UNIVERSITY OF LEEDS

Bio-inspired Magnetic Robots for Tortuous Surgical Navigations: From Shape-forming Tentacles to Tip-growing Vines

Joshua Davy

Submitted in accordance with the requirements for the degree of Doctorate of Philosophy

The University of Leeds

Faculty of Engineering

School of Electronic and Electrical Engineering

October 2025

This thesis is dedicated to my Dad,

Robert Neil Davy

1966 - 2013

Intellectual Property and Publication Statements

This PhD is presented under the alternative thesis style of the University of Leeds and as such its content is formed of three journal publications. All work from these publications is presented as published with the exception of minor edits to the figures to fit the thesis format and British English spellings.

I confirm that the work submitted is my own, except where work which has formed part of jointly authored publications has been included. My contribution and that of the other authors to this work are explicitly indicated below. I confirm that appropriate credit has been given within the thesis where reference has been made to the work of others. The author's contribution is notated by the initials **J.D.**

Chapter 2 includes work from the jointly authored publication:

Davy, J., Lloyd, P., Chandler, J.H. and Valdastri, P., 2023. A framework for simulation of magnetic soft robots using the material point method. IEEE Robotics and Automation Letters, 8(6), pp.3470-3477.

The contribution to this work is as follows:

- Conceptualization:**J.D.**
- Methodology: **J.D.**, P.L.
- Investigation: **J.D.**

- Funding: P.V.
- Supervision: P.L, J.H.C, P.V.
- Writing—original draft: **J.D**, P.L., J.H.C., P.V.
- Writing—review & editing: **J.D**, P.L., J.H.C, P.V.

I was fundamentality responsible for the design, implementation and evaluation of the simulation framework including all programming, developing experimental setups. P.L assisted in the mathematical derivations for the magnetic modelling.

Chapter 3 includes work from the jointly authored publication:

Davy, J., Greenidge, N.J., Kim, S., Tinsley, L.J., Lloyd, P., Chandler, J.H., Harris, R.A., Morimoto, T.K. and Valdastri, P., 2024. Vine robots with magnetic skin for surgical navigations. IEEE Robotics and Automation Letters, 9(8), pp.6888-6895. The contribution to this work is as follows:

- Conceptualization: **J.D.**
- Methodology: **J.D.**, N.J.G., S.K., L.T., P.L.
- Investigation: **J.D.**, N.J.G., S.K.
- Funding: T.K.M, R.A.H, P.V.
- Supervision: T.K.M, P.V
- Writing—original draft: **J.D.**, N.J.G., S.K, L.J.T., P.R.L., J.H.C., R.A.H, T.K.M., P.V.
- Writing—review & editing:**J.D.**, N.J.G., S.K, L.J.T., P.R.L., J.H.C., R.A.H, T.K.M., P.V.

I was responsible for the original concept design and fabrication. I worked with N.J.G on the experimental design and evaluation. The group at San Diego (S.K. and T.K.M.) were responsible for the modelling of the robot deformation.

Chapter 4 includes work from the jointly authored publication:

Davy, J., Dean, T.P., Greenidge, N.J., Calmé, B., Lloyd, P., Chandler, J.H. and Valdastri, P., 2025. Magnetic Fluid-Driven Vine Robots for Minimally Invasive Tissue Biopsy Sampling. Advanced Intelligent Systems, p.2400827.

- Conceptualization: **J.D.**
- Methodology: **J.D.**, T.P.D. N.J.G, P.R.L,
- Investigation: **J.D.**, T.P.D.
- Funding: P.V.
- Supervision: B.C, P.V.
- Writing—original draft: **J.D.**, T.P.D. N.J.G, B.C., P.R.L., J.H.C., P.V.
- Writing—review & editing: **J.D.**, T.P.D. N.J.G, B.C., P.R.L., J.H.C., P.V.

I was again responsible for the concept design and fabrication of the device. I worked with T.P.D. on the experimental setups and evaluation.

In addition, the following papers have also contributed to the work discussed in this thesis:

- Pittiglio, G., Brockdorff, M., da Veiga, T., **Davy, J.**, Chandler, J.H. and Valdastri, P., 2022. Collaborative magnetic manipulation via two robotically actuated permanent magnets. IEEE Transactions on Robotics, 39(2), pp.1407-1418.
- **Davy, J.**, Da Veiga, T., Pittiglio, G., Chandler, J.H. and Valdastri, P., 2023, April. Independent Control of Two Magnetic Robots using External Permanent Magnets: A Feasibility Study. In 2023 International Symposium on Medical Robotics (ISMR) (pp. 1-7). IEEE.
- Brockdorff, M., da Veiga, T., **Davy, J.**, Lloyd, P., Chandler, J.H., Pittiglio, G., Mathew, R.K. and Valdastri, P., 2025. Hybrid trajectory planning of two permanent magnets for medical robotic applications. The International Journal of Robotics Research, 44(2), pp.273-290.

- **Davy, J.**, Brockdorff, M. and Valdastri, P., 2025. Utilizing Field Gradient Measurements for Object Tracking in Permanent Magnet based Manipulation Systems. IEEE Transactions on Magnetics.
- Kim, N.G., Greenidge, N.J., **Davy, J.**, Park, S., Chandler, J.H., Ryu, J.H. and Valdastri, P., 2025. External steering of vine robots via magnetic actuation. Soft Robotics, 12(2), pp.159-170.
- Dean, T.P., **Davy, J.**, Scott, J., Valdastri, P. and Chandler, J.H., 2025, April. Anisotropic 3D-Knitted Sleeves as Inverse Pneumatic Artificial Muscles for Soft and Wearable Robotics. In 2025 IEEE 8th International Conference on Soft Robotics (RoboSoft) (pp. 1-6). IEEE.

Acknowledgements

First and foremost, I would like to thank Pietro Valdastri for the incredible opportunity to pursue a PhD under his supervision. I have always appreciated his ability to see through the noise and provide clear guidance, as well as his support of me and my ideas. I would also like to thank my secondary supervisor James Chandler for his support both academically and personally.

I would like to thank Nikita, Ben, Tom, Andrea and all of the STORM Lab for their friendship and making me laugh every day. They turned a PhD from a potentially lonely individual experience to a collaborative, fun and exciting one. I would like to give a special mention to Pete, whose combination of supervision and thoughtful personal mentorship has been so valuable to me. I would also like to thank Samwise and Clare for their help and support.

I'd further like to thank all my friends outside of university who have supported me and made me laugh through the past few years. I could not of done it without them. Finally, I would like to acknowledge the tireless support of my Mum, Jennifer Davy, whose support and kindness through times thick and thin have contributed more than anyone.

Abstract

There are areas of the body which cannot be surgically accessed without associated risk of tissue trauma. This thesis concerns itself with the design of miniaturised surgical robots designed to navigate deep within the anatomy in a minimally invasive manner. This work considers the navigation of tortuous lumina, such as those found in the bronchial tree of the lungs where the level of curvature required is notably high, and for traditional catheter designs requires large insertion forces at the proximal end of the device.

To counter these challenges, this thesis proposes bio-inspired robots for navigation of such environments. The first is a tentacle-like magnetic catheter designed to reduce interaction forces by full shape control. These miniature robots are fabricated based on a computational design process. To aid in this, the thesis develops a fully open-source continuum mechanics framework for simulation of magnetic soft structures to create patient-specific robot designs based on the Material Point Method. Follows is a discussion of the application of these robots and its associated challenges, particularly when high deformation and dexterity are required. After which. the thesis introduces a new class of continuum robot inspired by the movement of plant vines. This robot named the Magnetic Vine Robot (MVR), is formed of an entirely soft, flexible structure and contains a magnetic element therefore enabling steering under externally applied magnetic fields. Further, under internal fluidic pressure the robot propels itself forward moving without relative friction with the external environment enabling navigation of tortuous lumina. Proposed are two such MVR designs, the first formed of a magnetic skin and the second containing a magnetic liquid. These are then evaluated in a range

of diameters from 4 - 8 mm. Our unique approach, retains the soft structure of the robot allowing it to squeeze through small gaps, passively conform to the environment and capable of high curvature and stabilisation. These novel robot designs are then demonstrated in navigating tortuous anatomy both on table-top environments and then in realistic physical phantoms as pre-clinical studies, paving the way for their potential application in the real-world surgical environment.

Acronyms

CMOS Complementary Metal Oxide Semiconductor.

CSF Cerebral-Spinal Fluid.

DoF Degrees of Freedom.

EPM External Permanent Magnet.

FEM Finite Element Method.

MIS Minimally Invasive Surgery.

MPM Material Point Method.

MSR Magnetic Soft Robots.

MVR Magnetic Vine Robot.

ODE Ordinary Differential Equation.

Contents

List of Figures

List of Tables

Chapter 1

Background

1.1 Surgical Instruments

In the operating room, surgical instruments provide the necessary tools to perform the highly complex tissue interaction and manipulation performed by surgeons. Despite many advancements, surgery remains a mostly hands-on procedure with surgeons directly holding and manipulating simple tools. Sufficiently dextrous instruments enable Minimally Invasive Surgery (MIS), where the point of entry is through keyhole incisions or natural orifices [1], [2]. MIS holds appeal due to the potential for reduced recovery times and improved access to specific hard-to-reach areas of the body. Endoscopes are one group of such surgical instruments that integrate visualisation such as fibre imaging or digital cameras at their tip to provide a view point for the surgeon [3]. Examples include colonoscopy where an endoscope is inserted through the rectum for inspections of the colon, gastroscopes for visualisation of the stomach and bronchoscopy for the lungs [4]. Endoscopes are often integrated with tool channels allowing their use for treatment as well as their diagnostic functionality. Tools such as biopsy tools, grasping forceps or retrieval baskets can be utilised within this channel to allow for direct tissue interaction and removal [5].

With the design of any surgical instrument, care must be given for its design to not

induce harm. Traditional tools are made from hard materials relative to the soft tissues in which they interact, leading them to carry the risk of tissue damage during insertion [6]. This effect is exacerbated when navigating in highly tortuous lumen where friction accumulates requiring larger forces of insertion [7]. The potential risk of this trauma is of further concern in particularly low diameter lumen which are often associated with thin tissue walls and delicate anatomy such as those deep in the lungs. The majority of modern dextrous surgical instruments utilise internal tendons for actuation [6]. These tendons are used to deform the manipulator/catheter/tool's body allowing for steering of the device through bifurcations in the lumen. Tendon-driven devices are however often limited in dexterity and to hard materials, and the required forces and material strength increases with any decrease in tool diameter [8].

With our goal of providing new avenues for treatment, this thesis explores the development of surgical instruments for navigating delicate tortuous lumina within the anatomy. The objective is to propose a new form of surgical instrument based on advanced robotic structure where we utilise the principles of soft robots to create tools with an inherent safety factor associated with them. Further, we propose the utilisation of advanced actuation methodologies based on magnetic and fluidic systems enabling miniaturisation of our devices. These devices have the potential to reduce the invasiveness of some procedures and potentially open up new avenues for treatment in the surgical environment.

1.2 Bio-inspired Robotics

When designing dextrous slender robotised catheters for MIS, inspiration can be drawn from nature for its design. Often cited examples include the tentacles of an octopus or squid, the growth of vines or the peristaltic movement of worms [9].

The tentacles of Cephalopods serve a multitude of functions assisting in both manipulation and locomotion of the animal [10]. These bodies are entirely flexible containing no hard skeletal structure or fluidic spaces and are actuated through muscle fibres along the length. Crucially, tentacles are not limited to simple bending but have control over their

pose along their length leading to more complex profiles. This allows the creatures to manipulate objects and navigate their environments with ease. Plant vines navigate not through translation but through growth [11]. As the plant grows, new cells are created at the plant tip therefore extending length. Despite their soft structure, plant vines are capable of navigating through cracks in hard structures embedding themselves within stones or trees. This ability is unique to their growth characteristics allowing them to overcome friction with the external environment through tip-centred movement. Crucially plant vines make use of contact with the environment as a point of stabilisation, this lets them overcome their soft structure in order to create large navigation forces (such as overcoming of gravity) when necessary.

At the centimetre to metre scale, robotic systems are able to somewhat mimic the behaviour of animals and plants. However, when we come to the millimetre scale and below, the performance-gap between our robots and nature becomes apparent. The idea of a sub-centimetre robot capable of anything but the simplest of tasks whilst containing it's own energy storage, actuators, computer and sensors is not feasible with current technology [12], [13]. The reasoning for this is our lack of appropriate materials and fabrication methodologies for building robots at this scale. Modern additive manufacturing methods can be limited at these small scales and common actuation methodologies applied to robotics such as electromagnetic motors do not scale well to this small size. In addition, batteries are limited in miniaturisation and often become a limiting factor. We may conclude from this that the appropriate direction for advancement in millimetre scale robots is to directly pursue advanced manufacturing techniques and study deeply the material requirements. Indeed, there is a wealth of research into miniaturisation of these technologies mostly centred around additive manufacturing [14]. However with our very real clinical need for such dextrous devices our focus is also on how we can directly overcome these challenges of integration.

1.3 Millimetric Robots

In order to miniaturise our robots, we move all but essential systems outside of the internal structure. The robot still contains sensors and actuators however the processing is all external with the internal energy source replaced with some form of generator which sends power to the embedded actuators. Sensory information is not processed onboard but instead sent as raw signals to external processors. Because of the challenges of working at this scale, not just the size of these systems is reduced but their fundamental working principle is often different [15], [16].

Common sensors embedded within miniature surgical continuum robots include micro Complementary Metal Oxide Semiconductor (CMOS) cameras, fiberscopes and fibre-based shape sensors [17], [18]. These sensors are often interfaced through electrical wires, fluidic chambers or optical fibres to the external system. Micro-sensing is a large area of open research with challenges such as hysteresis, miniaturisation and robustness however this thesis concerns itself mostly with the problems of micro-actuation [17], [19], [20].

External actuation can be approached in several ways. The simplest to consider is that we move the large motors we usually use in large-scale robotics outside of our workspace and transfer their produced force through tendons or rods [8], [21]. This forms the basis of tendon-driven robots [6]. These can be thought of as a robotised evolution of common tendon-driven surgical tools used today with tendons acting in parallel to create opposing moment to deform the robot with multiple DoF [8]. Tendon-driven robots rely on a proven technology, which is compact and produces relatively large forces (Figure 1.1a). However, challenges come with miniaturisation of this technology particularly below 2-3 mm due to the decreased moment with which the tendons act. The use of rotating and translating rods, leads to the concentric tube robot where pre-bent tubes are used in opposition to create arbitrary deformation [22], [23] (Figure 1.1b). Concentric tube robots are impressive in their small scale and force output however their motion can be somewhat unpredictable with snapping instabilities caused by torsional wind-up between the tubes [24]. Fluidic driven continuum robots utilise pneumatic or hydraulic bellows

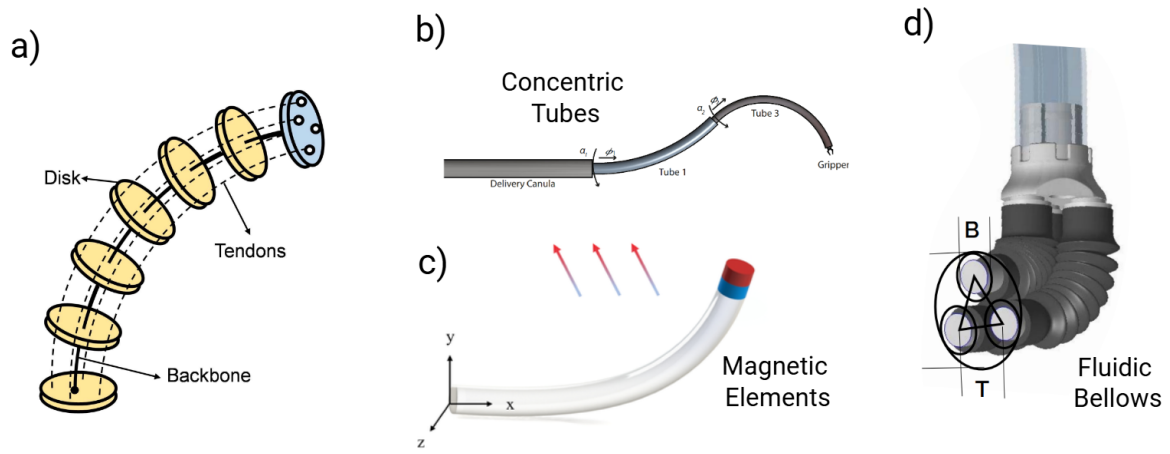

Figure 1.1: a) Tendon-driven continuum robot as taken from [26]. Pulling on the tendons leads to deformation in the spaced disks. b) Concentric tube robot with three tubes as taken from [27]. Concentric tube robots utilise hyperelastic tubes whose resultant shape is a product of their relative translation and orientation leading to a summation of their elastic energies. c) Magnetic continuum robot with tip magnetic element as taken from [28]. Magnetic actuation relies on a external magnetic manipulation system to apply specific magnetic fields to induce forces and torques on the internal magnetic elements of the robot d) Fluidic Bellow-driven robot with three parallel bellows as taken from [25]. By appling fluidic pressure from a extenal source the bellows contract or expand. Multiple bellows can be combined to create multiple DoF systems.

which are pressurised from an external source to deform the robot [25] (Figure 1.1d). Similar to tendon-driven robots, these bellows often act in parallel to create opposing moments for multi-DoF deformation. However these systems also struggle with challenges in miniaturisation and overall deformation achievable due to their need for internal fluid channels and difficult of fabrication.

In our research group we specialise in the use of magnetic manipulation, here the generator is formed of a magnetic source; either electromagnetic coils or permanent magnets [29], [30]. This allows for the manipulation of the magnetic field in the workspace. As actuators, we embed magnetic elements within the structure of our robot, which respond to the applied magnetic field with both an alignment torque and a field-gradient related force [31] (Figure 1.1d). This external actuation methodology has several advantages. The first is that it acts "wirelessly" with no need for any physical connection between the generator and actuator, the second is the preciseness in which force and torques can be applied with easy to characterise models. Further, through the use of magnetic

micro-particles, magnetic elements can be integrated into the robot whilst preserving soft structures enabling designs which are both highly miniaturised but also compliant with their environment [32].

1.4 Magnetic Manipulation

Magnetic manipulation refers to the use of externally applied magnetic fields to create a source of potential for internal actuators. For magnetic manipulation these fields are typically in the $0 - 100$ mT range [33]. Magnetic elements within a magnetic field will hold a magnetic potential energy dependent on their position and orientation within that field. In this thesis we mostly consider hard-magnetic elements (with the exemption of some aspects of Chapter 4). Hard magnetic elements are characterised by their fixed magnetic flux density under typically applied fields.

A hard-magnetic material holds a fixed magnetic flux density present with or without an externally applied field. This quantity is referenced to as its magnetic remanence ($\mathbf{B}_r$) with NdFeB a popular choice due to its large magnitude ($|\mathbf{B}_r| \approx 1.4$T). The direction of this vector, is the direction of magnetisation of the material i.e. the direction from its south to north pole. As the material rotates, so does this vector. From the remanence we can calculate the magnetic moment of the material

$$\mathbf{m} = \frac{\mathbf{B}_r V}{\mu_0}, \tag{1.1}$$

where V is the volume of the magnetic element and μ_0 is the magnetic vacuum permeability equal to $4\pi \times 10^{-7}$ Hm^{-1}.

When the magnetic element is placed within an external magnetic field $\mathbf{B}$ it holds magnetic potential energy

$$U = -\mathbf{B} \cdot \mathbf{m}. \tag{1.2}$$

From which can be derived the resultant force and torque on the element

$$\boldsymbol{\tau} = -\frac{\partial U}{\partial \theta_n}\mathbf{n} = \frac{\partial(\mathbf{B}\cdot\mathbf{m})}{\partial\theta_n}\mathbf{n} = \frac{\partial(|\mathbf{B}||\mathbf{m}|\cos\theta_n)}{\partial\theta_n}\mathbf{n} = -|\mathbf{B}||\mathbf{m}|\sin(\theta_n)\mathbf{n} = \mathbf{m}\times\mathbf{B}, \quad (1.3)$$

where θ_n is a rotation around the axis $\mathbf{n}$.

$$\mathbf{F} = -\frac{\partial U}{\partial \mathbf{x}} = \frac{\partial(\mathbf{B}\cdot\mathbf{m})}{\partial\mathbf{x}} = \frac{\partial(\mathbf{B}^T\mathbf{m})}{\partial\mathbf{x}} = G^T\mathbf{m} \quad (1.4)$$

where we define $G = \frac{\partial \mathbf{B}}{\partial \mathbf{x}}$ is the spatial derivative of the magnetic field.

It is worth noting the tensor G in a current free workspace is both symmetric and traceless (as follows from the Maxwell equations $\nabla\cdot\mathbf{B} = 0$, $\nabla\mathbf{B} = 0$) leading to their only being five independent elements [31].

These above equations assume the magnetic material to behave as a point-like magnetic element known as a magnetic dipole. As we will consider hard magnetic elements for the source of our actuating external field we can model the magnetic field produced by these elements using the dipole equation

$$\mathbf{B}(\mathbf{r}) = \left(\frac{\mu_0}{4\pi|\mathbf{r}|^3}(3\hat{\mathbf{r}}\otimes\hat{\mathbf{r}} - \mathbb{I})\right)\mathbf{m}, \quad (1.5)$$

where $\mathbf{r}$ is the displacement between the dipole position and measurement point. $\hat{\mathbf{r}} = \frac{\mathbf{r}}{||\mathbf{r}||}$. $\hat{\mathbf{r}}$ corresponds to the unit direction vector of $\mathbf{r}$, $\otimes$ is the outer product.

with the spatial derivative

$$G(\mathbf{r}) = \frac{\partial \mathbf{B}(\mathbf{r})}{\partial \mathbf{x}} = \frac{3\mu_0}{4\pi|\mathbf{r}|^4}(\mathbf{m}\otimes\hat{\mathbf{r}} + \hat{\mathbf{r}}\otimes\mathbf{m} + \hat{\mathbf{r}}\cdot\mathbf{m}(\mathbb{I} - 5\hat{\mathbf{r}}\otimes\hat{\mathbf{r}})). \quad (1.6)$$

1.5 Magnetic Continuum Robots as Surgical Instruments

The first recorded use of magnetic elements as actuators for surgical instruments dates to 600 BC for the extraction of iron arrows [34]. In the modern day, the development of high strength magnetic materials has allowed for the creation of miniaturised magnetic devices leading to a wealth of research into both the design of these instruments and actuation methodologies [35]. For the design of magnetic continuum robots, the simplest design consists of a singular magnetic element placed at the robot tip [36]. Due to the remote actuation methodology, there is no need for complex structures or force transfer mechanisms in the body of the robot itself, enabling this to be competitively soft and compliant. This soft structure reduces the invasiveness of insertion enabling the robot to naturally conform to the anatomy. An alternate approach to that of a tip-magnet is to embed multiple magnetic elements along the length of the robot [37], [38]. This allows for a distributed loading and an increase in overall magnetic volume enabling full body control of the system and a larger relative magnetic volume. At the limit, this can be implemented with magnetic micro-particles enabling full retention of the soft structure [32], [39], [40]. One important design decision is the direction of magnetisation of the magnetic elements. In the simplest case this "magnetic profile" aligns with the major axis of the continuum robot. This system proves the simplest to model but is limited to simple deformations. An alternate approach, is that of a magnetisation profile which varies along the robot length. This approach, although more complex to model and control gives a wide range of possible deformations [41], [42]. See Figure 1.2.

For the generation of the source magnetic field much work utilises systems based on electromagnetic coils [30], [43]. With the field strength proportional to the current in the coil, fields can be precisely controlled at high frequency and importantly, switched off entirely. Coils arranged in pairs in a Helmholtz configuration allow for high field homogeneity across a workspace. Practically, coils require large power supplies and usually

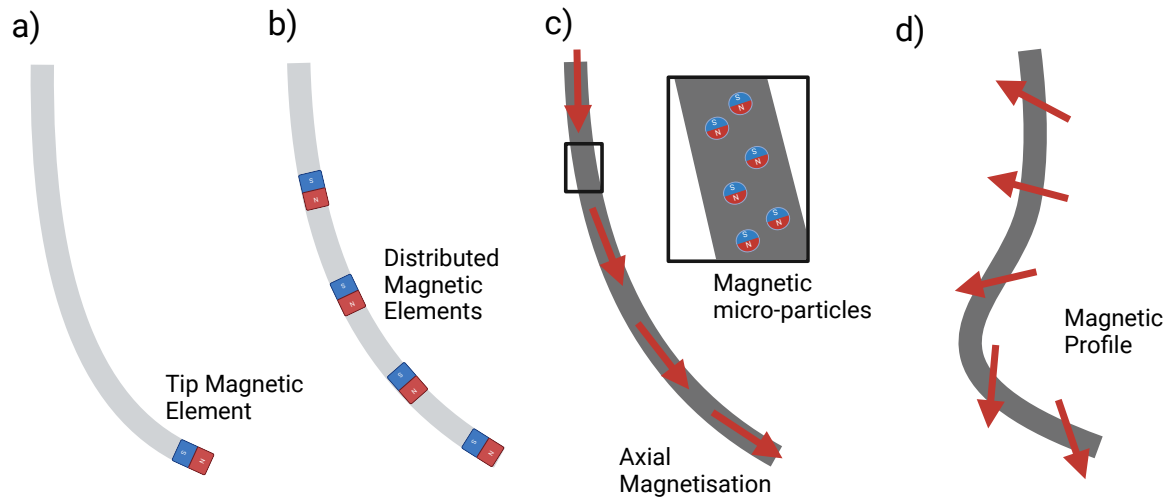

Figure 1.2: Overview of some approaches to magnetic continuum robots. a) A magnetic continuum robot with a singular magnetic element at the tip b) A robot with distributed magnetic elements along its length c) The use of magnetic micro-particles to preserve the robot's soft structure d) The use of a magnetic profile to allow for complex deformations under an applied field. Red arrows represent the direction of magnetisation in the material.

some form of active water-cooling for clinical scale devices. Alternatively is the use of External Permanent Magnet (EPM) approaches [29], [44], [45]. Here the field is always "on" when in the vicinity of the magnet but produces a large field for a given volume. To manipulate the field, the EPM is oriented and positioned relative to the magnetic instrument. This is the approach explored by our group, where we utilise collaborative manipulators with EPMs as end effectors enabling a large and adaptable workspace. See Figure 1.3.

A limitation of magnetic manipulation can be found by analysing the equations of Section 1.4. The magnetic torques imposed are related to distance from the dipole source as $\frac{1}{|\mathbf{r}|^3}$, however the forces drop off much faster with the relationship $\frac{1}{|\mathbf{r}|^4}$. This makes the ability to "pull" elements through magnetic forces in the body quite limited for tethered devices and often these robots still require insertion from their proximal end. This effect is exacerbated in tortous anatomy where friction accumulates and required stiffness increases.

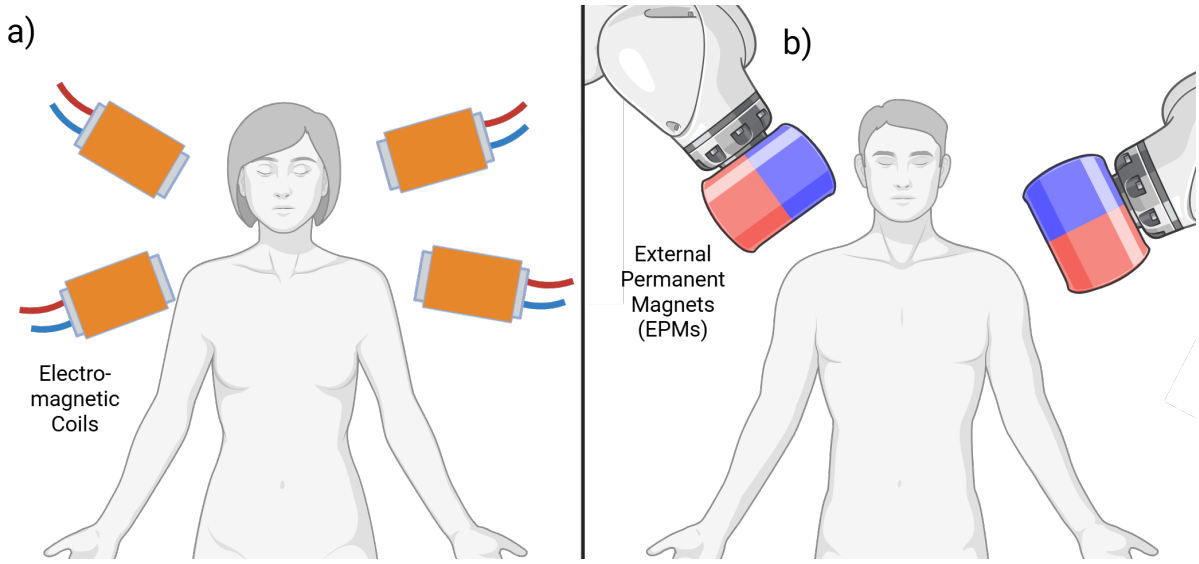

Figure 1.3: The two most common approaches to generation of magnetic fields for manipulation of magnetic continuum robots. a) Systems of electromagnetic coils produce a field proportional to applied currents. b) EPMs are positioned and oriented to create a desired magnetic field.

1.6 Simulation and Modelling of Magnetic Robots

Simulation represents a key aspect of modern robot design allowing for ideas to be tested and developed without the real world complexities of manufacturing [46]. Further, simulation enables variables such as deformation or internal forces to be studied with ease as these can be difficult to measure from real experiments [40], [47]. This is particularly applicable to the surgical use-case where quantification of potentially traumatic tissue forces can be difficult. Furthermore, simulation can be used as part of computational design processes such as to create specific robot designs for a given task [40]. Here, optimisation algorithms can utilise a simulation with a potentially abstract objective to improve robot designs or allow for parameter selection for controllers. After simulation-based design, the robot can be fabricated and utilised. This is highly dependent on reducing the *reality gap* between simulation and real world robots as well as obtaining any required material parameters [48].

The simulation of soft robots is particularly challenging given their technically infinite DoF. The simplest form of soft robot modelling considers segmenting the robot into

sections and assuming them as rigid [49]. These rigid link models are often fast but can be limited in accuracy at high deformations. Cosserat-rod assumptions enable full modelling of the deformation with high curvature but are limited to continuum structures [50]. Further, these simplified forms of models fail to capture complex interactions with the environment such as collision, friction and other environmental interactions.

For representation of the true soft robot shape and structure, full continuum mechanics models allow for complete representation of the soft body. Different material models can be readily integrated as well as external collisions and forces. Open frameworks based on finite element methods such as SoFa, have been established for soft robotics research and have been utilised for computational design frameworks as well as real-time robot control [51], [52].

For modelling of the magnetic effects, similar levels of assumption exist. When modelling rigid magnetic elements the dipole approximations as given in Section 1.3 are adequate given sufficient distance between elements. Modelling of magnetic hard elements in close-proximity should utilise full multipole expansions or Ordinary Differential Equation (ODE) solutions in order to well present the resultant force and torques [53]. For magnetic soft materials (i.e. those formed of embedded magnetic micro-particles), assumptions of discrete hard magnetic elements can be made however fail to represent the deformation experienced within the material. To this end, continuum mechanics frameworks which integrate stress-strain relationships have been developed [54]. Often, in the interest of reduced computational complexity, these models do not consider the self-interaction between magnetic elements, instead only considering their resultant stress due to external magnetic fields.

1.7 Shape-forming Tentacles

The work presented in this thesis sits within an ERC consolidator grant project on the design of "patient-specific" magnetic tentacle-like robots (NoLiMiTs, 818045). These robots are formed of a specific magnetic profile unique to the patients anatomy minimising

interaction forces with the external environment [40], [55]–[57]. This approach proposes an end-to-end process where the target centrelines are extracted from pre-operative CT followed by a computational-design process to determine the magnetic profile of the robot based on an internal simulation/model and then followed by fabrication of the robot. This approach has been validated in several phantom and cadaveric experiments and shown to improve navigation ability and overall system dexterity.

Advancements to this technique have seen the use of anisotropic materials, complex geometries and various magnetic materials [41], [58]. One limitation in the current approach however is the model used in the computational design process with often large reality-gaps between expected and measured performance. This effect is exacerbated particularly when considering high curvatures, multi-materials and varying geometry. This can be attributed to the simple rigid-link model utilised which makes rigid-body assumptions of the soft robot. This simple model although computationally tractable, fails to account for realistic material behaviour in these complex scenarios and has significant error at large deformation.

1.8 Tip-growing Vines

Vine robots are a class of continuum robot that move without translation relative to their environment [59]–[61]. Instead, these robots "grow" at their tip, extending their length. These robots are of particular interest for environments with high friction as, due to their tip-growing locomotion, external interactions on their body do not prevent their movement. Often these robots are likened to the growth of plant vines, with their ability to conform to the anatomy and use the external environment as points of stabilisation.

One popular method utilises the principle of eversion to create a tip-growing structure [59], [63]. Here the robot is formed of a thin-walled flexible tube which is inverted inside of itself. Then, the internal body is pressurised causing the inverted material to be expelled outward at the robot tip extended its length. This enables an entirely soft structure whilst moving without shearing interaction with the environment. Further, due to the

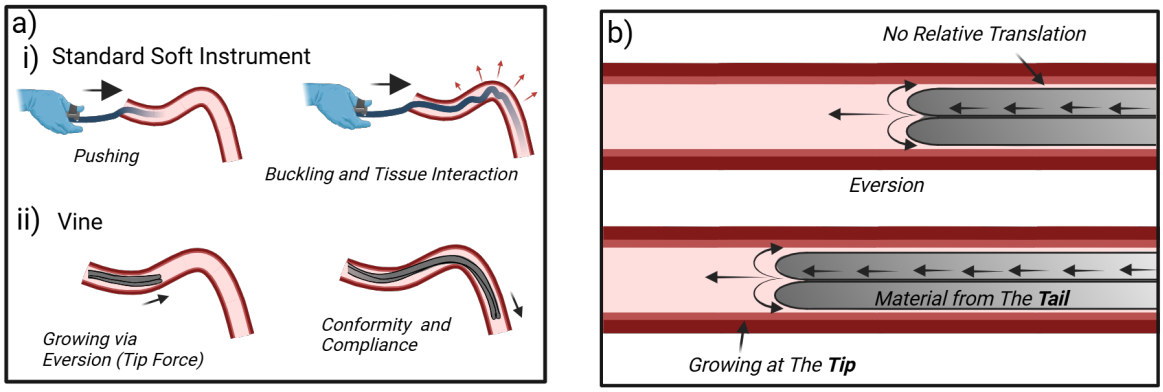

Figure 1.4: a) Principles of Vine or Growing Robots when compared to standard compliant instruments b) The eversion principle achieves tip growing using a thin-wall pressurised tube. As adapted from [62].

soft structure, these robots can squeeze through small gaps and conform naturally to their surroundings.

This principle of eversion was first explored for the clinical setting in the work of Goldstein et al. [64]. This work introduces a 1 mm diameter catheter for navigation of blood vessels. This work is impressive in its miniaturisation but lacks a methodology for active steering of the robot. Recently, several groups have proposed forms of vine robot steering. Tendon-driven methods have been demonstrated at small scale but sacrifice the soft body of the robot making it comparatively stiff [63]. Others have integrated fluidic bellows into the body of the robot but these are difficult to miniaturise and have a relatively complex level of manufacturing [59], [65].

A further challenge is functionalisation of these devices, in particular maintaining anything at the tip of the robot during insertion can be challenging [66]. This can be attributed to the growing nature of the robot meaning no part can be considered as a tip attachment point. Further, due to the everting nature the vine will passively push any object located within the tail out of the tip as is grows, this means that using this channel as an internal tool channel can be challenging [67]. This has lead to several groups exploring the use of caps for the robot that can be used as a point of attachment for sensors and tools [60], [66].

1.9 Summary

In this background section, we outlined the clinical need for more dextrous surgical catheters to improve patient outcomes and open up new avenues of treatment. Particular examples include the interaction of tissues for biopsy as well as diagnosis visualisation via micro-cameras. We then discussed bio-inspiration in robotic systems and how the question of robot scale determines the approach of robot design. It is highly desirable to achieve robot systems than replicate nature in terms of dexterity and manipulation skills at a small-scale. However, we concluded that it is not possible with current manufacturing and fabrication techniques to mimic small animals and plants in their energy storage and dexterity, and concluded that in order to create surgical tentacle or vine-like robots with the dexterity we require we must rely on external actuation. This lead us to the topic of magnetic manipulation and the design of magnetic robots. This was followed by a discussion of the challenges of design of magnetic robots particularly when desiring dextrous high degree of freedom systems. We discussed the established research avenue of shape-forming patient-specific magnetic tentacle robots and relevant literature in the area with a focus on the challenges of simulations of magnetic and compliant systems. Finally, we returned to our discussion of bio-inspiration and considered vine robots which navigate their environment through growing and how these lead to potentially less tissue trauma with their surroundings and navigation of complex environments.

References

[1] X. Hu, A. Chen, Y. Luo, C. Zhang, and E. Zhang, "Steerable catheters for minimally invasive surgery: A review and future directions," *Computer Assisted Surgery*, vol. 23, no. 1, pp. 21–41, 2018.

[2] K. Fuchs, "Minimally invasive surgery," *Endoscopy*, vol. 34, no. 02, pp. 154–159, 2002.

[3] P. Valdastri, M. Simi, and R. J. Webster III, "Advanced technologies for gastrointestinal endoscopy," *Annual review of biomedical engineering*, vol. 14, no. 1, pp. 397–429, 2012.

[4] S. M. Kavic and M. D. Basson, "Complications of endoscopy," *The American journal of surgery*, vol. 181, no. 4, pp. 319–332, 2001.

[5] A. Khanicheh and A. K. Shergill, "Endoscope design for the future," *Techniques in gastrointestinal endoscopy*, vol. 21, no. 3, pp. 167–173, 2019.

[6] T. da Veiga, J. H. Chandler, P. Lloyd, *et al.*, "Challenges of continuum robots in clinical context: A review," *Progress in Biomedical Engineering*, vol. 2, no. 3, p. 032 003, 2020.

[7] R. Dreyfus, Q. Boehler, S. Lyttle, *et al.*, "Dexterous helical magnetic robot for improved endovascular access," *Science Robotics*, vol. 9, no. 87, eadh0298, 2024.

[8] J. Burgner-Kahrs, D. C. Rucker, and H. Choset, "Continuum robots for medical applications: A survey," *IEEE transactions on robotics*, vol. 31, no. 6, pp. 1261–1280, 2015.

[9] R. Pfeifer, M. Lungarella, and F. Iida, "Self-organization, embodiment, and biologically inspired robotics," *science*, vol. 318, no. 5853, pp. 1088–1093, 2007.

[10] W. M. Kier, "The functional morphology of the tentacle musculature of nautilus pompilius," in *Nautilus: The Biology and Paleobiology of a Living Fossil, Reprint with additions*, Springer, 1987, pp. 257–269.

[11] F. E. Putz and H. A. Mooney, *The biology of vines*. Cambridge University Press, 1991.

[12] M. Wehner, R. L. Truby, D. J. Fitzgerald, *et al.*, "An integrated design and fabrication strategy for entirely soft, autonomous robots," *nature*, vol. 536, no. 7617, pp. 451–455, 2016.

[13] T. Tolley Michael, F. Shepherd Robert, C. Galloway Kevin, J. Wood Robert, M. Whitesides George, *et al.*, "A resilient, untethered soft robot," *Soft robotics*, 2014.

[14] G. Stano and G. Percoco, "Additive manufacturing aimed to soft robots fabrication: A review," *Extreme Mechanics Letters*, vol. 42, p. 101 079, 2021.

[15] T. Da Veiga, J. H. Chandler, G. Pittiglio, *et al.*, "Material characterization for magnetic soft robots," in *2021 IEEE 4th International Conference on Soft Robotics (RoboSoft)*, IEEE, 2021, pp. 335–342.

[16] Z. Yang and L. Zhang, "Magnetic actuation systems for miniature robots: A review," *Advanced Intelligent Systems*, vol. 2, no. 9, p. 2 000 082, 2020.

[17] I. Payo, V. Feliu, and O. D. Cortázar, "Fibre bragg grating (fbg) sensor system for highly flexible single-link robots," *Sensors and Actuators A: Physical*, vol. 150, no. 1, pp. 24–39, 2009.

[18] R. Daher, C. Kendrick, M. H. Yap, D. Leff, and S. Giannarou, "Vision-based robot localisation for ductoscopic navigation," in *Hamlyn Symposium on Medical Robotics*, p. 89.

[19] K. Meena and A. R. Sankar, "Biomedical catheters with integrated miniature piezoresistive pressure sensors: A review," *IEEE Sensors Journal*, vol. 21, no. 9, pp. 10 241–10 290, 2021.

[20] Z. Shen, Z. Zhang, N. Zhang, *et al.*, "High-stretchability, ultralow-hysteresis conductingpolymer hydrogel strain sensors for soft machines," *Advanced Materials*, vol. 34, no. 32, p. 2 203 650, 2022.

[21] C. Benoist, C. Girerd, N. Zemiti, P. Poignet, and P. Berthet-Rayne, "Tendon-driven vs rod-driven continuum robots: A bench test evaluation," in *CRAS 2024-Conference on New Technologies for Computer and Robot Assisted Surgery*, 2024.

[22] H. B. Gilbert, D. C. Rucker, and R. J. Webster III, "Concentric tube robots: The state of the art and future directions," in *Robotics Research: The 16th International Symposium ISRR*, Springer, 2016, pp. 253–269.

[23] P. E. Dupont, J. Lock, B. Itkowitz, and E. Butler, "Design and control of concentric-tube robots," *IEEE Transactions on Robotics*, vol. 26, no. 2, pp. 209–225, 2009.

[24] J.-S. Kim, D.-Y. Lee, K. Kim, S. Kang, and K.-J. Cho, "Toward a solution to the snapping problem in a concentric-tube continuum robot: Grooved tubes with anisotropy," in *2014 IEEE International Conference on Robotics and Automation (ICRA)*, IEEE, 2014, pp. 5871–5876.

[25] N. Garbin, L. Wang, J. H. Chandler, K. L. Obstein, N. Simaan, and P. Valdastri, "A disposable continuum endoscope using piston-driven parallel bellow actuator," in *2018 International Symposium on Medical Robotics (ISMR)*, IEEE, 2018, pp. 1–6.

[26] R. Danesh and F. Janabi-Sharifi, "Backstepping control of tendon-driven continuum robots in large deflections using the cosserat rod model," *Mechanism and Machine Theory*, vol. 208, p. 105 953, 2025.

[27] F.-Y. Lin, C. Bergeles, and G.-Z. Yang, "Biometry-based concentric tubes robot for vitreoretinal surgery," in *2015 37th annual international conference of the IEEE engineering in medicine and biology society (EMBC)*, IEEE, 2015, pp. 5280–5284.

[28] P. M. Kolahi and M. H. Korayem, "Investigation and improving modeling and control for continuum magnetic robots using cosserat theories and optimal control," *Acta Mechanica*, vol. 235, no. 5, pp. 3095–3110, 2024.

[29] G. Pittiglio, J. H. Chandler, M. Richter, V. K. Venkiteswaran, S. Misra, and P. Valdastri, "Dual-arm control for enhanced magnetic manipulation," in *2020 IEEE/RSJ International Conference on Intelligent Robots and Systems (IROS)*, IEEE, 2020, pp. 7211–7218.

[30] B. J. Nelson, "An electromagnetic robot for navigating medical devices," *Nature Reviews Bioengineering*, vol. 2, no. 5, pp. 370–371, 2024.

[31] J. J. Abbott, E. Diller, and A. J. Petruska, "Magnetic methods in robotics," *Annual Review of Control, Robotics, and Autonomous Systems*, vol. 3, no. 1, pp. 57–90, 2020.

[32] Y. Kim, G. A. Parada, S. Liu, and X. Zhao, "Ferromagnetic soft continuum robots," *Science robotics*, vol. 4, no. 33, eaax7329, 2019.

[33] G. Pittiglio, M. Brockdorff, T. da Veiga, J. Davy, J. H. Chandler, and P. Valdastri, "Collaborative magnetic manipulation via two robotically actuated permanent magnets," *IEEE Transactions on Robotics*, vol. 39, no. 2, pp. 1407–1418, 2022.

[34] U. Häfeli, "The history of magnetism in medicine," *Magnetism in medicine*, vol. 2, pp. 3–25, 1998.

[35] H. Kirchmayr, "Permanent magnets and hard magnetic materials," *Journal of Physics D: Applied Physics*, vol. 29, no. 11, p. 2763, 1996.

[36] J. W. Martin, B. Scaglioni, J. C. Norton, *et al.*, "Enabling the future of colonoscopy with intelligent and autonomous magnetic manipulation," *Nature machine intelligence*, vol. 2, no. 10, pp. 595–606, 2020.

[37] D. Lin, N. Jiao, Z. Wang, and L. Liu, "A magnetic continuum robot with multimode control using opposite-magnetized magnets," *IEEE Robotics and Automation Letters*, vol. 6, no. 2, pp. 2485–2492, 2021.

[38] A. Mesot, Q. Boehler, F. Heemeyer, S. Lyttle, B. Aktaş, and B. J. Nelson, "Parametric design of continuum robots using interlocking ball joints," *Advanced Intelligent Systems*, p. 2 500 180, 2025.

[39] G. Pittiglio, P. Lloyd, T. da Veiga, *et al.*, "Patient-specific magnetic catheters for atraumatic autonomous endoscopy," *Soft robotics*, vol. 9, no. 6, pp. 1120–1133, 2022.

[40] P. Lloyd, G. Pittiglio, J. H. Chandler, and P. Valdastri, "Optimal design of soft continuum magnetic robots under follow-the-leader shape forming actuation," in *2020 International Symposium on Medical Robotics (ISMR)*, IEEE, 2020, pp. 111–117.

[41] P. Lloyd, O. Onaizah, G. Pittiglio, D. K. Vithanage, J. H. Chandler, and P. Valdastri, "Magnetic soft continuum robots with braided reinforcement," *IEEE Robotics and Automation Letters*, vol. 7, no. 4, pp. 9770–9777, 2022.

[42] L. Wang, D. Zheng, P. Harker, A. B. Patel, C. F. Guo, and X. Zhao, "Evolutionary design of magnetic soft continuum robots," *Proceedings of the National Academy of Sciences*, vol. 118, no. 21, e2021922118, 2021. DOI: 10.1073/pnas.2021922118. eprint: https://www.pnas.org/doi/pdf/10.1073/pnas.2021922118. [Online]. Available: https://www.pnas.org/doi/abs/10.1073/pnas.2021922118.

[43] A. Schonewille, C. He, C. Forbrigger, *et al.*, "Electromagnets under the table: An unobtrusive magnetic navigation system for microsurgery," *IEEE Transactions on Medical Robotics and Bionics*, 2024.

[44] J. W. Martin, B. Scaglioni, J. C. Norton, *et al.*, "Enabling the future of colonoscopy with intelligent and autonomous magnetic manipulation," *Nature machine intelligence*, vol. 2, no. 10, pp. 595–606, 2020.

[45] S. Salmanipour and E. Diller, "Eight-degrees-of-freedom remote actuation of small magnetic mechanisms," in *2018 IEEE international conference on robotics and automation (ICRA)*, IEEE, 2018, pp. 3608–3613.

[46] H. Choi, C. Crump, C. Duriez, *et al.*, "On the use of simulation in robotics: Opportunities, challenges, and suggestions for moving forward," *Proceedings of the National Academy of Sciences*, vol. 118, no. 1, e1907856118, 2021.

[47] H. Lipson, "Challenges and opportunities for design, simulation, and fabrication of soft robots," *Soft Robotics*, vol. 1, no. 1, pp. 21–27, 2014.

[48] N. Jakobi, P. Husbands, and I. Harvey, "Noise and the reality gap: The use of simulation in evolutionary robotics," in *European conference on artificial life*, Springer, 1995, pp. 704–720.

[49] C. Armanini, F. Boyer, A. T. Mathew, C. Duriez, and F. Renda, "Soft robots modeling: A structured overview," *IEEE Transactions on Robotics*, vol. 39, no. 3, pp. 1728–1748, 2023.

[50] J. Till, V. Aloi, and C. Rucker, "Real-time dynamics of soft and continuum robots based on cosserat rod models," *The International Journal of Robotics Research*, vol. 38, no. 6, pp. 723–746, 2019.

[51] E. Coevoet, T. Morales-Bieze, F. Largilliere, *et al.*, "Software toolkit for modeling, simulation, and control of soft robots," *Advanced Robotics*, vol. 31, no. 22, pp. 1208–1224, 2017.

[52] C. Wehner, F. Schubert, H. Hellkamp, *et al.*, "An open-source user-friendly interface for simulating magnetic soft robots using simulation open framework architecture (sofa)," *arXiv preprint arXiv:2508.10686*, 2025.

[53] A. J. Petruska and J. J. Abbott, "Optimal permanent-magnet geometries for dipole field approximation," *IEEE transactions on magnetics*, vol. 49, no. 2, pp. 811–819, 2012.

[54] R. Zhao, Y. Kim, S. A. Chester, P. Sharma, and X. Zhao, "Mechanics of hard-magnetic soft materials," *Journal of the Mechanics and Physics of Solids*, vol. 124, pp. 244–263, 2019.

[55] G. Pittiglio, P. Lloyd, T. da Veiga, *et al.*, "Patient-specific magnetic catheters for atraumatic autonomous endoscopy," *Soft Robotics*, 2022.

[56] G. Pittiglio, J. H. Chandler, T. da Veiga, *et al.*, "Personalized magnetic tentacles for targeted photothermal cancer therapy in peripheral lungs," *Communications Engineering*, vol. 2, no. 1, p. 50, 2023.

[57] P. Lloyd, A. K. Hoshiar, T. da Veiga, *et al.*, "A learnt approach for the design of magnetically actuated shape forming soft tentacle robots," *IEEE Robotics and Automation Letters*, vol. 5, no. 3, pp. 3937–3944, 2020.

[58] Z. Koszowska, G. Pittiglio, J. Chandler, M. Brockdorff, and P. Valdastri, "Mechanical reinforcement towards fully soft magnetic endoscopic endonasal surgical manipulators," EasyChair, Tech. Rep., 2022.

[59] E. W. Hawkes, L. H. Blumenschein, J. D. Greer, and A. M. Okamura, "A soft robot that navigates its environment through growth," *Science Robotics*, vol. 2, no. 8, eaan3028, 2017.

[60] M. M. Coad, L. H. Blumenschein, S. Cutler, *et al.*, "Vine robots," *IEEE Robotics & Automation Magazine*, vol. 27, no. 3, pp. 120–132, 2019.

[61] S. Al Harthy, H. Sadati, C. Girerd, *et al.*, "Tip-growing robots: Design, theory, application," *IEEE Transactions on Robotics*, 2024.

[62] J. Davy, T. P. Dean, N. J. Greenidge, *et al.*, "Magnetic fluid-driven vine robots for minimally invasive tissue biopsy sampling," *Advanced Intelligent Systems*, p. 2 400 827, 2025.

[63] P. Berthet-Rayne, S. H. Sadati, G. Petrou, *et al.*, "Mammobot: A miniature steerable soft growing robot for early breast cancer detection," *IEEE Robotics and Automation Letters*, vol. 6, no. 3, pp. 5056–5063, 2021.

[64] S. Goldstein, R. Jones, J. Sipe, J. Doppman, and J. Boretos, "A miniature toposcopic catheter suitable for small diameter tortuous blood vessels," *J Biomech Eng*, 1980.

[65] N. G. Kim, S. Park, D. Seo, *et al.*, "A soft growing robotic endoscope for painless and strain-free insertion," *Soft Robotics*, 2025.

[66] C. Suulker, S. Skach, D. Kaleel, *et al.*, "Soft cap for vine robots," in *2023 IEEE/RSJ International Conference on Intelligent Robots and Systems (IROS)*, IEEE, 2023, pp. 6462–6468.

[67] C. Girerd, A. Alvarez, E. W. Hawkes, and T. K. Morimoto, "Material scrunching enables working channels in miniaturized vine-inspired robots," *IEEE Transactions on Robotics*, 2024.

Chapter 2

Introduction

2.1 Thesis Aims

The overriding goal of thesis to explore fundamental methodologies for the design of surgical catheters with the potential to revolutionise minimally invasive surgical access. To do this, the thesis has the following aims:

- To explore methods for minimising tissue interaction when inserting surgical instruments into highly torturous vessels in the human anatomy. This should allow for highly dextrous catheters that are capable of reaching areas of the anatomy typically avoided.

- To develop a simulation model capable of being used in computational design frameworks for the design of magnetic continuum robots that shape-form to minimise interaction. This model will have to be specific to the case of the hard-magnetic materially-soft materials utilised in the design of magnetic continuum robots.

- To explore novel methodologies for the locomotion of magnetic continuum robots that minimise tissue interaction. This will include both shape-forming magnetic continuum robots but also robots built on the principle of everting vine robots which move without translation.

- To characterise, model and develop these robot designs in free-space and clinically relevant tissue phantoms towards pre-clinical and eventual translation of these novel surgical devices.

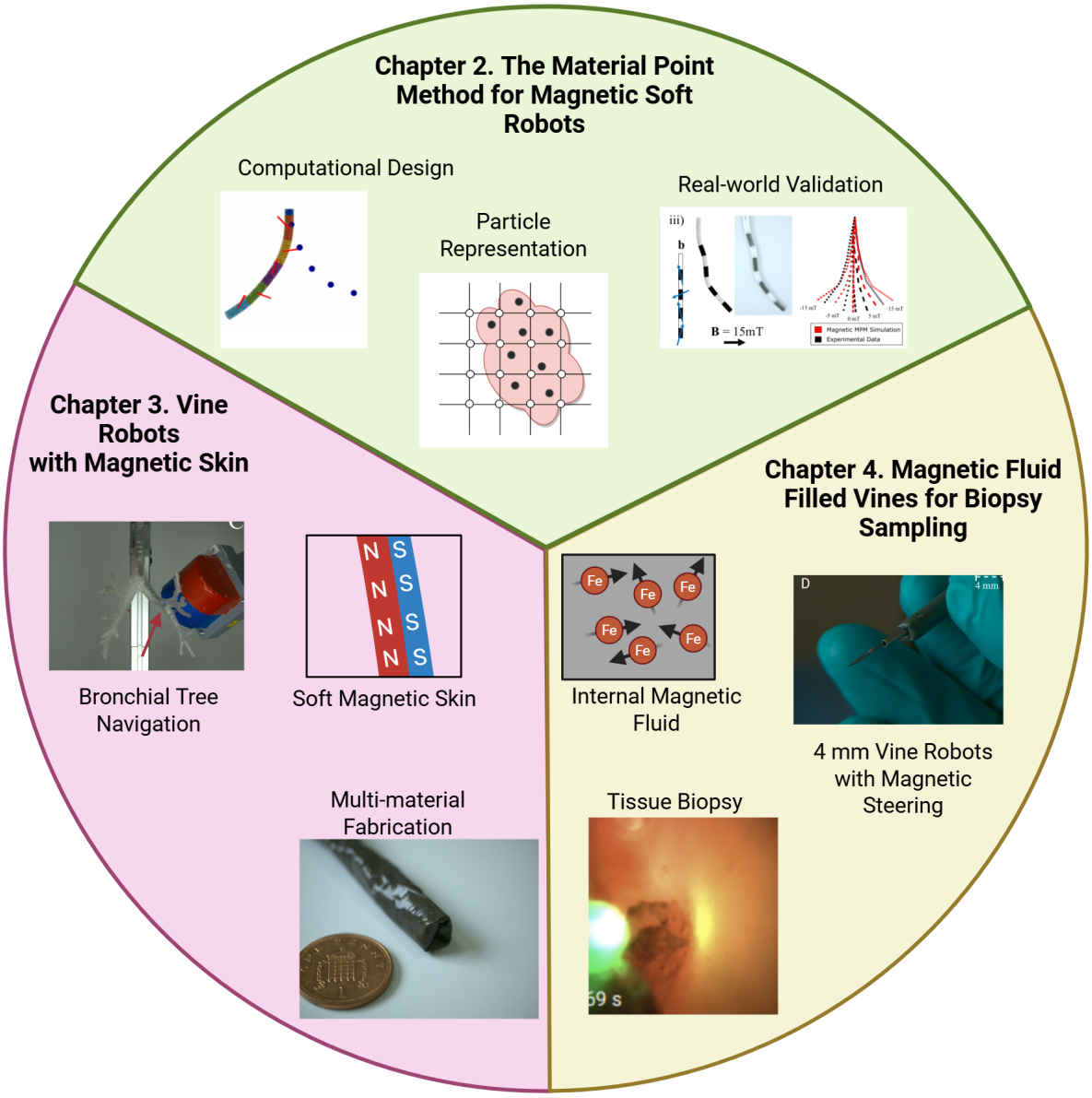

Figure 2.1: Graphical abstract covering the 3 content chapters of this Thesis. Chapter 2 covers a custom simulation framework for magnetic soft robots, Chapter 3 introduces vine robots and their steering via a magnetic skin, Chapter 4 considers vine robots steered via internal magnetic fluid.

2.2 Thesis Structure

The rest of this thesis is organised as follows with Chapters 2 - 4 presented as published work under the alternative style of PhD thesis at the University of Leeds.

Chapter 2 introduces a novel simulation framework for magnetic soft robots. This generalised open-source simulator is designed for representing the complex interactions of magnetic soft robots to close the reality-gap between prototype and model. This work presents the first use of the Material Point Method (MPM) for magnetic soft robots with distinct advantages over Finite Element Method (FEM) approaches. This simulator is general purpose however was developed with computational design frameworks in mind in order to enable the design of shape-forming tentacles for complex scenarios such as dynamic environments and tortuous anatomy.

Chapter 3 introduces a novel form of miniaturised magnetic robot combining the principles of vine robots with magnetic actuation. This work aims to address some of the challenges with shape-forming tentacle robots via utilising the environment to aid in navigation. We develop a robot of 8 mm diameter which can squeeze through small gaps and conform naturally to its anatomy. To steer the robot, we employ a magnetic "skin" for the vine robot formed of a silicone doped with magnetic micro-particles.

Chapter 4 begins by explaining limitations in the magnetic skin approach established in Chapter 2, however expresses the real benefits of robots with entirely soft structures. To this end, instead of embedding the surface of the vine with magnetic elements, this work utilises the internal growing medium of the robot. Here, we form a magnetic fluid out of a dispersion of magnetic elements. This creates a robot with high magnetic volume that can be easily steered and grown simultaneously.

Each of these chapters are prepended by a short **Commentary** explaining the placement of this published work in the chapter and appended by an **Evaluation** summarising the findings of the work. Chapter 5 contains reflections and conclusions linking the chapters of published work and providing guidance on future work. Figure 2.1 gives a overview of

the thesis structure.

Chapter 3

A Framework for Simulation of Magnetic Soft Robots using the Material Point Method

3.1 Chapter Commentary

This chapter introduces a 3D continuum mechanics framework specifically targeted at Magnetic Soft Robots (MSR). This framework enables dynamic simulations of robot behaviour and can well represent deforming magnetic soft bodies without relying on any rigid element assumptions. Furthermore, it allows for complex geometries and arbitrary magnetisation profiles. This framework is based on the Material Point Method (MPM), a continuum mechanics methodology based on a dual Eulerian-Lagrangian representation. Unlike FEM approaches, there is no mesh and instead a particle representation is used with an intermediary calculation step performed on a fixed grid. This creates an overall simpler algorithm to implement and avoids issues such as mesh-collapse. The framework handles large deformations and inherently represents self-collision. My direct contribution was to develop and implement the magnetic soft material models. In particular, to leveage the assumptions of an *ideal magnetically-hard hyper-elastic material* and for the first time

introduce this into a MPM framework. I developed this framework to aid in the creation of the shape-forming tentacle robots and therefore was developed with computational design in mind. This MPM based model can be utilised to allow for representation of complex geometries enabling both design of the magnetic profile and the form of the robot. A short workshop paper which forms a continuation of this work into a computational design framework is included in the Appendix.

The below manuscript is copied from: Davy, J., Lloyd, P., Chandler, J.H. and Valdastri, P., 2023. A framework for simulation of magnetic soft robots using the material point method. IEEE Robotics and Automation Letters, 8(6), pp.3470-3477.

3.2 Abstract

Simulation represents a key aspect in the development of robot systems. The ability to simulate behavior of real-world robots provides an environment where robot designs can be developed and control systems optimised. Due to the use of external magnetic fields for actuation, magnetic soft robots can be wirelessly controlled and are easily miniaturised. However, the relationship between magnetic soft materials and external sources of magnetic fields present significant complexities in modelling due to the relationship between material elasticity and magnetic wrench (forces and torques). In this work, we present a simulation framework for magnetic soft robots using the Material Point Method (MPM) which integrates hyper-elastic material models with the magnetic wrench induced under external fields. Compared to existing Finite Element Methods (FEM), the presented MPM based framework inherently models self-collision between areas of the model and can capture the effect of forces in non-homogeneous magnetic fields. We demonstrate the ability of the MPM framework to model the influence of magnetic wrench on magnetic soft robots, capture dynamic behavior of robots under time-varying magnetic fields, and provide an accurate representation of deformation when colliding with obstacles. We show the versatility of MPM framework by comparing simulations to a range of real-world magnetic soft robot designs previously presented in the literature.

3.3 Introduction

Magnetic Soft Robots (MSRs) are of interest due to the potential for miniaturisation afforded by off-board actuation [1]–[5]. By manipulating this magnetic field, the resultant wrench (forces and torques) on magnetic segments of the robot can be precisely controlled. This makes MSRs well suited to applications in surgery where the soft structure of the robot and small scale can enable them to reach areas of the anatomy unachievable by conventional tooling [6], [7]. MSRs can be formed by embedding permanent magnets or magnetic microparticles into soft elastomeric materials [8], [9]. The latter case is appealing due to the ability to retain an entirely soft structure. However, this scenario presents a challenging system to model with standard approaches due to material geometry, direction of magnetisation, external magnetic field and external forces all influencing the resultant deformation.

Finite element methods (FEM) have been used to model MSRs and represent a high accuracy approach capable of modeling hyper-elastic deformation under external fields while representing complex geometries [10][11]. MSRs, make use of *hard magnetic* materials which are defined by their remnant magnetisation once an external magnetising field is removed. In order to simplify the FEM modeling of MSRs, the assumption of discrete hard magnetic elements embedded within the soft material can be made [12][13]. However, this assumption is only valid on MSRs formed with discrete magnetic sections, and loses accuracy as the deformation of these sections increases [14]. Zhao et al. [11] addressed this significant problem by deriving a stress relationship for magnetically hard, mechanically soft materials and integrated it into FEM software (ABAQUS, Dassault Systèmes, France) allowing continuous, deformable magnetic profiles within the material [11]. By the combination of hyper-elastic models with the magnetic contribution of stress in the material, they demonstrate the accurate prediction of equilibrium deformation under constant fields. Nonlinear FEM analysis comes at significant computational cost due to the numerical iterative minimisation process. Furthermore, under large hyper-elastic deformation the mesh representation utilised in FEM can become distorted, leading to

erroneous results and poor convergence [15]. Ye et al. presented Magttice, a FEM-based lattice model by integrating the magnetic potential energy derived by Zhao et al. into a lattice mesh model [10]. They proceed to study the interaction between MSRs with fluids in time varying fields, noting the importance of considering gravity into the model to provide accurate deformation results.

As an alternative approach to FEM, the Material Point Method (MPM) is a hybrid Lagrangian, Eulerian model for continuum mechanics [16][17]. Unlike FEM, there is no underlying deforming mesh in the model. Instead MPM is a cyclical process which moves between a particle based representation and a fixed grid. The particle representation is utilised for internal material stress and the grid provides a structure to apply external forces. The lack of deforming mesh prevents the issue of mesh collapse under high deformation experienced in FEM. Unlike FEM, the use of discrete material points can implicitly handle self-collision and model fracturing and has found application in crack propagation of beams and the study of tissue-needle interaction [18][19]. The nature of this method suits the mass parallelisation of processing across multiple processors, as individual updates of particle and grid nodes can be considered independently and the effects summated. Further, due to the continuous nature of MPM, derivatives of the current state with respect to the initial model parameters can be obtained and utilised to guide optimisation to achieve desired behaviour [17].

In this work, we extend the MPM to cover magnetically hard, mechanically soft materials. Using this approach, we demonstrate the ability to model large deformations in MSRs under varying fields. Our system is capable of representing dynamic behavior and collisions in the environment, as well as the final equilibrium state in static fields. Additionally, as the MPM representation associates each particle with its own magnetisation vector, MSRs can be modeled with varied and near continuous magnetisation profiles. Thus, our methodology and simulation environment is capable of representing complex MSR scenarios and capturing their resultant behavior.

In an extension to previously presented FEM modeling, we showcase the ability to model

not just torques but also magnetic forces present caused by non-homogeneous magnetic fields. Unlike FEM approaches, self collision between model parts is implicit in the MPM allowing the physical interaction between segments of the robot to be studied. We further show how the MPM methodology means external forces can be easily integrated into the model providing realistic interactions with surfaces and obstacles.

We validate these models on fabricated MSRs and show agreement with the derived MPM model. We further showcase robot designs from the literature in the simulation framework and replicate behaviours as observed in reality. Open source examples of 3D implementation of the framework are available at `http://github.com/joshdavy1/magneticMPM`.

3.4 A review of the material point method.

MPM is an Eulerian-Lagrangian numerical method for continuum mechanics consisting of two material representations. The first, the Lagrangian representation consists of individual particles of a fixed mass and volume that represent discretised elements of the material. These elements are initially distributed evenly to represent the geometry of the material. The second is the grid representation, which can be considered as an undeformable Eulerian mesh, which is fixed in reference frame. This grid consists of regular node points, surrounding the material. The grid nodes are static in position and regularly spaced but represent a transfer of particle properties from one time-step to the next.

Transfers between representations are named Particle-to-Grid (P2G) (Fig. 3.1a) and Grid-to-Particle (G2P) (Fig. 3.1c), respectively. Our work extends the Moving Least Squares - Material Point Method (MLS-MPM) algorithm in order to represent the actuation experienced in magnetic materials [20]. The following gives an overview of the MLS-MPM; readers are referred to the works of [20] and [21] for an extensive overview and full derivations.

3.4.1 Particle (Lagrangian) Representation

Particles are initialised in order to represent the geometry of the soft robot and their position at time t is notated as $\mathbf{x}_p^t \in \mathbb{R}^3$. $\mathbf{v}_p^t \in \mathbb{R}^3$ represents the particle velocity vector and $\mathbf{C}_p^t \in \mathbb{R}^{3\times3}$ represents the affine velocity matrix [22]. A final variable $\mathbf{F}_p^t \in \mathbb{R}^{3\times3}$ represents the particle deformation gradient initialised to the identity matrix $\mathbf{F}_p^0 = \mathbb{I}$.

3.4.2 Particle to Grid (P2G)

In order to transfer the particle representation of the material to the grid, we must distribute the properties of the particle to the surrounding nodes (see Fig. 3.1b). To do this, a weighting function is utilised to specify the relative distribution of the particle property to the neighborhood nodes. Here, the properties are distributed using a quadratic B-spline kernel distributed to a 3x3x3 neighborhood of grid nodes given as

$$W(\Delta\mathbf{r}) = w(\Delta x)w(\Delta y)w(\Delta z) \tag{3.1}$$

where

$$w(\alpha) = \begin{cases} 0.75 - |\alpha/\delta x|^2 & 0 \leq |\alpha/\delta x| < 0.5 \\ 0.5(1.5 - |\alpha/\delta x|)^2 & 0.5 \leq |\alpha/\delta x| < 1.5 \\ 0 & 1.5 \leq |\alpha/\delta x| \end{cases} \tag{3.2}$$

[21]. Where $\Delta\mathbf{r} = [\Delta x, \Delta y, \Delta z]^T$ is the relative displacement between particle and the node at i, j, k as shown in Fig. 3.2. δx is the grid node spacing (See Fig. 3.2). $\alpha \in \{\Delta x, \Delta y, \Delta z\}$.

As such grid mass is distributed as

$$m_{i,j,k}^t = \sum_p W(\Delta\mathbf{r}) m_p, \tag{3.3}$$

where m_p is the particle mass equal to ρv_p where ρ is the material density and v_p is the particle volume. Grid momentum is calculated as

$$\mathbf{p}_{i,j,k}^{t} = \sum_{p} W(\Delta\mathbf{r})(m_p\mathbf{v}_p^t - (\frac{4}{\delta x^2}v_p\mathbf{P}_p^t(\mathbf{F}_p^t)^T + m_p\mathbf{C}_p^n)\Delta\mathbf{r}). \tag{3.4}$$

where $\mathbf{P}_p^t$ is the first Piola–Kirchhoff stress tensor [21].

3.4.3 Grid (Eulerian) Representation

After transfer to the grid representation, the effect of external forces are imposed (Fig. 3.1c). These external forces and the grid momentum can be integrated to form the grid velocity.

$$\mathbf{v}_{i,j,k}^{t} = \frac{1}{m_{i,j,k}^{t}}(\mathbf{p}_{i,j,k}^{t} + \mathbf{f}_{i,j,k}^{t}\Delta t), \tag{3.5}$$

where Δt is the simulation time stepping and $\mathbf{f}_{i,j,k}^{t}$ is the external force on the node. For all nodes where $m_{i,j,k}^{t} \neq 0$.

3.4.4 Grid to Particle (G2P)

After the velocities in the grid frame have been calculated, particle velocity and affine velocity can then be reconstructed utilising the same weighting kernel specified in Section 3.4.2 (Fig. 3.1d).

$$\mathbf{v}_p^{t+1} = \sum_i \sum_j \sum_k W(\Delta\mathbf{r})\mathbf{v}_{i,j,k}^{t}, \tag{3.6}$$

$$\mathbf{C}_p^{t+1} = \frac{4}{\delta x^2}\sum_i \sum_j \sum_k W(\Delta\mathbf{r})\mathbf{v}_{i,j,k}^{t}\Delta\mathbf{r}. \tag{3.7}$$

The deformation gradient of the particle and particle positions are updated, representing the overall change in deformation and pose of material in the time-step.

$$\mathbf{F}_p^{t+1} = (\mathbb{I} + \mathbf{C}_p^{t+1}\Delta t)\mathbf{F}_p^{t} \tag{3.8}$$

$$\mathbf{x}_p^{t+1} = \mathbf{x}_p^{t} + \mathbf{v}_p^{t+1}\Delta t \tag{3.9}$$

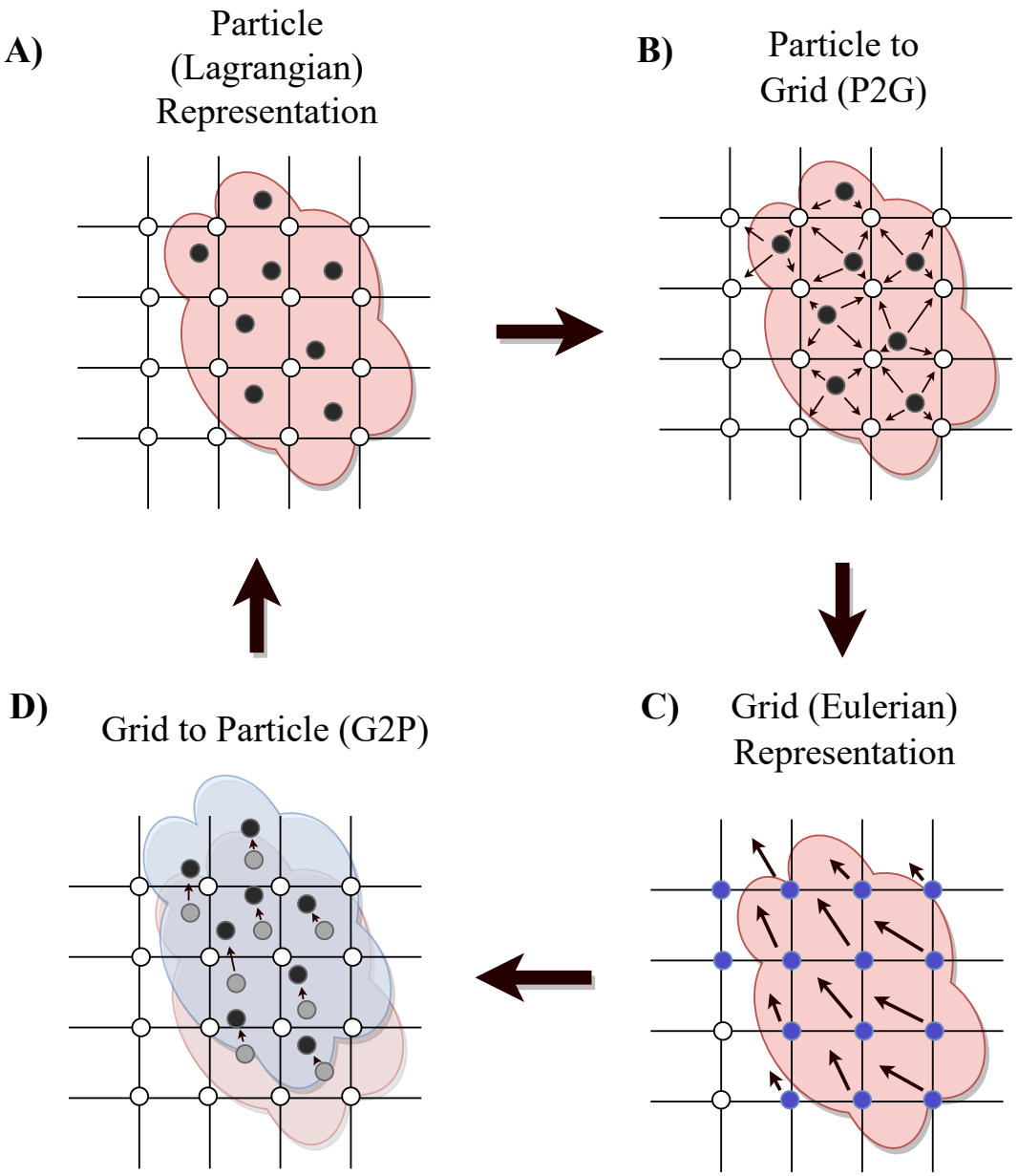

Figure 3.1: The cyclical method followed by MPM. a) Internal forces and magnetic stress are computed in the particle domain. b) Particle properties are transferred to grid representation. c) External interaction and forces due to magnetic gradients are computed in the grid domain. d) Particle properties are reconstructed from the grid.

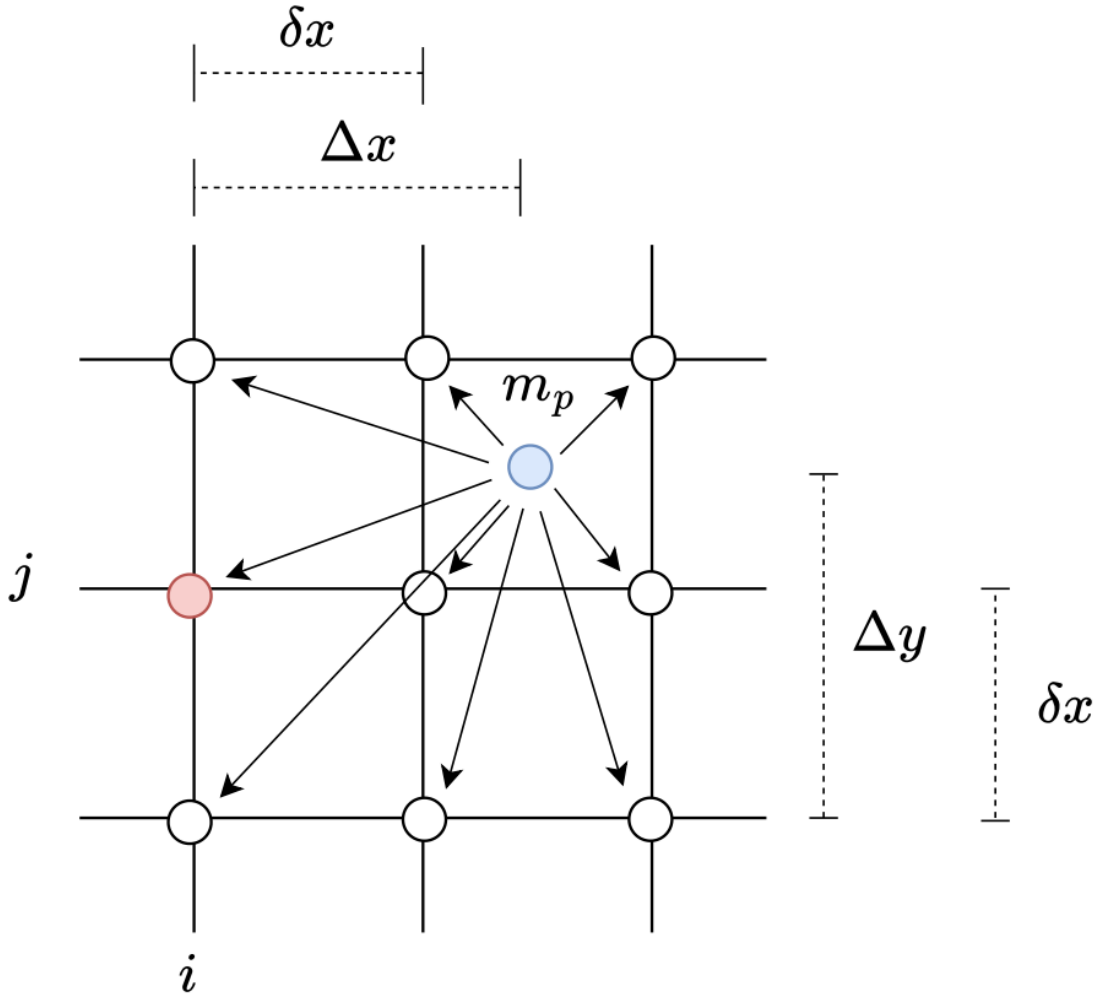

Figure 3.2: 2D illustration of the distribution of particle (blue) properties in the P2G step to the node i, j (red) utilising the Quadratic B-spline kernel [21].

3.5 Modelling of magnetically hard, mechanically soft materials.

We consider the modeling of elastomers embedded with magnetic elements, common in soft robotics. Typically, this consists of a silicone prepolymer mixed with hard magnetic microparticles (commonly NdFeB due to its high remnant magnetisation). This mixture is then cast into molds of the desired form of the magnetic robot and set [23]. The cast is then subjected to a saturating magnetising field in order to set the direction of magnetisation. After being removed from the field, the material retains a remnant magnetisation.

In this work we consider this material as an *ideal hard-magnetic soft material* [11]. The self-interaction between the magnetic elements of the MSR is neglected. This has shown to be a valid assumption for modelling deformation of the MSR due to the relative weakness of this interaction compared to the interaction with larger external magnetic fields [10][23].

3.5.1 Elastomeric Properties

For modelling the elastic properties of the material the Neo-Hookean elastic model is adopted which has been shown to accurately model the stress-strain relationship of magnetic soft materials in the strain ranges experienced in soft robotic applications [24]. The Neo-Hookean model is given as

$$\mathbf{P}^t_{p,elastic} = GJ^{-2/3}(\mathbf{F}^t_p - \frac{I_1}{3}(\mathbf{F}^t_p)^{-T}) + KJ(J-1)(\mathbf{F}^t_p)^{-T}. \tag{3.10}$$

where $\mathbf{P}^t_{p,elastic}$ is the elastic contribution of the first Piola-Kirchoff stress tensor, G is the shear modulus of the material and K is the bulk modulus. J = determinant$(\mathbf{F}^t_p)$ and I_1 = trace$(\mathbf{F}^{t^T}_p \mathbf{F}^t_p)$. In order to satisfy the assumption of near incompressibility of the utilised silicone polymers we chose the bulk modulus to be a sufficiently high value. In

this case we set $K = 20G$. At the strain/scale ranges relevant to our MSRs, the actual value of the bulk modulus does not largely affect the final deformation [10][11].

3.5.2 Magnetic Properties

A magnetic agent under external magnetic fields will experience an aligning torque between the magnetic moment and the external field.

$$\boldsymbol{\tau} = \mathbf{m} \times \mathbf{B} \tag{3.11}$$

where $\mathbf{B}$ is the external magnetic field and $\mathbf{m}$ is the magnetic moment vector equal to $\frac{\mathbf{B}_r V}{\mu_o}$ where V is the volume of the agent. μ_0 is the vacuum permeability equal to $4\pi \times 10^{-7}$ Hm^{-1} and $\mathbf{B}_r$ is the remnant magnetisation vector.

Further, in the case of a non-homogeneous magnetic field, the agent will experience a force,

$$\mathbf{f} = \nabla(\mathbf{B} \cdot \mathbf{m}). \tag{3.12}$$

This force is proportional to the spatial gradient of the magnetic field and is at maximum with alignment of the magnetic moment and external field.

In the FEM approach outlined by Zhao et al. [11] the effect of aligning torque under homogeneous magnetic fields is integrated into the elastic model via an additional stress. We utilise this stress along with the Neo-hookean model into the P2G step of the MPM cycle. This, in the first Piola-Kirchoff form is

$$\mathbf{P}^t_{p,magnetic} = -\frac{1}{\mu_0}\mathbf{B} \otimes \mathbf{B}_{r_p}, \tag{3.13}$$

where $\otimes$ is the dyadic product and $\mathbf{B}_{r_p}$ is the remnant magnetic flux density associated with the particle. Leading to an overall material stress as

$$\mathbf{P}^t_p = \mathbf{P}^t_{p,elastic} + \mathbf{P}^t_{p,magnetic}. \tag{3.14}$$

By incorporating the magnetic stress effect into the P2G step, the effect of the realigning torque can be incorporated into the MPM. However, the forces induced in non-homogeneous magnetic fields are not covered. Therefore the magnetic force is incorporated as an external force in the grid velocity calculation. To calculate the force at the grid node, we calculate the equivalent magnetic moment of the node as a product of the volume of magnetic particles using the same weightings as described in the P2G Section 3.4.2.

$$\mathbf{m}_{i,j,k}^{t} = \frac{v_p}{\mu_0} \sum_{p} W(\Delta \mathbf{r}) \widetilde{\mathbf{B}}_{r_p}. \tag{3.15}$$

where $\widetilde{\mathbf{B}}_{r_p}$ is the remnant magnetic flux density rotated into the current reference frame equal to $\frac{1}{J}\mathbf{F}_p^t \mathbf{B}_{r_p}$.

The external magnetic force can then be derived as

$$\mathbf{f}_{magnetic} = \nabla \mathbf{B}_{i,j,k}{}^{T} \cdot \mathbf{m}_{i,j,k}^{t}, \tag{3.16}$$

where $\nabla \mathbf{B}_{i,j,k}$ is the spatial gradient of the magnetic field at the node.

3.5.3 Material Damping

Damping is the energy dissipation of the material and represents numerous complex phenomena (viscosity, air resistance, heat exchange etc.). To capture these properties of magnetic soft materials, we model damping by adding a force proportional to the current grid momentum,

$$\mathbf{f}_{damping} = -c\mathbf{p}_{i,j,k}^{t} \tag{3.17}$$

where c is the damping constant. This external force will lead the material to a final equilibrium pose given a static applied field.

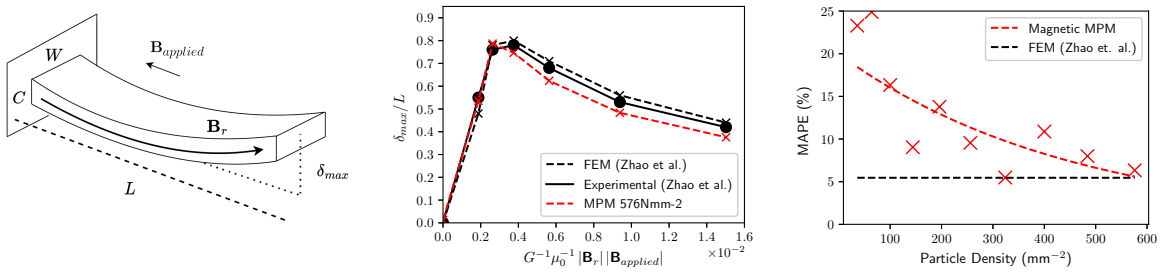

(a) (b) (c)

Figure 3.3: High deformation magnetic soft beam experiment as presented by Zhao et al [11]. (a) The applied field $\mathbf{B}_{applied}$ is in the opposite direction to the remnant magnetisation $\mathbf{B}_r$ of the soft material leading to high deflection. (L = 17.2 mm, C = 0.84 mm, W = 5 mm). (b) Magnetic MPM methodology compared with experimental results and FEM analysis [11] $G^{-1}\mu_0^{-1}|\mathbf{B}_r|$ is a constant which leads these results to be independent of material parameters. (c) Mean Absolute Percentage Error (MAPE) converges with increased particle density.

Therefore the full set of external forces introduced to the grid operations step is

$$\mathbf{f}^t_{i,j,k} = \mathbf{f}_{magnetic} + \mathbf{f}_{damping} + \mathbf{f}_{gravity} \tag{3.18}$$

$$\mathbf{f}^t_{i,j,k} = \nabla \mathbf{B}_{i,j,k}{}^T \cdot \mathbf{m}^t_{i,j,k} - c\mathbf{p}^t_{i,j,k} + m^t_{i,j,k}\mathbf{g} \tag{3.19}$$

where $\mathbf{g}$ is the acceleration due to gravity.

It is worth noting that the proposed extension of MPM to model magnetic soft materials requires three readily obtained material parameters. These are the material density, the magnetic remanence, and the shear modulus of the material. However, the damping constant is more difficult to obtain. In magnetics, the interest is often in the final equilibrium state of the robot, and therefore a damping parameter leading to a fast settle time of the system is most appropriate. This can be obtained through iterative experimentation. In the case where accurate representation of dynamics is required a methodology such as followed by Shariati et al. may be utilised [25].

3.6 Experimental Verification

3.6.1 Implementation

The above stated magnetic MPM algorithm was implemented in the Taichi programming language [26]. Taichi was selected due to supporting GPU parallelisation and Python-esque syntax. All examples were run on an NVIDIA Quadro RTX 4000 GPU.

The choice of time-step significantly affects the speed of simulation and a maximum time-stepping should be chosen that retains model stability. As derived in [27], the maximum time stepping for MPM is

$$\Delta t_{max} = C\delta x\sqrt{\frac{\rho}{3G}} \tag{3.20}$$

where C is a constant close to one. It is evident that the time-stepping can be increased by utilising large grid node spacing. However, this limits the fidelity in which external forces can be incorporated. A balance must be found between grid node spacing and simulation speed. It can also be observed from (3.20) that the stiffer, less dense materials lead to a lower maximum time-stepping. The number of particles N, further effects the simulation performance. Low particle numbers fail to fully represent the deformation of the robot, while high numbers will add significant computation time. The generation of the initial pose of the particles is performed by uniformally distributing particles in the geometry of the structure. This is performed via sampling 3D models of the robot. We first validate our methodology empirically on planar models; verifying agreement with real world behaviour. We then present a full 3D implementation of the magnetic MPM framework and showcase simulations of MSRs from the literature. All material parameters were obtained following the methodology of [24].

3.6.2 Magnetic Beam Deformation

To validate the approach, we recreate the high deformation beam bending experiment presented by Zhao et al. [11]. A magnetically hard materially soft beam (G = 303 kPa,

$|\mathbf{B}_r| = 0.258$ T) manufactured from PDMS (Sylgard 184) is placed in a external magnetic field. The direction of applied field is parallel yet opposite to the remnant magnetisation vector of the beam (See Fig. 3.3a); causing a deflection under increasing field strength. We recreate this scenario in our framework with a varying particle density to represent the beam ($\delta x = 0.3$ mm, $\Delta t = 6 \times 10^{-6}$ s). We then compare the resultant deflection δ_{max}/L with the experimental data and FEM results provided by the authors (See Fig. 3.3b). Fig. 3.3c shows how the results converge with particle density leading to a 6.1% Mean Absolute Percentage Error (MAPE) with a particle density of 576 mm^{-2}. This data informed choices on particle density in the following experiments.

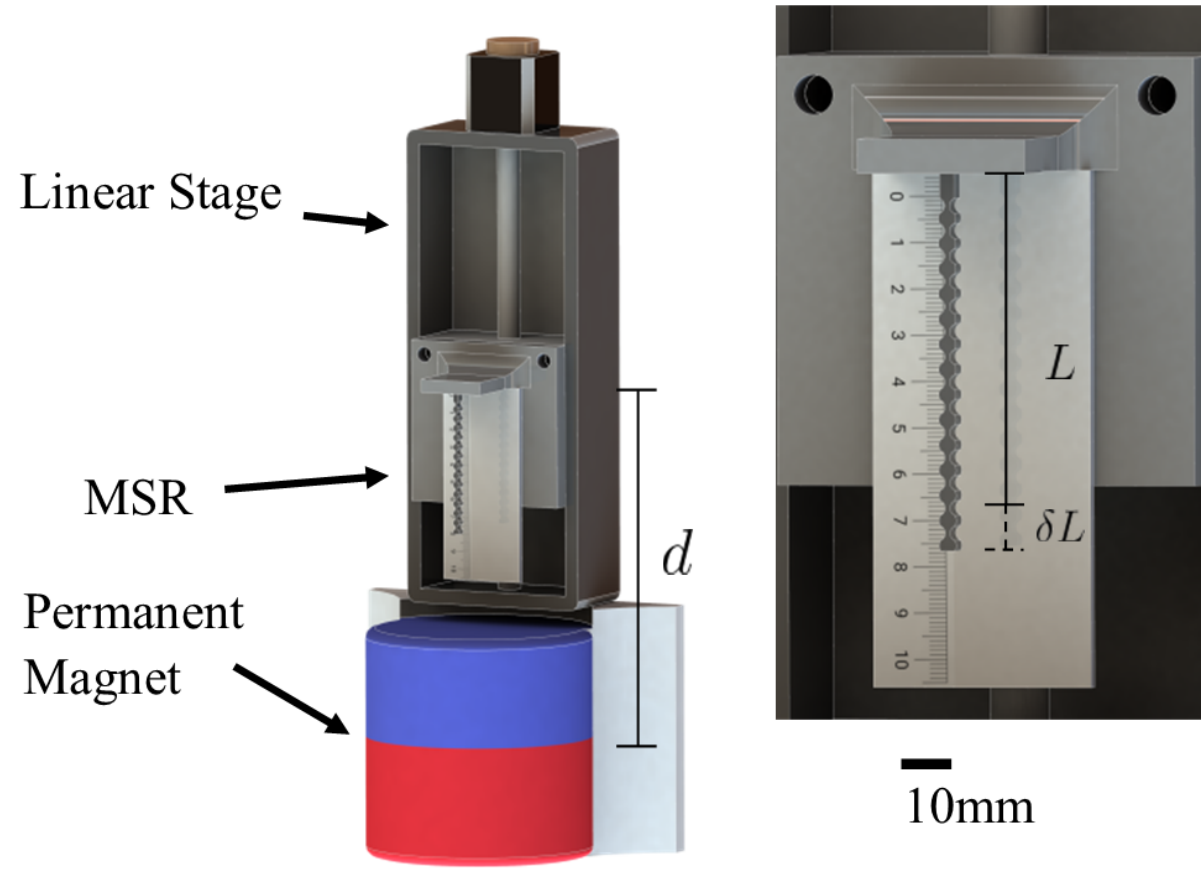

Figure 3.4: Experimental setup for measuring the deformation of the MSR due to gradient forces. A linear stage moves the robot closer to the permanent magnet where gradient forces are stronger. This causes an extension of length in the MSR.

3.6.3 Deformation under Non-homogeneous Magnetic Fields.

To verify the ability of the MPM framework to model forces experienced due to magnetic field gradients the interaction between a permanent magnet and a MSR is studied. The robot was magnetised along its main axis and placed vertically above a 100 mm x 100 mm cylindrical neodymium magnet with a remanence of 1.44 T (See Fig. 3.4). The MSR is fabricated from Ecoflex-30 silicone polymer (Smooth-On, Inc., U.S.A.) mixed with NdFeB microparticles in a 1:1 mass ratio ($G = 33$ kPa, $|\mathbf{B}_r| = 0.101$ T, $\rho = 1840$ kgm^{-3}). In this configuration, no magnetic torques are present due to the alignment of the robot's magnetisation with the permanent magnet. The design of the MSR has periodic thickness in order to give an exaggerated deformation compared to a simple beam. Thicker sections increase the overall magnetic moment whilst thinner sections give larger strain due to lower elastic forces. The MSR is mounted to a linear stage allowing the introduction of the robot towards the magnet. As the robot is moved towards the magnet, larger magnetic fields gradients are present which causes an extension of robot length. This strain is compared to the same experimental setup in simulation ($\delta x = 2$ mm, $\Delta t = 1 \times 10^{-6}$ s, $N = 15,359$). A model of the magnetic field from a cylindrical permanent magnet is provided by Magpylib [28] and finite differences are used to obtain the spatial gradient of the magnetic field.

Fig. 3.5 shows the results from simulation and experimental setup. Due to the alignment of the magnetic field and magnetisation of the robot, the gradient effect can be independently observed. The results are in strong agreement and the error at lower distances to the magnet can be attributed to limitations in magnetic field modelling and accuracy of hyper-elastic model rather then an inherent fault in methodology.

3.6.4 Interaction with External Bodies.

The MPM implicitly handles self-collision between material points. This is a significant advantage over FEM methods which require additional interpolation between mesh vertices to handle this self collision. In the MPM framework, external forces can be in-

tegrated into the model in the grid representation. To demonstrate the ability to model interaction with external entities we consider the deformation of an axially magnetised MSR under contact with a rigid obstacle. This is represented in the grid representation stage by setting the grid velocity to zero at the obstacle boundary on collision with the obstacle,

$$\mathbf{v}_{out} = \begin{cases} \mathbf{0} & \text{if } \mathbf{v}_{in_{\parallel}} \geq 0, \\ \mathbf{v}_{in} & \text{otherwise.} \end{cases} \tag{3.21}$$

where $\mathbf{v}_{in}$ is the incoming velocity calculated in Equation (3.5) and $\mathbf{v}_{out}$ is the velocity used in particle property reconstruction in section 3.4.4. $_{\parallel}$ represents the parallel component of the velocity vector between the obstacle and the MSR.

A MSR of dimensions 60x3x3 mm is fabricated from Dragonskin-10 silicone polymer (Smooth-On, Inc., U.S.A.) mixed with NdFeB microparticles in a 1:1 mass ratio, ($G =$

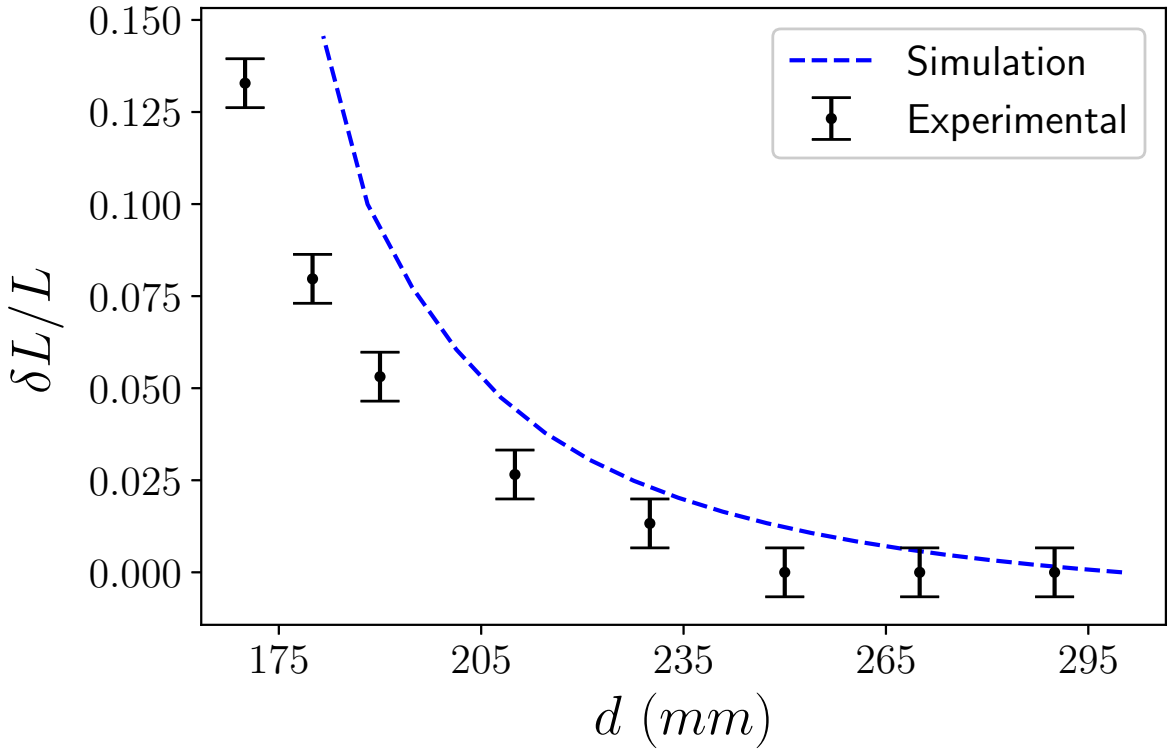

Figure 3.5: Comparison of simulation and experimental results for the deformation of the robot as described in Section 3.6.3 due to increasing field gradient forces as its introduced towards the magnet.

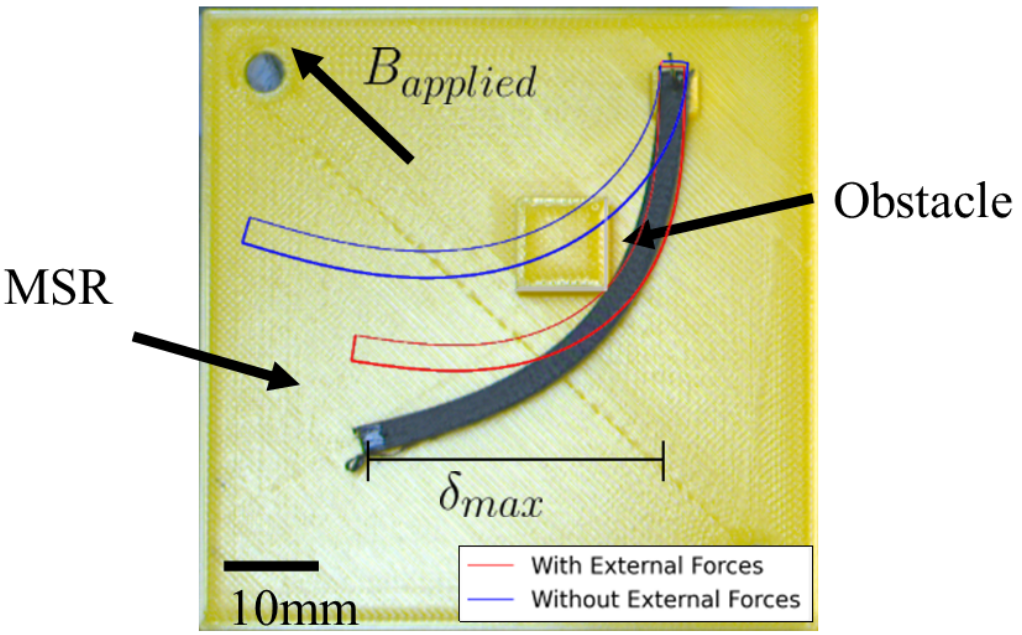

Figure 3.6: Experimental setup measuring deformation when interacting with external obstacles. Red and blue outlines represent the resultant deformation under the applied magnetic field, considering and not considering the interaction with the obstacle respectively. $|\mathbf{B}_{applied}| = 10$ mT.

120 kPa, $|\mathbf{B}_r| = 0.125$ T, $\rho = 1882$ kgm^{-3}) [24]. The MSR is axially magnetised and deflected via an applied magnetic field from a resting state under gravity to collide with a plastic obstacle (See Fig. 4.10). Fig. 3.7 shows normalised maximum deflection δ_{max}/L with increasing applied magnetic field, when considering the external object in the MPM framework. At large deflection, a larger difference in tip position can be noted. This can be attributed to the accuracy of the underlying hyper-elastic model (Equation (A.1) at high deformation.

3.6.5 Magnetic Soft Robots from the Literature.

MSRs vary from the sub-millimetre to larger centimetre-scale [2][6][23][29]. In this section, we showcase the utility of our MPM-framework by replicating designs of MSRs as presented in the literature.

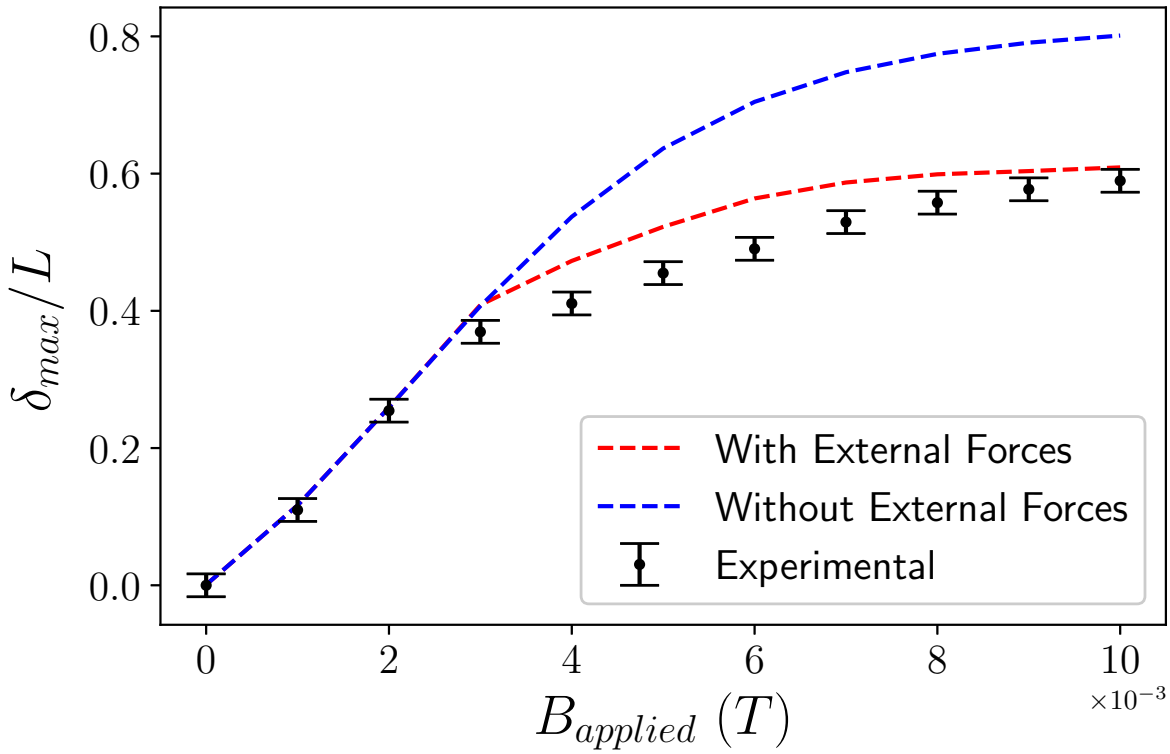

Figure 3.7: Comparison of maximum normalised deflection δ_{max}/L of the MSR with experimental results when external interaction is considered. ($\delta x = 2$ mm, $\Delta t = 5 \times 10^{-5}$ s, $N = 11,520$)

3.6.5.1 Continuum MSR (Pittiglio et al [23])

We first consider the continuum MSR presented by Pittiglio et al. [23]. These robots are formed of alternating magnetic and non-magnetic sections. The direction of the magnetisation vector of each section is decided by an optimisation algorithm to give a desired shape under a given magnetic field. We reproduce the continuum MSR in simulation and applied the same magnetic profile as presented ($\delta x = 1$ mm, $\Delta t = 2 \times 10^{-5}$ s, $c = 200$ s^{-1}, $N = 118,271$) with two magnetisation profiles (**a** and **b**). Material parameters were obtained from the work, and a damping parameter was chosen to provide fast equilibrium of the system. In Fig. 3.8a it can be observed that under the same magnetic field with matching profiles, the simulation and real robot produce deformations closely matching the real world behaviour. (See Supplementary Video).

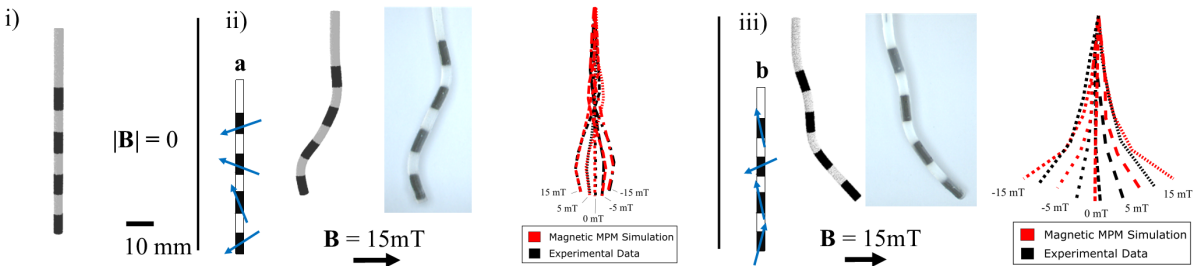

(a) Simulation of continuum MSR developed by Pittiglio et al. [23]. i) MSR under no external field. ii) Deformation under field in simulation with magnetisation profile **a** (left), deformation under field in experimental setup with fabricated MSR (center) and transient behaviour under magnetic field sweep (right). Mean tip positional error across sweep = 0.38 mm. iii) Deformation under field in simulation with magnetisation profile **b** (left) and deformation under field in experimental setup with fabricated MSR. (center) and transient behaviour under magnetic field sweep (right). Mean tip positional error across sweep = 6.97 mm. MSR length = 80 mm.

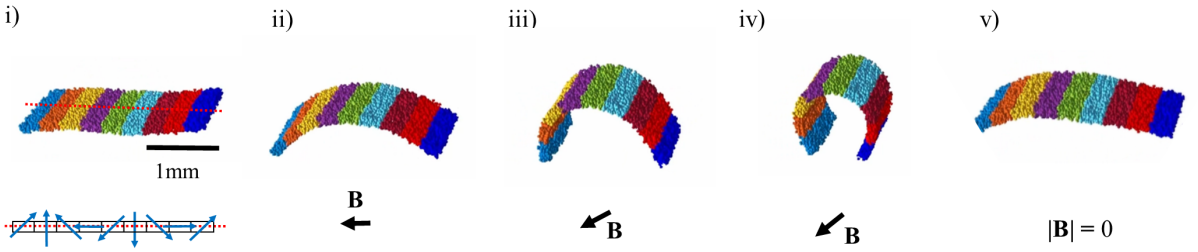

(b) The small scale soft robot presented by Hu et al. [29], in the presented simulation framework, demonstrating the 'walking' behaviour discussed in the author's work as the magnetic field is rotated. i) Magnetisation profile $|\mathbf{B}_{max}| = 8$ mT.

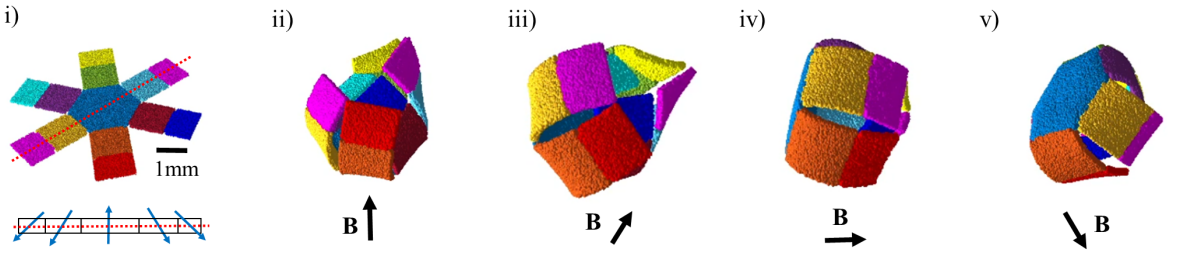

(c) The six arm untethered gripper presented by Xu et al. [13]. Applying a magnetic field perpendicular to the robot causes it to grasp shut. Once shut, rotating the magnetic field causes the robot to roll. The self-collision between model parts is inherent in our methodology. i) Magnetisation profile. $|\mathbf{B}| = 15$ mT, $\omega = 10$ Hz.

Figure 3.8: MSRs from the literature represented in the MPM framework.

3.6.5.2 Small scale soft robot (Hu et al. [29])

We reproduce the MSR designed by Hu et al. [29] in our framework and make use of the collision model of Equation (3.21) to represent a floor with which the robot can interact ($\delta x = 0.1$ mm, $\Delta t = 7 \times 10^{-7}$ s, $c = 180$ s^{-1}, $N = 10{,}260$). The robot presented by the authors is formed of a continuous magnetic profile along its length; we represent this as a series of nine sections with a matching magnetic profile (See Fig. 3.8b). By applying a rotating external magnetic field of varying magnitude, the 'walking' behavior observed by the authors is recreated. The ability to replicate this complex behaviour in simulation shows the potential of the MPM framework to iteratively design and test MSRs when compared to complex fabrication and experimental setups in reality. (See Supplementary Video).

3.6.5.3 Six armed untethered gripper (Xu et. al. [13])

The final example taken from the literature is the six-armed untethered gripper robot presented by Xu et al. [13]. This robot consists of 13 magnetic sections each with it's own magnetisation vector. On the application of a magnetic field perpendicular to the undeformed robot, the robot folds up and is capable of grasping small objects. The direction of magnetic field can be rotated and the robot will then roll in the direction of rotating field of angular frequency $\omega = 10$ Hz. This behavior is recreated in Fig. 3.8c and shown in the Supplementary Video. ($\delta x = 0.1$ mm, $\Delta t = 5 \times 10^{-7}$ s, $c = 20$ s^{-1}, $N = 103,430$). The grasping behaviour of the robot is a product of the self-collision between the robot's arms. This behavior is inherent in the MPM algorithm unlike FEM approaches which require additional computation to interpolate meshes and calculate these interaction forces. (See Supplementary Video).

3.7 Conclusion

In this work, we have presented a novel methodology for simulating MSRs. The Material Point Method (MPM) is capable of accurately representing the deformation experienced

in magnetic soft materials at high deformation in the presence of external magnetic fields. Unlike FEM approaches, MPM implicitly represents self-collisions in the material, allowing MSRs that rely on self-interaction to be represented. Further, our methodology has extended what was capable with existing systems by integrating the magnetic forces experienced in non-homogeneous magnetic fields. We have validated the methodology and show strong agreement (6.1% MAPE, Fig 3.3c) with real-world deformation at large strains. Further, comparison with MSRs from the literature showcases the ability of the presented methodology to replicate the complex behaviour seen in the real robots in simulation.

Existing simulation frameworks for MSRs have often relied on proprietary, closed-source or unreleased implementations. We have made implementation examples of our magnetic MPM framework available in order to allow others to utilise our methodology. Robots can be generated from 3D CAD models with specification of the magnetic profile of each section. The ability to test ideas quickly in simulation (when compared to fabrication and experimental setups), allows the fast iterative design of MSRs. When paired with the ability to model external forces and obstacles, designs can be explored and modified, and complex behaviors can be tested. By releasing our implementation, we hope others developing simulation frameworks can provide direct comparisons with our work.

Our framework is well suited to use as an environment for optimisation or training machine learning systems, which can then be applied in reality. For example, the continuum MSRs of Pittiglio et. al. [23] were optimised using simplified rigid-link models. Utilising more accurate modelling would allow these designs to closer match the desired objective or incorporate dynamic behaviour under the influence of transient magnetic fields. The mass parrelisation of our implementation, leads to efficient run-times by utilising GPU processing.

Unlike FEM, the MPM is a continuous function of the initial variable values. This fact was exploited by Hu et al. [17], to develop a fully differentiable physics simulation to reduce the number of iterations for convergence of design optimisation. This could be

replicated with our methodology to optimise parameters such as magnetic profile, robot geometry and applied field efficiently.

The presented methodology only considers the interaction between the material's magnetic field and the externally applied actuating field. This neglects any self-interaction between discrete magnetic robot segments. This assumption is suitable for the cases in our experimental verification but, for other MSR designs that may rely on this interaction, their behaviour may not be accurately. An example of this could be the interactive forces between multiple MSRs in the same workspace [27]. Future work could consider the field generated by individual magnetic segments in order to better represent this characteristic. This would, of course, add significant algorithmic and computational complexity to the simulation.

The inherent ability to represent collision between particles in MPM could be utilised to consider the interaction between MSRs and external soft bodies. This is of particular interest due to the clinical applications of MSRs, in order to study the interaction between robots and soft tissues.

References

[1] Y. Kim and X. Zhao, "Magnetic soft materials and robots," *Chemical Reviews*, vol. 122, no. 5, pp. 5317–5364, 2022.

[2] M. Sitti, "Miniature soft robots—road to the clinic," *Nature Reviews Materials*, vol. 3, no. 6, pp. 74–75, 2018.

[3] D. Liu, X. Liu, Z. Chen, *et al.*, "Magnetically driven soft continuum microrobot for intravascular operations in microscale," *Cyborg and Bionic Systems*, vol. 2022, 2022.

[4] J. Lu, Y. Liu, W. Huang, K. Bi, Y. Zhu, and Q. Fan, "Robust control strategy of gradient magnetic drive for microrobots based on extended state observer," *Cyborg and Bionic Systems*, 2022.

[5] C. Huang, Z. Lai, X. Wu, and T. Xu, "Multimodal locomotion and cargo transportation of magnetically actuated quadruped soft microrobots," *Cyborg and Bionic Systems*, vol. 2022, p. 0004, 2022.

[6] E. Diller and M. Sitti, "Micro-scale mobile robotics," *Foundations and Trends® in Robotics*, vol. 2, no. 3, pp. 143–259, 2013, ISSN: 1935-8253.

[7] Q. Boehler, S. Gervasoni, S. L. Charreyron, C. Chautems, and B. J. Nelson, "On the workspace of electromagnetic navigation systems," *IEEE Transactions on Robotics*, pp. 1–17, 2022. DOI: 10.1109/TRO.2022.3197107.

[8] Y. Kim, G. A. Parada, S. Liu, and X. Zhao, "Ferromagnetic soft continuum robots," *Science Robotics*, vol. 4, no. 33, eaax7329, 2019. eprint: https://www.science.org/doi/pdf/10.1126/scirobotics.aax7329. [Online]. Available: https://www.science.org/doi/abs/10.1126/scirobotics.aax7329.

[9] P. Lloyd, G. Pittiglio, J. H. Chandler, and P. Valdastri, "Optimal design of soft continuum magnetic robots under follow-the-leader shape forming actuation," in *2020 International Symposium on Medical Robotics (ISMR)*, IEEE, 2020, pp. 111–117.

[10] H. Ye, Y. Li, and T. Zhang, "Magttice: A lattice model for hard-magnetic soft materials," *Soft Matter*, vol. 17, no. 13, pp. 3560–3568, 2021.

[11] R. Zhao, Y. Kim, S. A. Chester, P. Sharma, and X. Zhao, "Mechanics of hard-magnetic soft materials," *Journal of the Mechanics and Physics of Solids*, vol. 124, pp. 244–263, 2019.

[12] R. Dreyfus, Q. Boehler, and B. J. Nelson, "A Simulation Framework for Magnetic Continuum Robots," *IEEE Robotics and Automation Letters*, vol. 7, no. 3, pp. 8370–8376, Jun. 2022.

[13] T. Xu, J. Zhang, M. Salehizadeh, O. Onaizah, and E. Diller, "Millimeter-scale flexible robots with programmable three-dimensional magnetization and motions," *Science Robotics*, vol. 4, no. 29, eaav4494, 2019.

[14] S. Jeon, A. K. Hoshiar, K. Kim, *et al.*, "A magnetically controlled soft microrobot steering a guidewire in a three-dimensional phantom vascular network," *Soft*

Robotics, vol. 6, no. 1, pp. 54–68, 2019, PMID: 30312145. eprint: https://doi.org/10.1089/soro.2018.0019. [Online]. Available: https://doi.org/10.1089/soro.2018.0019.

[15] J. Danczyk and K. Suresh, "Finite element analysis over tangled simplicial meshes: Theory and implementation," *Finite Elements in Analysis and Design*, vol. 70-71, pp. 57–67, 2013, ISSN: 0168-874X. DOI: https://doi.org/10.1016/j.finel.2013.04.004.

[16] W. T. Sołowski, M. Berzins, W. M. Coombs, *et al.*, "Chapter two - material point method: Overview and challenges ahead," in ser. Advances in Applied Mechanics, S. P. Bordas and D. S. Balint, Eds., vol. 54, Elsevier, 2021, pp. 113–204. [Online]. Available: https://www.sciencedirect.com/science/article/pii/S0065215620300120.

[17] Y. Hu, J. Liu, A. Spielberg, *et al.*, *Chainqueen: A real-time differentiable physical simulator for soft robotics*, 2018. DOI: 10.48550/ARXIV.1810.01054. [Online]. Available: https://arxiv.org/abs/1810.01054.

[18] F. Sun, G. Wang, L. Zhang, R. Wang, T. Cao, and X. Ouyang, "Material point method for the propagation of multiple branched cracks based on classical fracture mechanics," *Computer Methods in Applied Mechanics and Engineering*, vol. 386, p. 114 116, 2021, ISSN: 0045-7825. [Online]. Available: https://www.sciencedirect.com/science/article/pii/S0045782521004473.

[19] M. Li, Y. Lei, D. Gao, Y. Hu, and X. Zhang, "A novel material point method (mpm) based needle-tissue interaction model," *Computer Methods in Biomechanics and Biomedical Engineering*, vol. 24, no. 12, pp. 1393–1407, 2021, PMID: 33688750. eprint: https://doi.org/10.1080/10255842.2021.1890047. [Online]. Available: https://doi.org/10.1080/10255842.2021.1890047.

[20] Y. Hu, Y. Fang, Z. Ge, *et al.*, "A moving least squares material point method with displacement discontinuity and two-way rigid body coupling," *ACM Transactions on Graphics*, vol. 37, no. 4, p. 150, 2018.

[21] C. Jiang, C. Schroeder, J. Teran, A. Stomakhin, and A. Selle, "The material point method for simulating continuum materials," in *ACM SIGGRAPH 2016 Courses*, ser. SIGGRAPH '16, Anaheim, California: Association for Computing Machinery, 2016, ISBN: 9781450342896. [Online]. Available: https://doi.org/10.1145/2897826.2927348.

[22] C. Jiang, C. Schroeder, A. Selle, J. Teran, and A. Stomakhin, "The affine particle-in-cell method," *ACM Transactions on Graphics (TOG)*, vol. 34, no. 4, pp. 1–10, 2015.

[23] G. Pittiglio, P. Lloyd, T. da Veiga, *et al.*, "Patient-specific magnetic catheters for atraumatic autonomous endoscopy," *Soft Robotics*, 2022.

[24] T. Da Veiga, J. H. Chandler, G. Pittiglio, *et al.*, "Material characterization for magnetic soft robots," in *2021 IEEE 4th International Conference on Soft Robotics (RoboSoft)*, IEEE, 2021, pp. 335–342.

[25] A. Shariati, J. Shi, S. Spurgeon, and H. A. Wurdemann, "Dynamic modelling and visco-elastic parameter identification of a fibre-reinforced soft fluidic elastomer manipulator," in *2021 IEEE/RSJ International Conference on Intelligent Robots and Systems (IROS)*, IEEE, 2021, pp. 661–667.

[26] Y. Hu, T.-M. Li, L. Anderson, J. Ragan-Kelley, and F. Durand, "Taichi: A language for high-performance computation on spatially sparse data structures," *ACM Trans. Graph.*, vol. 38, no. 6, Nov. 2019, ISSN: 0730-0301. [Online]. Available: https://doi.org/10.1145/3355089.3356506.

[27] Y. Fang, Y. Hu, S.-M. Hu, and C. Jiang, "A temporally adaptive material point method with regional time stepping," *Computer Graphics Forum*, vol. 37, no. 8, pp. 195–204, 2018. [Online]. Available: https://onlinelibrary.wiley.com/doi/abs/10.1111/cgf.13524.

[28] M. Ortner and L. G. Coliado Bandeira, "Magpylib: A free python package for magnetic field computation," *SoftwareX*, 2020. DOI: 10.1016/j.softx.2020.100466.

[29] W. Hu, G. Z. Lum, M. Mastrangeli, and M. Sitti, "Small-scale soft-bodied robot with multimodal locomotion," *Nature*, vol. 554, no. 7690, pp. 81–85, 2018.

3.8 Chapter Evaluation

This work represents the first time the MPM has been applied to magnetic soft robots and represents a paradigm shift from previous approaches. Overall, this developed framework has distinct advantages over existing methodologies, particularly when it comes to handling of self-collision and large deformation. When compared to frameworks based on FEM, the MPM avoids issue with mesh-collapse and is also simpler to implement with reference implementations in below 100 lines of code.

The mathematical models of Equation 13, 15 and 19 are my formulations and are based on the fundamental principles established in [1] and [2]. I personally, was responsible for all the implementation, experimental design and fabrication with my co-authors mostly responsible for supervision.

The framework was released with the paper publication and to our knowledge has been used in several publications and is actively being researched in a number of groups. Wang et al. utilised the framework to explore computational design for crawler robots [3], [4]. In their Masters' thesis Norouziani also explored the frameworks use in a computational design process for optimising applied magnetic profile [5].

Despite this implementation being highly parallelised, the time-complexity of the algorithm increases dramatically with stiffer tissues. When compared to simpler, rigid-link based models of the tentacle robots this would lead to a significantly longer optimisation process. The key to improving that is to replace the Semi-implicit Euler method integration methodology with a fully implicit solver. This has been implemented in other MPM methodologies leading to significantly faster algorithms [6].

Our goal with this work was to develop a better framework for modelling of magnetic tentacle robots to allow a computational design framework with more complex dynamic

objectives and allow for arbitrary geometries and magnetisations. However, as with all computational design the dependence on accurate material parameters and fabrication leads to a reality-gap between simulation and real robots. In the case of magnetic soft robots, fabrication of silicones is often dependent on shelf-life and mixing methodology and can lead to large variations in material parameters. With our larger objective of creating a continuum robot which can handle tortuous navigations, the next chapter considers an alternative form of continuum robot where computational design is not necessary to reduce tissue interaction.

References

[1] R. Zhao, Y. Kim, S. A. Chester, P. Sharma, and X. Zhao, "Mechanics of hard-magnetic soft materials," *Journal of the Mechanics and Physics of Solids*, vol. 124, pp. 244–263, 2019.

[2] J. J. Abbott, E. Diller, and A. J. Petruska, "Magnetic methods in robotics," *Annual Review of Control, Robotics, and Autonomous Systems*, vol. 3, no. 1, pp. 57–90, 2020.

[3] L. Wang, "Co-design of magnetic soft robots with large deformation and contacts via material point method and topology optimization," *Computer Methods in Applied Mechanics and Engineering*, vol. 445, p. 118 205, 2025.

[4] S. Wang, Z. Dai, Q. Lu, and C.-Y. Su, "The simulation and path tracking control study of magnetic miniature soft robots," *Journal of Field Robotics*, vol. 42, no. 3, pp. 903–915, 2025.

[5] F. Norouziani, "Design of small scale magnetic soft robots using cma-es and material point method," Ph.D. dissertation, 2025.

[6] Y. Yamaguchi, S. Moriguchi, and K. Terada, "Extended b-spline-based implicit material point method," *International Journal for Numerical Methods in Engineering*, vol. 122, no. 7, pp. 1746–1769, 2021.

Chapter 4

Vine Robots with Magnetic Skin

4.1 Chapter Commentary

This chapter introduces a novel form of miniaturised everting robot named the Magnetic Vine Robot (MVR). After the landmark paper of Hawkes et al, the principle of eversion become an emerging paradigm in soft robotics [1]. This work was originally inspired a between our group at Leeds and Prof. Jee-Hwan Ryu's group at Korea Advanced Institute of Science and Technology (KAIST) [2]. In this collaboration, we first explored the potential use of magnetic steering for vine robots at a large scale (25 mm diameter). Here, we utilised a magnetic element at the tip of the vine robot and used a manipulated EPM for steering. We found this system to be of notably high-performance, with high controllability (i.e. intuitive to navigate the robot via joystick control), large angles of steering and large forward forces from the vine robot. However, this design was relatively large and lost the appealing soft structure of the vine robot.

In this follow-on work we proposed the use of a *magnetic skin* for steering of vine robots. This allowed us to create a robot at just 8 mm scale that can be steered using magnetic fields whilst preserving the soft structure of the robot. We achieved this through the use of a magnetic silicone layer to the robot. This design was our first endeavour into developing

vine robots within our lab and served as a bridge between our previous magnetic tentacle designs and the new vine robot technology.

This work formed a collaboration between our group at Leeds and Tania Morimoto's group at UC San Diego. My contribution was the concept design, manufacturing and experimental setups with the San Diego group contributing the model for robot deformation

The below manuscript is copied from: Davy, J., Greenidge, N.J., Kim, S., Tinsley, L.J., Lloyd, P., Chandler, J.H., Harris, R.A., Morimoto, T.K. and Valdastri, P., 2024. Vine robots with magnetic skin for surgical navigations. IEEE Robotics and Automation Letters, 9(8), pp.6888-6895.

References

[1] E. W. Hawkes, L. H. Blumenschein, J. D. Greer, and A. M. Okamura, "A soft robot that navigates its environment through growth," *Science Robotics*, vol. 2, no. 8, eaan3028, 2017.

[2] N. G. Kim, N. J. Greenidge, J. Davy, *et al.*, "External steering of vine robots via magnetic actuation," *Soft Robotics*, 2024.

4.2 Abstract

Drawing inspiration from natural growth and movement strategies, vine robots possess exceptional passive shape-forming abilities, enabling them to deform around obstacles. However, an intrinsic lack of active steering limits their capacity to control their growth trajectory. This paper considers the external manipulation of such robots through the utilisation of magnetically active materials embedded within the vine robot's skin. This results in a completely flexible, steerable, growing structure that can be actuated via the application of external magnetic fields and field gradients. We explore the principles of magnetically-guided vine robots and provide empirical evidence highlighting the

efficacy of our proposed magnetic steering methodology. Due to the inverted internal structure, careful design of the magnetisation direction of the robot has to be considered. We propose an orthogonal magnetisation strategy that successfully preserves a net positive magnetisation. We focus on a vine robot of 8 mm in diameter, constructed from a polyethylene substrate coated with a silicone layer embedded with magnetic microparticles. We demonstrate the ability of our robots to navigate complex environments and steer around large obstacles in a shear free manner via the simultaneous control of both the magnetic field and the growing pressure. Finally, we demonstrate our robot by performing the selective navigation of multiple bifurcations within a bronchial tree phantom.

4.3 Introduction

Vine robots, also known as soft growing robots, exhibit the ability to conform to their surroundings, enabling seamless adaptations around obstacles and navigation through intricate environments [1], [2]. Vine robots conventionally rely on pneumatic or hydraulic actuation to grow, where pressurisation of an inverted inflatable tube propels the internal material towards the tip to progressively elongate the robot's body [3]. As a result, the robot advances in a shear-free manner, as its compliant soft body conforms to the shape of the surrounding environment. This combination of features offers an innovative solution for traversing convoluted, narrowed, and sensitive anatomical pathways while minimising the potential for traumatic interactions with surrounding tissue [4], [5].

However, without the ability to control orientation and, consequently, growth direction [6], vine robot navigation is limited when operating in open spaces or constrained channels [2], [7]. To enable their use in more complex environments, there is therefore a need for steering mechanisms that preserve the distinct attributes of vine robots, while enabling control over their growth direction.

Previous attempts to to address this challenge have led to the development of various active steering methods, including pneumatic, tendon-driven, and rigid actuation ap-

proaches. The most common steering method involves pneumatic actuators — including serial pneumatic artificial muscles (sPAMs), cylindrical pneumatic artificial muscles (cPAMs), fabric pneumatic artificial muscles (fPAMs), and pouches integrated into the robot wall [3], [6], [8] — that contract along the entire length of the robot. These soft actuators and mechanisms allow vine robots to preserve the advantages of their soft body, however, miniaturisation becomes a challenge due to the added layers and actuators on the robot body. Alternatively, tendon-driven approaches, commonly seen in traditional continuum robots [4], [9], [10] enable bending when the tendon is pulled from the base. These tendons have been routed within the walls of the robot body, as well as within a separate internal channel to enable steering. These designs offer high controllability over curvature but can create a complex internal structure and often require overcoming high friction around the tendons.

Magnetic actuation has emerged as a promising solution for guiding robots within the human body. By controlling an external actuating field in combination with magnetic elements embedded within the robot's body, precise and remote manipulation of these entities becomes possible [11]. To achieve fully soft structures with magnetic actuation, robots can be designed using magnetically hard yet materially soft elastomers [12]. Typically, these materials consist of silicone mixed with NdFeB micro-particles, resulting in a highly deformable structure that responds to external magnetic fields [13]. By eliminating the need for onboard actuators, magnetic robots can be miniaturised down to the millimetre and micrometre scale whilst remaining soft. This has led to the exploration of magnetic robots for endoluminal applications [12], [13].

In this study, we investigate the application of magnetic actuation for steering miniaturised vine robots. Our previous work focused on the design of shape-forming magnetic catheters in order to minimise contact and therefore normal force interaction with the surrounding lumen [13]. In this work, the growing nature of the vine robot eliminates the shear forces generated from contact by avoiding surface translation. These approaches differ at the fundamental level, but both aim at minimising the potential for trauma during endoluminal procedures.

Through the use of magnetically active elastomeric skin, we achieve a fully soft and adaptable vine robot structure, capable of navigating complex environments while minimising shearing interactions with the surroundings. Compared to other steering methods, our design remains fully soft and can achieve high angles of steering with small diameter vine robots. Softness ensures gentle tissue interaction, minimising the risk of trauma. Miniaturisation and deformability enables access to narrow lumens deep within the anatomy, and high manoeuvrability enables precise navigation.

We consider here the fabrication of 8 mm diameter magnetic vine robots (MVRs) with a particular focus on the challenges associated with designing a continuous magnetic body with an inverted internal section. We demonstrate the robot's ability to deform under the influence of external magnetic fields and investigate how this is affected by the internal pressure of the MVR. Our design is steered by controlling an external magnetic field, which can be provided via systems of electromagnetic coils or permanent magnets. In this work, we use the dEPM (dual External Permanent Magnet) platform [14] consisting of two EPMs each mounted to a 7 DoF robotic manipulator in order to apply precise magnetic fields and field gradients in the MVR workspace. We showcase the robot's growth and navigation capabilities within a simple environment, and demonstrate navigation of three different bifurcating pathways within a bronchial tree phantom (See Fig. 5.1), representing a preliminary step toward the potential clinical application of MVRs.

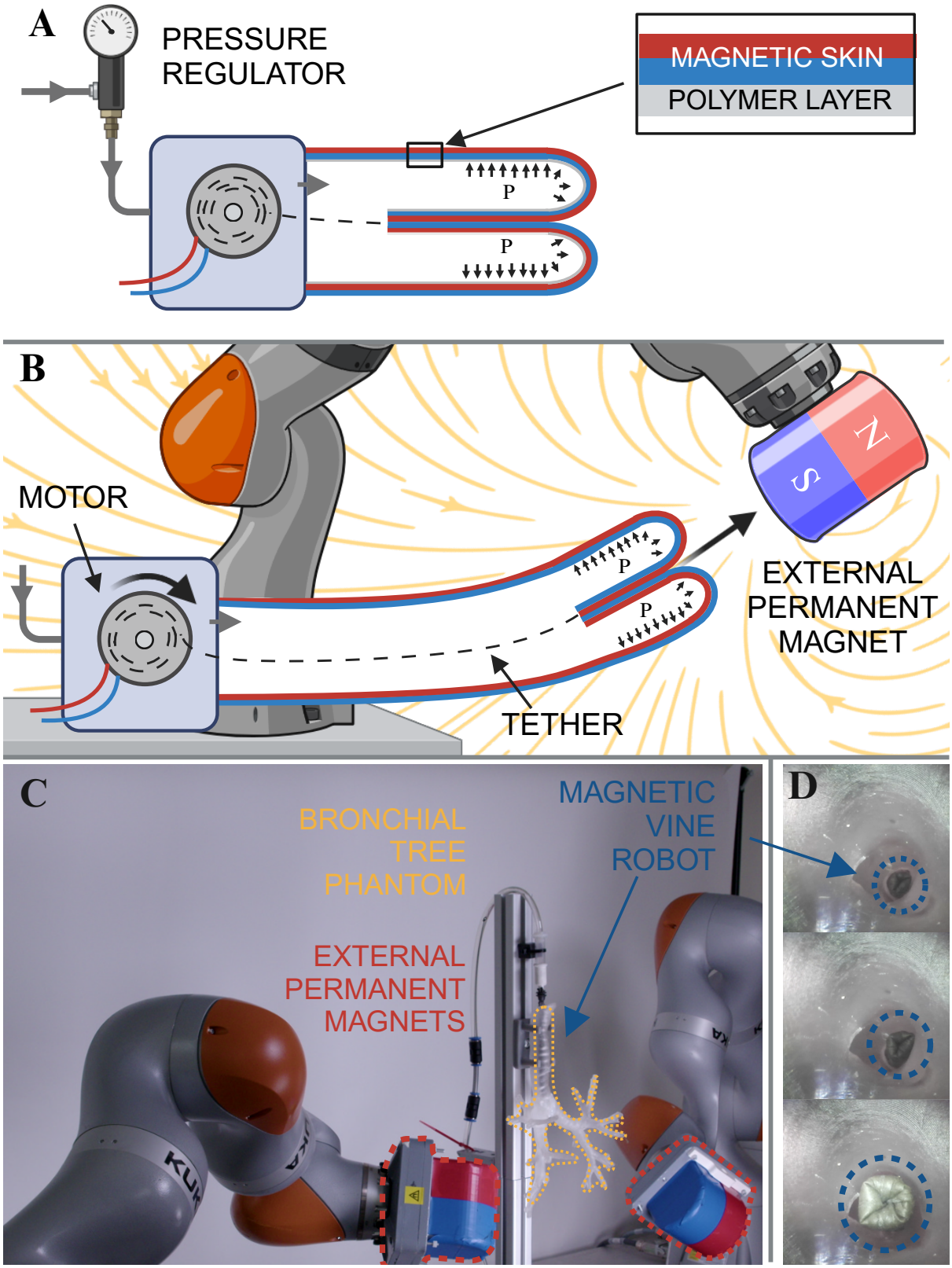

Figure 4.1: (A) Working principle of the proposed Magnetic Vine Robot (MVR) formed from a polymer substrate and magnetic layer. (B) Steering of the MVR is achieved through manipulation of External Permanent Magnets (EPMs). (C) Navigation of a bronchial tree phantom. The EPMs' pose determines the applied field and thus the deflection of the MVR. This permits navigation of the various bifurcations. (D) MVR growing through a lumen.

4.4 Principles

To control the direction of the robot's growth, we propose coating the skin of the robot with a NdFeB doped silicone layer. When an external actuating field is applied, a distributed magnetic wrench is induced, causing deformations throughout the body of the robot. Harnessing this behaviour allows us to control the direction of growth of the MVR.

4.4.1 Everting Vine Robots

The vine robots we consider employ an inverted inflatable cylinder mechanism for their growth. By applying pressure, the internal material is pushed forward, causing it to evert and form the growing body of the robot. A tether attached to the tail of the inverted material constrains the growth of the vine. Without any steering mechanism, the direction of this growth is uncontrolled. With the precise release of the tether, and sufficient internal pressure, the growth of the robot can be precisely controlled.

4.4.2 Direction of Magnetisation

In this study, we focus on an MVR design where the pressurised growing body of the robot is coated with NdFeB doped silicone, a magnetically hard yet materially soft elastomer. "Magnetically hard" refers to the material's high magnetic remanence, i.e. its ability to retain its magnetisation after being magnetised. Most conventional (non-everting) magnetic continuum robots employ axial magnetisation, where the magnetisation direction aligns with the robot's major axis, extending towards the distal end.

Incorporating eversion into magnetic continuum robots introduces an additional consideration when choosing the robot's magnetisation direction, since the inverted material (also called the "tail") has a reversed direction of magnetisation compared to the outer layer (See Fig. 4.2). Under axial magnetisation, the magnetisation direction of the inverted internal region would exactly oppose the one of the outer region, resulting in a net magnetic moment of zero (Fig. 4.2A). By considering a magnetisation orthogonal to the major axis

of the robot, we can generate a net positive magnetic moment, as demonstrated below and in Fig. 4.2B.

Consider a circular cross-section of an MVR possessing some remnant magnetisation. The vector $\hat{\mathbf{m}}$ represents the direction of this magnetisation. For the outer layer of the robot, the total magnetisation of the cross-section can be integrated around φ to yield

$$\mathbf{m}_{\text{outer}} = \frac{1}{2\pi}\int_0^{2\pi} \hat{\mathbf{m}} d\varphi = \hat{\mathbf{m}}. \tag{4.1}$$

For the internal layer, the direction of magnetisation is flipped as the robot body inverts. This results in a rotation of the direction of magnetisation by 2φ (See Fig. 4.2B). Thus, the internal layer exhibits a total magnetisation described by

$$\mathbf{m}_{\text{inner}} = \frac{1}{2\pi}\int_0^{2\pi} R_z(2\varphi)\hat{\mathbf{m}} d\varphi. \tag{4.2}$$

Here, R_z is the rotation matrix representing a rotation of 2φ radians about the z-axis (the major axis) of the MVR. The summation of the outer and inner magnetisations can be used to calculate the total magnetisation.

When considering axial magnetisation, where $\hat{\mathbf{m}} = [0, 0, 1]$, we find that $\mathbf{m}_{\text{outer}} = \hat{\mathbf{m}}$. Substituting and solving (4.2), we obtain $\mathbf{m}_{\text{inner}} = [0, 0, -1]$. Consequently, the overall magnitude of magnetisation $|\mathbf{M}| = |\mathbf{m}_{\text{outer}} + \mathbf{m}_{\text{inner}}| = 0$. However, in the case of orthogonal magnetisation, where $\hat{\mathbf{m}} = [0, 1, 0]$ and $\mathbf{m}_{\text{inner}} = [0, 0, 0]$, a net positive magnetisation is preserved, resulting in $|\mathbf{M}| = [0, 1, 0]$.

4.4.3 Magnetic Actuation

In magnetic actuation, externally applied magnetic fields and field gradients are controlled in order to remotely apply forces and torques on magnetic agents embedded within the robot. For the generation of magnetic fields with sufficient distance, EPMs can be assumed to be magnetic dipoles [15]. The magnetic field produced by a dipole is

$$\mathbf{B}(\mathbf{m}, \mathbf{r}) = \left(\frac{\mu_0}{4\pi \left\| \mathbf{r} \right\|^3} (3\hat{\mathbf{r}}\hat{\mathbf{r}}^T - \mathbb{I}) \right) \mathbf{m}, \tag{4.3}$$

where $\mathbf{r}$ is the displacement vector. $\mathbf{r}$, $\hat{\mathbf{r}} = \frac{\mathbf{r}}{||\mathbf{r}||}$. $\mathbf{m}$ is the magnetic moment of the body. μ_0 is the vacuum permeability $4\pi \times 10^{-7}$ Hm^{-1}.

A magnetic body within a magnetic field $\mathbf{B}$ will experience an aligning torque proportional to the field strength.

$$\boldsymbol{\tau} = \mathbf{m} \times \mathbf{B}. \tag{4.4}$$

Note that, as this is a cross product, the magnetic agent cannot be controlled around its axis of magnetisation, limiting the number of degrees of freedom of magnetic torque to two.

The magnetic field produced by a dipole is inherently inhomogeneous. In these non-homogenous magnetic fields, magnetic agents will experience a force proportional to the spatial gradient of the magnetic field $\nabla \mathbf{B}$.

$$\mathbf{F} = \nabla \mathbf{B}^T \mathbf{m}. \tag{4.5}$$

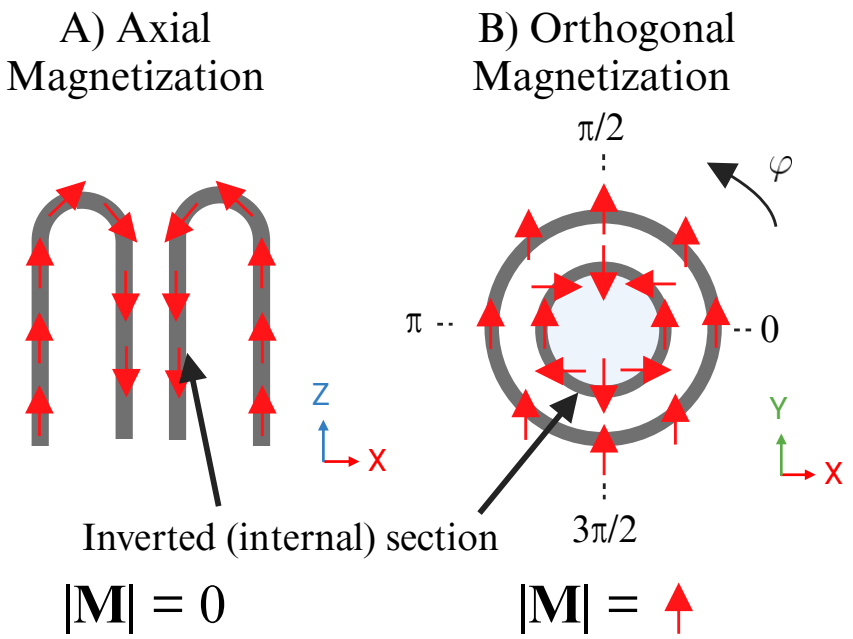

Figure 4.2: Diagram showing two alternative magnetisation strategies for the vine robot, as detailed in Section 4.4.2. (A) The axial magnetisation, when inverted, has a net zero magnetic moment. (B) The orthogonal magnetisation introduced in this work preserves a net non-zero magnetic moment, therefore permitting steering via externally applied fields.

4.5 MVR Modelling

Understanding the bending behaviour of the MVR under an external magnetic field is the key to active magnetic steering. Due to the magnetised skin of the MVR, distributed aligning torques (q_τ [Nm/m]) and magnetic forces (q_F [N/m]) are applied to the MVR, which bend and steer the robot as shown in Fig. 4.3. In this work, a two-stage bending model is developed, where each stage aims to capture the behaviour of the robot at a different level of deflection. In the first stage of the model, when there is only a small amount of deflection, the bending of the inflated cylindrical tube dominates the deflection, as shown in Fig. 4.3B. When a load is applied to the MVR, the base of the MVR wrinkles because the thin-walled tube cannot support compressive stress. As the applied load increases, the wrinkle at the base propagates around the tube, and the tube creases as shown in Fig. 4.3C. This large deflection behaviour is captured in the second stage of the model.

4.5.1 Stage 1: Bending Model

We extend the inflated tube model of Comer et. al. [16] to incorporate distributed magnetic forces and aligning torques for the MVR. Here, we assume that the MVR is radially inextensible and the stiffness of the MVR tail (inverted section) is negligible. Equation (4.6) describes the deflection (y) with respect to the distance along the length (x) for both wrinkled and unwrinkled regions of the MVR.

$$\frac{d^2y}{dx^2} = \begin{cases} \dfrac{M_e(x)}{EI} & \text{unwrinkled region for } x_w < x < l \\ \dfrac{M_e(x)}{EI}\dfrac{2\pi}{2\pi - 2\varphi_0(x) + \sin 2\varphi_0(x)} & \\ & \text{wrinkled region for } 0 < x < x_w \end{cases} \tag{4.6}$$

where EI is the flexural rigidity of the inflated cylindrical tube, and P, R, and l are the internal pressure, the radius, and the length of the MVR, respectively. $\varphi_0(x)$ is the angle of the wrinkles around the tube at distance x, as shown in the inset of Fig. 4.3B. The wrinkled and unwrinkled regions are divided at $x = x_w$, and $M_e(x_w) = \pi R^3 P/2$ is satisfied [16]. M_e is the externally applied moment, which is given as

$$M_e(x) = \int_x^l q_f(u)(l-u) + q_\tau(u) - q_g(u)du, \tag{4.7}$$

where q_g is the distributed moment due to gravity and u is a dummy variable for the integral. For the wrinkled region, the relationship between M_e and φ_0, as provided in [16], must also be considered:

$$\frac{M_e(x)}{PR^3} = \frac{\pi[2\pi - 2\varphi_0(x) + \sin 2\varphi_0(x)]}{4[\sin\varphi_0(x) + [\pi - \varphi_0(x)]\cos\varphi_0(x)]}. \tag{4.8}$$

To solve for y in the unwrinkled region ($x_w < x < l$), (4.6) is differentiated with respect to x, resulting in

$$\frac{d^3y}{dx^3} = -\frac{q_f(l-x) + q_\tau - q_g}{EI}. \tag{4.9}$$

For the wrinkled region ($0 < x < x_w$), (4.8) is substituted into (4.6), and (4.8) is differentiated with respect to x to solve for y and φ_0.

$$\begin{aligned}
\frac{d^2y}{dx^2} =& \frac{\pi^2 R^3 P}{2EI[\sin\varphi_0 + (\pi - \varphi_0)\cos\varphi_0]} \\
\frac{d\varphi_0}{dx} =& -\frac{4[q_f(l-x) + q_\tau - q_g]}{\pi R^3 P} C \\
C =& \left[\frac{-2 + 2\cos 2\varphi_0}{\sin\varphi_0 + (\pi - \varphi_0)\cos\varphi_0} + \right. \\
& \left. \frac{(2\pi - 2\varphi_0 + \sin 2\varphi_0)(\pi - \varphi_0)\sin\varphi_0}{[\sin\varphi_0 + (\pi - \varphi_0)\cos\varphi_0]^2}\right]^{-1}
\end{aligned} \tag{4.10}$$

Equation (4.9) and (4.10) then can be numerically solved together for y and φ_0 with the following boundary conditions, where the prime notation ($'$) represents the derivative

with respect to x.

$$\begin{aligned} y(0) &= 0 \\ y'(0) &= 0 \\ y(x_w^-) &= y(x_w^+) \\ y'(x_w^-) &= y'(x_w^+) \\ M_e(x_w^-) &= M_e(x_w^+) \end{aligned} \tag{4.11}$$

Once y is found, a bending angle (θ) is calculated using $\theta = \sin^{-1}[y(l)/l]$.

4.5.2 Stage 2: Creasing Model

When the externally applied moment at the base ($M_e(0)$) becomes greater than $\pi R^3 P$, the wrinkles at the base propagate entirely around the MVR ($\varphi_0(0) = \pi$), causing the MVR to buckle and undergo a large deflection. We note that in some cases, prior to reaching $\varphi_0(0) = \pi$, if the first stage model cannot find a viable solution, a large deflection of MVR is assumed. To model this behavior, the second-stage model is studied, where we assume a crease is formed at the base of the MVR due to buckling (Fig. 4.3C). The rest of the MVR is assumed to remain straight for simplicity. At static equilibrium, the externally applied moment at the base ($M_e(0)$) is the same as the resisting moment generated by the crease (M_c).

$$M_e(0) = M_c \qquad \text{for } M_e > \pi R^3 P \tag{4.12}$$

M_c can be analytically modeled as provided in [17], [18] by assuming that the internal pressure (P) does not change due to the variation in internal volume (V) as the crease forms.

$$M_c = P\frac{dV}{d\theta} = \pi R^3 P \left(\tan^2 \frac{\theta}{2} + 1\right) \tag{4.13}$$

By solving (4.7), (4.12), and (4.13), θ as a function of P for a given design and magnet position can be found.

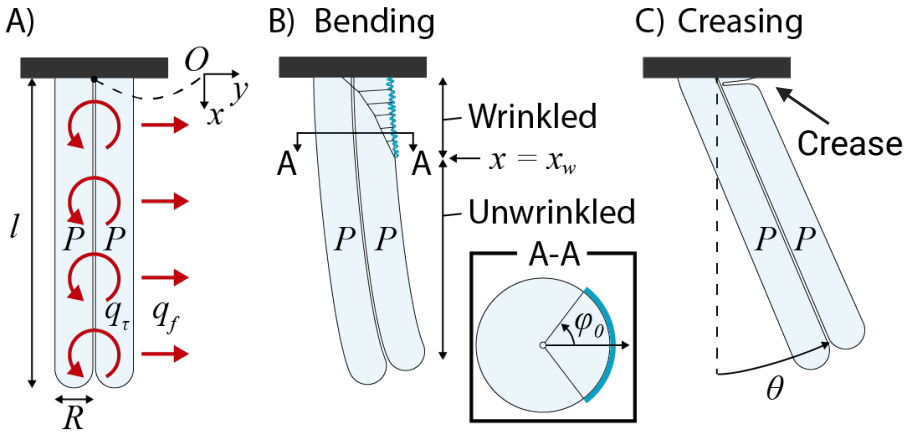

Figure 4.3: Schematics of the vine robot bending. (A) Under an external magnetic field, distributed magnetic forces and aligning torques are applied to the vine robot. The gravity is in the x direction, and the internal pressure of the vine robot is P. (B) The first-stage model where a small deflection is dominated by bending. (C) The second-stage model where a large deflection is dominated by a crease at the base.

4.6 MVR Design and Fabrication

4.6.1 Magnetic Coating

The MVR is constructed from a 20 μm thick Low-Density Polyethylene (LDPE) sheet coated with a layer of silicone mixed with NdFeB magnetic particles. The LDPE sheet is folded and heat-sealed using a impulse sealer to create a cylindrical structure with an external diameter of 8 mm and a length of 250 mm. The structure is inverted to leave the created seal on the inside of the body. This LDPE cylinder is then mounted vertically on an acrylic tube. We prepare a two-part silicone polymer (Ecoflex 0030, Smooth-on) and add 5 μm NdFeB micro-particles (MQFP-Bb, Magnequench GmnH) to achieve a 50-50 mass ratio of silicone and particles. This mixture undergoes vacuum mixing for 200 seconds at 1600 RPM. Subsequently, the magnetic silicone mixture is applied to the LDPE cylinder using a brush, with efforts to maintain a uniform single layer. The silicone-coated cylinder is then left to cure (Fig. 4.4) for four hours. Across five fabricated robots, the average mass of the completed MVRs measures 1.8 g (σ = 0.37 g). Over all MVRs, the average thickness of the silicone layer is 198.75 μm (σ = 138 μm).

To impart the direction of remnant magnetisation of the coating, the MVR is removed from the acrylic cylinder and wrapped around a wooden dowel. This is placed within the coil of an impulse magnetizer (ASC176 IM-10-30, ASC Scientific, USA), where a field of 1.5 T is applied. After unwrapping from the dowel, the MVR exhibits orthogonal magnetization along its entire length.

4.6.2 Tether Control and Pressurisation

Similar to previous work, the growth of the MVR is managed through a combination of a tether release motor and pressurisation [1], [2]. Air pressure is introduced through a controlled compressed air supply into the proximal end of the robot. The tether serves as a constraint, allowing precise control of the robot's length by releasing the tether via a motor, itself situated within the pressurised enclosure.

Figure 4.4: Fabrication of the MVR. An LDPE substrate layer (A) is formed into a cylinder (B) then coated in NdFeB doped silicone (C). After curing, the robot is inverted and (D) attached to a tether.

4.6.3 Magnetic Manipulation Platform

For actuation purposes, we employ the dEPM platform from [19]. This platform comprises two 7 Degrees of Freedom (DoF) robot manipulators (KUKA IIWA LBR14), each equipped with 100 mm diameter and 100 mm length EPMs (N52 NdFeB). By manipulating the pose of the EPMs, we can control the applied magnetic field on the MVR.

The use of two EPMs offers advantages such as full-rank magnetic actuation and higher applied fields. However, in our experimentation, we do not utilise both EPMs simultaneously. Instead, this platform provides a convenient means of fully manipulating the EPMs around the workspace of the MVR, which would be challenging with a single manipulator [19].

4.7 Results

4.7.1 Free-space Deflection

We first consider the free-space deflection of the MVR against gravity. The MVR of 80 mm was placed between the dual EPM platform on a mounting stand. A single EPM was placed at a horizontal distance d from the center of the workspace. The value h refers to the vertical offset between EPM and MVR (h = 65 mm, l = 80 mm). This was chosen to approximately focus the center of the magnetic field at the center of the MVR at rest (see Fig. 4.5).

To investigate the deflection of the MVR in two different planes, we consider two actuation cases, torque-dominated and gradient-dominated. This is due to the fact that magnetic torque cannot be applied around the axis of magnetisation. In the torque-dominated case (Fig. 4.5B), we rely primarily on the use of magnetic torque. In this case, the EPM is oriented so that its magnetisation axis is orthogonal to that of the MVR in order to produce a misalignment and therefore a magnetic torque on the MVR. In the gradient-dominated case (Fig. 4.5C), we rely primarily on the use of the magnetic field gradient. A magnetic force is applied on the MVR by orienting the EPM so that its magnetisation axis is in alignment with that of the MVR. In both cases, there is mixed contribution to the overall deflection of the MVR but the named effect is considered the primary contributor. In both cases, the magnitude of the effect is dependent on the separation distance between the EPM and the MVR.

To investigate both cases, the bending angle of an MVR without the internal inverted material was observed over a range of EPM distances and pressures and compared to the model results (Fig. 4.6). The growing pressure of these MVRs was experimentally found to be 12 kPa, and therefore in this work we consider a range of vine pressures up to 12 kPa. The results show that the model is able to capture the major aspects of the MVR's deflection behavior. In particular, we quantified the model errors by taking the difference between the model-predicted values and the experimentally measured values.

The experimental data points used for the error calculation are indicated with solid markers in Fig. 4.6, and were selected to be the points at which the bending behavior of the MVR transitioned from a small deflection to a large deflection. In the torque-dominated case, the model was able to predict when the MVR started to crease with errors of 77, 21, and 12 mm at 1, 6, and 12 kPa. The differences between the predicted maximum bending angles and the experimental measurements were 4.7, 9.1, and 1.2^o at 1, 6, and 12 kPa, respectively. Similarly for the gradient-dominated case, the EPM distances where the MVR started to crease were predicted with errors of 36, 1, and 18 mm at 1, 6, and 12 kPa. The maximum bending angles were modeled with errors of 8.2, 9.6, and 3.5^o at 1, 6, and 12 kPa, respectively. As observed, model performance is greater at the higher pressures, since the model assumes an inflated beam as the robot body. Further improvement in the model could be achieved by considering the stiffness of the MVR body and more accurate magnetic field modeling when in close proximity to the EPM.

In addition, the effect of robot length (l) on bending angle was investigated, while d and h were kept at 127 mm and 69 mm, respectively. Fig. 4.7 shows the resulting bending angle as the robot grows towards the static EPM. It can be observed that there is a critical length at which the MVR buckles and deflects towards the EPM, which is reasonably captured by the model.

Finally, Fig. 4.8 shows the deflection of the MVR in the torque case with the inclusion of the internal inverted material and tensioned tether at specified intervals. It can be observed that as the EPM is brought closer and then removed, the MVR fails to return to it's original rest pose. This effect is not captured in our model and is related to bias in the internal tensioned tether material. Despite this, the MVR remains controllable and any further movement by the EPM in the range of actuation still is capable of deforming the vine.

The required EPM distance is proportional to the magnetic volume, both of the MVR and EPM. Given the constraints imposed by the human anatomy, we estimate required

actuation distances will be in the range of 100-300 mm for navigation in the bronchial tree [13]. Our observed actuation distances fall within the lower end of this range but could be compensated for with MVR designs with higher magnetic volume or alternatively, larger EPMs.

4.7.2 Navigation of Constricted Channel

A key feature of vine robots is the ability to squeeze through gaps smaller than their diameter. Vine steering methodologies based on hard internal components fail to retain this feature. Our presented MVR design is formed of an entirely soft body and therefore is capable of contracting its diameter in order to pass through constricted channels. To demonstrate this capability, we grow the MVR through gaps smaller than its nominal diameter. Figure 4.9 shows the MVR squeezing through gaps of 5 and 3 mm, respectively, at a growing pressure of 12 kPa. As demonstrated, the MVR is capable of passing through these gaps and continuing to grow. In the 3 mm case, this demonstrates the MVR's capability to successfully pass through gaps 37.5% of its diameter. In these experiments, the MVR was not capable of passing through a 2 mm gap. This lower limit of navigation through a constricted channel can likely be attributed to high internal friction that cannot be overcome without surpassing the maximum growing pressure that can be applied without a risk of bursting the MVR.

4.7.3 Navigation

With large deflections dominant at lower pressures, we devise a control strategy for navigating with the MVR based on regulation of pressure and control of the EPM pose. For growth of the MVR, we increase the pressure of the MVR to 12.0 kPa and the tether is released by the desired growing length. Then, when large deformations are required the pressure is lowered in order to facilitate steering.

To demonstrate this control strategy, we navigate the MVR around two obstacles to form a sigmoidal (S-shaped) path (see Fig. 4.10). The MVR is oriented such that the

axis of magnetization is perpendicular to the plane of deformation and the gradient-dominated strategy (as detailed in Section 4.7.1) is exploited. In Fig. 4.10C the MVR pressure is 12.0 kPa. At t = 57 s (Fig. 4.10D), the pressure is reduced to 0 kPa. It can be observed that at this reduced pressure, the robot bends around the obstacle, facilitating navigation. The total time to navigate the two obstacles averaged 144 s over two repetitions, with the majority of this time taken up by manual pressure regulation and EPM introduction/retraction (See Supplementary Video).

4.7.4 Bronchial Tree Phantom Demonstration

With this developed control strategy, we perform a final demonstration of the MVR in a bronchial tree phantom. The bronchi phantom is created from anatomical CT data and 3D printed using a hard translucent resin (see Fig. 4.11) [13]. We perform three navigations through the bifurcations of the bronchial tree targeting three areas of interest in order to demonstrate the use of magnetic control. These channels all have a diameter larger then the MVR. Through EPM positioning and pressure regulation, we successfully navigate to the three target locations (A, B and C) in 35, 28 and 61 seconds respectively (see Fig. 4.11). The lack of shearing action between the vine robot and phantom walls facilitates this deep navigation (See Supplementary Video).

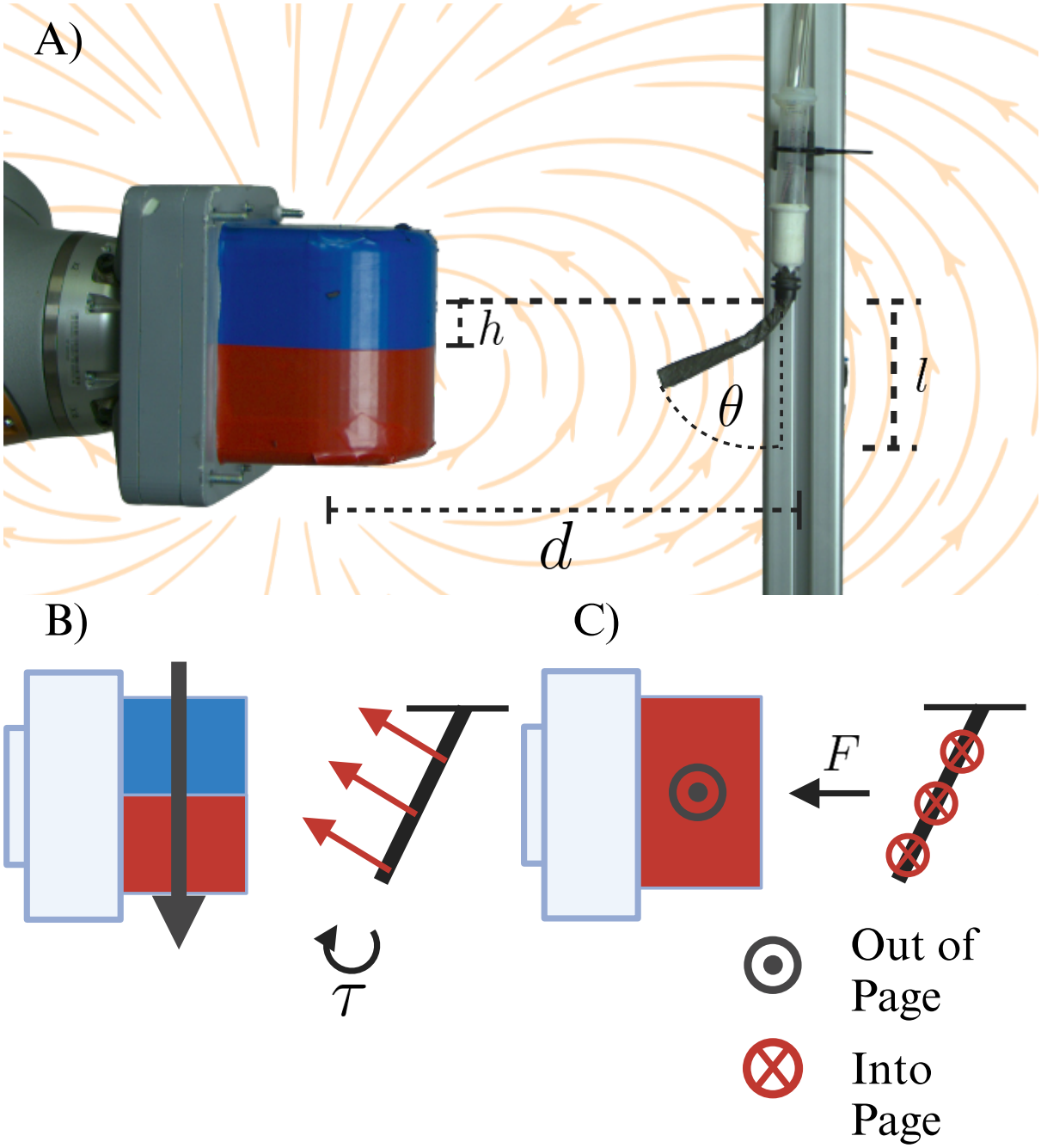

Figure 4.5: Setup for free-space deflection tests. (A) Two actuation modes are utilised depending on the orientation of the robot. This is required due to the orthogonal magnetisation. The first case (B) considers the deflection with the axis of magnetisation lying on the plane of actuation (torque-dominated actuation). The second case (C) considers orthogonality between the axis of magnetisation and plane of actuation (force-dominated actuation)

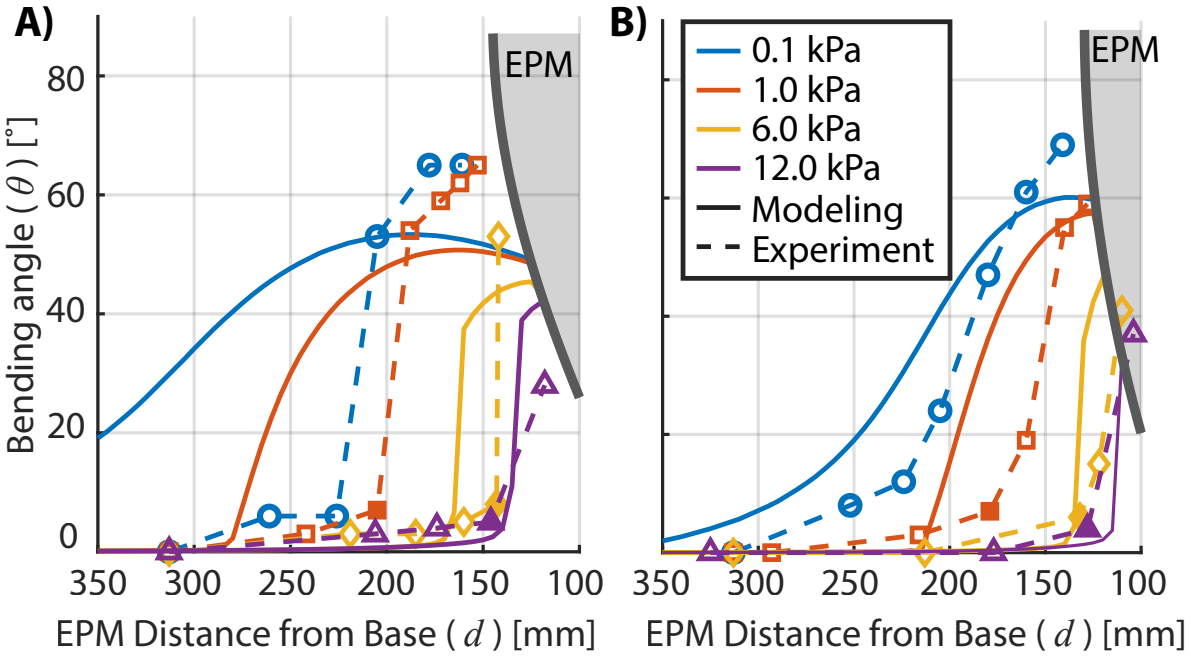

Figure 4.6: Graphs showing the deflection of the MVR in free space in the two scenarios described in Section 4.7.1 and Fig. 4.5. (A) torque-based actuation and (B) gradient-based actuation. Deflections are shown at four different operating pressures. The gray area represents the EPM.

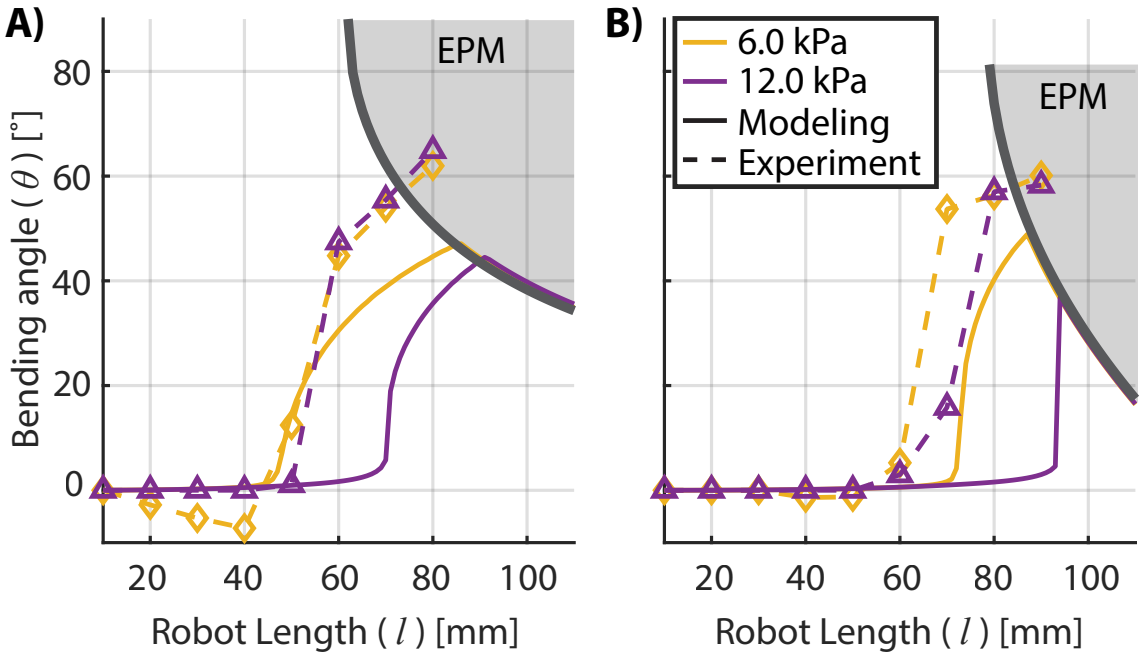

Figure 4.7: Graphs showing the deflection versus deployed length in free space in the two scenarios described in Section 4.7.1 and Fig. 4.5. (A) torque-based actuation and (B) force-based actuation. The gray area represents the EPM.

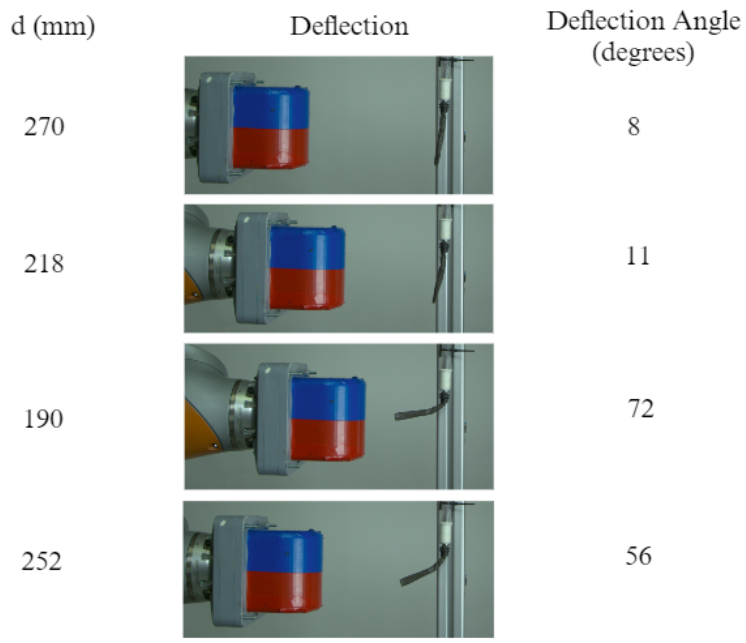

Figure 4.8: Deformation of the MVR with movement of the EPM in the torque case (h = 65 mm). Note how due to the tensioned internal tether the MVR does not return to its original rest pose upon EPM retraction.

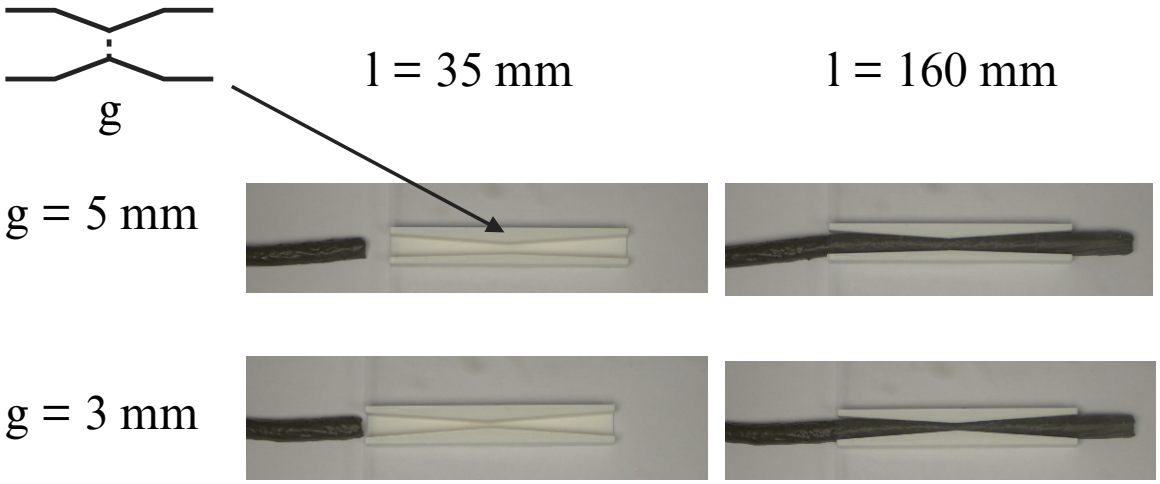

Figure 4.9: Demonstration of the MVRs ability to squeeze through small gaps down to 37.5% of original diameter. The fully soft nature of the MVR design enables the retention of this key feature of vine robots.

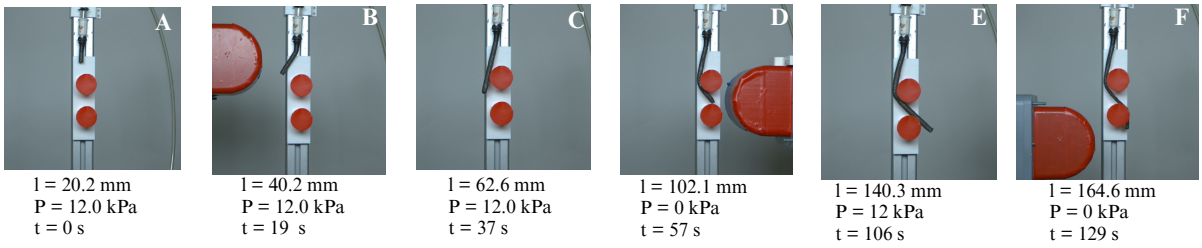

Figure 4.10: Navigation around two obstacles to form an 'S' shape with the robot body. The regulation of pressure within the robot allows for large deflections to be achieved despite relatively low magnetic moment.

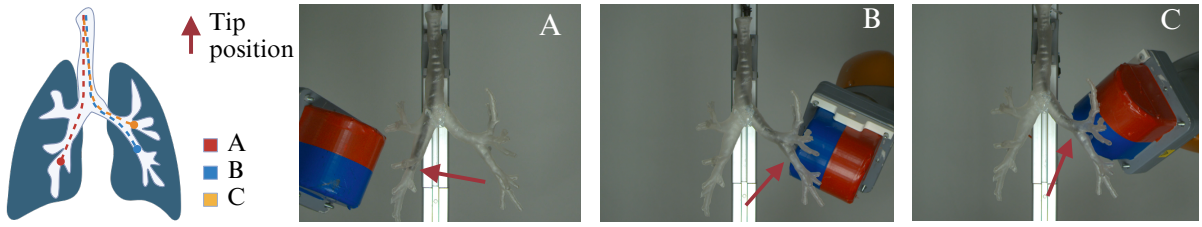

Figure 4.11: Navigation of bronchial tree to three different peripheral locations. The pose of the EPMs steers the vine robot through the desired pathway. Regulation of pressure allows greater deformations of the robot, enabling steering through the bifurcations, since at high pressure the pneumatic restoration force dominates.

4.8 Conclusion

In this work, we have presented a miniaturised design for a magnetically steerable vine robot. The inverted internal section of the MVR opposes the direction of the outer body. In order to preserve a net positive magnetic moment we have proposed an orthogonal magnetisation strategy to preserve the ability to steer everting MVRs. We have investigated how deflection of the MVR is affected by the relative pose of the EPM and by the pressure within the MVR. The relatively high pressure required to grow the MVR is too high to achieve the large deflections in some cases. Therefore we proposed a strategy for control of the MVR based on regulating pressure when steering is required.

Compared to other magnetic continuum robots, the magnetic moment of the MVR is relatively low. This means the EPMs must be positioned close to the MVR in order to achieve large deflections. These distances are below what would be clinically viable. Future work should consider how the magnetic moment of the robot could be increased to enable MVR steering in a larger workspace. This will involve exploring the relationship between magnetic moment and flexibility as a function of layer thickness and composition. These parameters profoundly affect the ability of the robot to effectively evert, grow, and steer.

In order to reach the deformations required for navigation in the demonstrations in this work, the MVR pressure had to be reduced in some cases to zero. Because our model assumes an inflated beam with non-zero pressure, the model showed larger discrepancies with the experiments at low pressures. Future work should consider how non-inflated beams can be accurately modeled. The retraction of the MVR remains an open problem. Successful retraction relies on a strong grounding force at the vine tip [20]. Future work will consider if magnetic forces can be used to apply this stabilisation to allow for successful retraction.

During experimentation, it was observed that with multiple inversions and eversions of the MVR, the NdFeB doped silicone layer began to peel from the LDPE substrate. This

limited the MVR's lifecycle to roughly 10 repetitions. Future work should consider how the bonding between the magnetic coating and polymer layer can be improved in order to develop a more robust MVR. Furthermore, the application of the magnetic silicone with a brush is inherently inconsistent. Future work should consider other, digitally controlled coating methods that can provide a more consistent layer thickness, which will also help to improve the model predictions. This development, in turn, will open up the exciting potential for open and eventually closed loop control strategies. The NdFeB particles utilised are not bio-compatible. Future work should consider how a biocompatible skin can be formed, either through additional protective layers or alternative types of magnetic particles.

When compared to other steerable vine robots, we note that there have been designs demonstrated down to the 2.9 mm diameter [4]. However, such designs are based on internal hard steering mechanisms, which can have limitations in squeezing through gaps much smaller than their body diameter. Compared to other "fully-soft" (i.e. no internal rigid components) steerable vine robot designs that have a range of diameters from 20 to 38 mm [1], [21], the presented MVR is over 50% smaller. Based on our proposed model, it can be observed that the potential for further miniaturisation will be dependent on the required magnetic volume, external magnetic field strength, and the required growing pressure.

Future work should also consider how not just the tip, but the entire shape of the MVR can be controlled. This has the potential to further decrease undesired interactions with the surrounding anatomy. Finally, functionalisation of the robot should be considered based on the particular clinical application, likely taking advantage of the internal channel the MVR creates once grown.

References

[1] E. W. Hawkes, L. H. Blumenschein, J. D. Greer, and A. M. Okamura, "A soft robot that navigates its environment through growth," *Science Robotics*, vol. 2, no. 8, eaan3028, 2017.

[2] N. G. Kim and J.-H. Ryu, "A soft growing robot using hyperelastic material," *Advanced Intelligent Systems*, vol. 5, no. 2, p. 2 200 264, 2023.

[3] L. H. Blumenschein, M. M. Coad, D. A. Haggerty, A. M. Okamura, and E. W. Hawkes, "Design, modeling, control, and application of everting vine robots," *Frontiers in Robotics and AI*, vol. 7, p. 548 266, 2020.

[4] P. Berthet-Rayne, S. H. Sadati, G. Petrou, *et al.*, "Mammobot: A miniature steerable soft growing robot for early breast cancer detection," *IEEE Robotics and Automation Letters*, vol. 6, no. 3, pp. 5056–5063, 2021.

[5] M. Li, R. Obregon, J. J. Heit, A. Norbash, E. W. Hawkes, and T. K. Morimoto, "Vine catheter for endovascular surgery," *IEEE Transactions on Medical Robotics and Bionics*, vol. 3, no. 2, pp. 384–391, 2021.

[6] J. D. Greer, T. K. Morimoto, A. M. Okamura, and E. W. Hawkes, "A soft, steerable continuum robot that grows via tip extension," *Soft robotics*, vol. 6, no. 1, pp. 95–108, 2019.

[7] P. A. Der Maur, B. Djambazi, Y. Haberthür, *et al.*, "Roboa: Construction and evaluation of a steerable vine robot for search and rescue applications," in *2021 IEEE 4th International Conference on Soft Robotics (RoboSoft)*, IEEE, 2021, pp. 15–20.

[8] T. Abrar, F. Putzu, A. Ataka, H. Godaba, and K. Althoefer, "Highly manoeuvrable eversion robot based on fusion of function with structure," in *2021 IEEE International Conference on Robotics and Automation (ICRA)*, IEEE, 2021, pp. 12 089–12 096.

[9] S. Wang, R. Zhang, D. A. Haggerty, N. D. Naclerio, and E. W. Hawkes, "A dexterous tip-extending robot with variable-length shape-locking," in *2020 IEEE Inter-*

national Conference on Robotics and Automation (ICRA), IEEE, 2020, pp. 9035–9041.

[10] N. D. Naclerio, A. Karsai, M. Murray-Cooper, *et al.*, "Controlling subterranean forces enables a fast, steerable, burrowing soft robot," *Science Robotics*, vol. 6, no. 55, eabe2922, 2021.

[11] Z. Yang and L. Zhang, "Magnetic actuation systems for miniature robots: A review," *Advanced Intelligent Systems*, vol. 2, no. 9, p. 2 000 082, 2020.

[12] Y. Kim and X. Zhao, "Magnetic soft materials and robots," *Chemical reviews*, vol. 122, no. 5, pp. 5317–5364, 2022.

[13] G. Pittiglio, J. H. Chandler, T. da Veiga, *et al.*, "Personalized magnetic tentacles for targeted photothermal cancer therapy in peripheral lungs," *Communications Engineering*, vol. 2, no. 1, p. 50, 2023.

[14] G. Pittiglio, J. H. Chandler, M. Richter, V. K. Venkiteswaran, S. Misra, and P. Valdastri, "Dual-arm control for enhanced magnetic manipulation," in *2020 IEEE/RSJ International Conference on Intelligent Robots and Systems (IROS)*, IEEE, 2020, pp. 7211–7218.

[15] A. J. Petruska and J. J. Abbott, "Optimal permanent-magnet geometries for dipole field approximation," *IEEE transactions on magnetics*, vol. 49, no. 2, pp. 811–819, 2012.

[16] R. Comer and S. Levy, "Deflections of an inflated circular-cylindrical cantilever beam," *AIAA journal*, vol. 1, no. 7, pp. 1652–1655, 1963.

[17] C. R. Nesler, T. A. Swift, and E. J. Rouse, "Initial design and experimental evaluation of a pneumatic interference actuator," *Soft robotics*, vol. 5, no. 2, pp. 138–148, 2018.

[18] R. Jitosho, S. Simón-Trench, A. M. Okamura, and B. H. Do, "Passive shape locking for multi-bend growing inflated beam robots," in *2023 IEEE International Conference on Soft Robotics (RoboSoft)*, IEEE, 2023, pp. 1–6.

[19] G. Pittiglio, M. Brockdorff, T. da Veiga, J. Davy, J. H. Chandler, and P. Valdastri, "Collaborative magnetic manipulation via two robotically actuated permanent magnets," *IEEE Transactions on Robotics*, vol. 39, no. 2, pp. 1407–1418, 2022.

[20] N. G. Kim, D. Seo, S. Park, and J.-H. Ryu, "Self-retractable soft growing robots for reliable and fast retraction while preserving their inherent advantages," *IEEE Robotics and Automation Letters*, 2023.

[21] C. Watson, R. Obregon, and T. K. Morimoto, "Closed-loop position control for growing robots via online jacobian corrections," *IEEE Robotics and Automation Letters*, vol. 6, no. 4, pp. 6820–6827, 2021.

4.9 Chapter Evaluation

The developed Magnetic Vine methodology fundamentally explores a different approach to reducing tissue interaction to the tentacle robots. Whereas the shape-forming ability of the tentacle robot negates normal forces with the surrounding tissue, it still has shearing interaction particularly when the vessel is in close proximity with the surrounding tissue. However the vine robot, due to its everting nature eliminates shear interaction but accepts normal forces. We also eliminate forces associated with pushing of the robot from the proximal end and instead our locomotion force is grounded at the robot tip. This has the potential to reduce buckling and allows for navigation through constricted vessels or openings.

This approach represents an entirely novel form of magnetic continuum robot. By incorporating everting technology the robot is capable of self-propelling with minimal tissue interaction. We also present the first analysis of these novel robots and discuss how they challenge the conventional forms of magnetic robots.

The magnetic skin approach however, limits the miniaturisation of the robot. As explored in other work, the thickness of the vine robot walls is proportional to growing pressure [1]. However, reducing the thickness of the applied magnetic skin reduces the overall magnetic volume and therefore steerability. This leads to the problem that the robot

cannot be steered and grown simultaneously significantly reducing the ease of navigation. It also requires high-magnetic fields to achieve this above which is realistically achievable at typical required actuation distances in the clinic [2], [3]).This trade-off is inherent to the design of magnetic-skin vine robots and therefore implored us to consider ways of increasing the magnetic volume of the vine robot.

References

[1] C. Girerd, A. Alvarez, E. W. Hawkes, and T. K. Morimoto, "Material scrunching enables working channels in miniaturized vine-inspired robots," *IEEE Transactions on Robotics*, 2024.

[2] B. J. Nelson, "An electromagnetic robot for navigating medical devices," *Nature Reviews Bioengineering*, vol. 2, no. 5, pp. 370–371, 2024.

[3] G. Pittiglio, J. H. Chandler, M. Richter, V. K. Venkiteswaran, S. Misra, and P. Valdastri, "Dual-arm control for enhanced magnetic manipulation," in *2020 IEEE/RSJ International Conference on Intelligent Robots and Systems (IROS)*, IEEE, 2020, pp. 7211–7218.

Chapter 5

Magnetic Fluid-Driven Vine Robots for Minimally Invasive Tissue Biopsy Sampling

5.1 Chapter Commentary

The magnetic skin approached discussed in the last chapter is fundamentally limited in magnetic volume as the magnetic material itself is constrained by the wall thickness of the material. To overcome this, whilst preserving the appealing soft compliant structure of the robot, we fill the internal space with a magnetic fluid. This new approach instead of relying on the surface of the vine robot for placing this material, instead utilises the much larger internal volume of the vine. This fluid, formed of a iron-water suspension, enables the crucial property of being able to steer and grow the vine simultaneously enabling particularly tortous navigations. Through pressurisation, and release of the vine tail, the fluid grows the vine providing forward locomotion and via application of external magnetic fields, forces can be applied to the vine robot enabling steering through bifurcations.

Further, this work exploits another behaviour of vine robots, namely their ability to

passively stabilise on their surroundings. This is achieved due to the vine robots contact with the anatomy and inflated soft body. This acts similarly to a ballooning catheter stabilising and providing a grounding force. We utilise this to apply large tip forces enabling the use of a biopsy needle for penetration of soft tissue.

The below manuscript is sourced from: Davy, J., Dean, T.P., Greenidge, N.J., Calmé, B., Lloyd, P., Chandler, J.H. and Valdastri, P., 2025. Magnetic Fluid-Driven Vine Robots for Minimally Invasive Tissue Biopsy Sampling. Advanced Intelligent Systems, p.2400827.

5.2 Abstract

There is a growing need for precise, minimally invasive biopsy techniques that reduce patient discomfort, improve sampling accuracy in hard-to-reach areas, and minimise tissue damage. Vine robots, a type of continuum robot, offer a promising solution with their unique ability to evert, allowing them to navigate complex environments while reducing friction. This paper presents a novel vine robot design powered by magnetic fluid. The fluid drives both vine growth through pressurisation and enables precise steering and manipulation using external magnetic fields. Unlike previous designs, our robot's high magnetic volume ensures precise control even under pressure, while maintaining a fully soft structure. This allows for controlled needle movements during biopsies. Additionally, the robot achieves passive stabilisation by pressing against surrounding walls. This stabilisation, combined with magnetic forces can exert up to 1.26 N of insertion force at the tip, enabling effective tissue penetration. We conducted experiments with a 5 mm diameter, 145 mm long magnetic fluid-driven vine robot, demonstrating movement in free space, through narrow constrictions, and within phantoms modeled after human bronchial anatomy. These results pave the way for the robot's potential application in minimally invasive surgeries, particularly in difficult-to-access areas of the body.

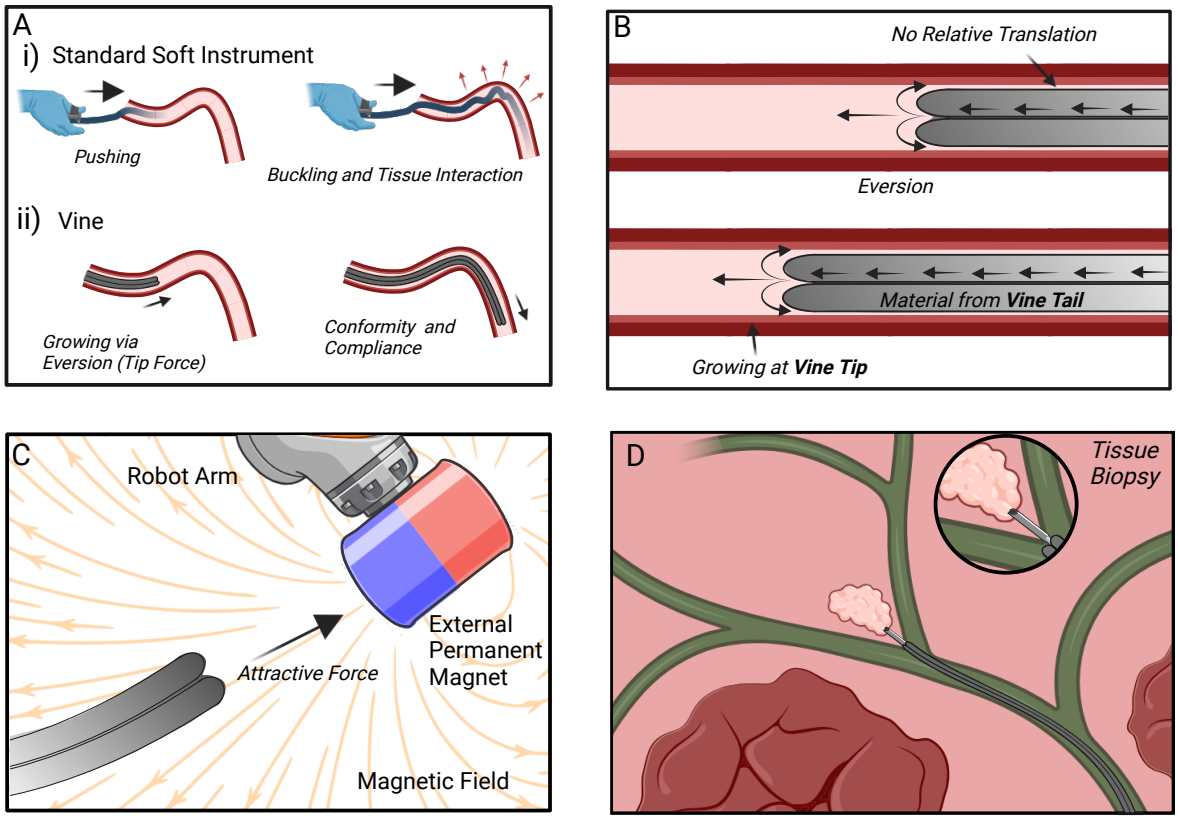

Figure 5.1: A) A traditional soft catheter is prone to buckling and creates high forces on the surrounding vessels. A vine robot concentrates its force at the tip and moves in a shear-free manner. B) Vines locomote via everting, the inner tail moves forward due to pressure and everts at the tip. The everted material remains static as the vine extends its length. C) Magnetic fluid driven vines can be steered using external permanent magnets (EPMs) to induce forces on the body. D) Magnetic fluid driven vines can be highly miniaturised and enable navigation deep within the anatomy.

5.3 Introduction

Any decision to perform an endoscopic or catheter enabled intervention must be weighed against the risk of procedural complications [1]. Standard endoscopic instruments are formed of hard bodies (relative to the anatomy through which they will travel) and thus carry the potential for traumatic tissue interaction. These instruments are typically controlled by internal tendons allowing limited bending focused purely at the tip and their insertion through the anatomy can be limited by frictional forces with surrounding tissues [2]. Such tools are often characterised by low dexterity, limited control and large diameter [3]. These challenges motivate the design of new robotic instruments [3], [4] one of which is the everting catheter [5]–[7]. These devices utilise an unraveling material which, instead of translating through a lumen, locomote via tip centered growth. This form of locomotion minimises potentially traumatic tissue interaction and focuses the forces of insertion at the distal rather than proximal end of the device [6]. Recently, such robots integrated with robotic steering methods such as pneumatic artificial muscles, have been designated as “soft growing robots" or “vine robots" (so named due to their visual and behavioral similarity to the climbing plant) and have been explored for a wide range of applications including military, civil engineering and medical [8], [9].

In the medical domain, these vine robots form part of a wider group of soft robotic systems where it is hoped that softer materials can minimise stress on surrounding tissue during physical interaction [10]. For target applications in navigation of tight lumens, a longstanding goal has been the miniaturisation of such devices. With decreased vine diameter comes a reduced tip cross sectional area and therefore the internal pressure required to evert the material increases [11]. Further, as with any robotic system, miniaturisation creates challenges due to the difficulty of small-scale manufacturing and the inevitable reduction in usable actuating force.

Non-steered everting catheters have long existed, with some approved for clinical use [5]. Given their soft conforming bodies, they are capable of passively adapting to anatomical paths requiring no active steering mechanism [12]. A more recent example would

be VINE (Vascular Internal Navigation by Extension), an everting catheter 3.5 mm in diameter designed for endovascular surgery. This device, instead of utilising an internal steering mechanism, is pre-shaped based on the target anatomical structure and grows in a pre-determined direction [13]. This approach is capable of high levels of curvature and miniaturisation, but the design is pre-determined and therefore must be manufactured to the specific anatomy of interest. Without this procedure-specific approach, natural bifurcations, such as those commonly found in the anatomy, require active steering mechanisms to navigate in a deterministic manner. Away from the medical domain, Hawkes et al. introduced pneumatic artificial muscles for steering of 25 mm diameter vine robots [8]. These inflatable pouches on the side of the robot enable steering via pressurisation at the base. However, the complexity in fabrication of these pouches has likely prevented it being applied at a smaller scale.

The Mammobot platform is one such miniaturised vine robot design for navigation of bifurcations in the mammorary glands [7]. This device utilises an internal steerable catheter to bend the vine body and has been demonstrated at a 2.9 mm diameter scale. The tendon-driven catheter is limited in its dexterity, but is capable of steering the vine through small bending angles. This design could be considered more of an everting sheath rather than a self-propelling vine robot, as its locomotion is determined by the pushing of the stiff internal tool rather than internal pressurisation. This stiff tool provides the steering mechanism for the robot but sacrifices the overall softness of the robot body and with it, limits bending curvature and overall conformity. Furthermore, a key advantage of everting bodies is the creation of locomotion force at their tip. With this approach, force is still applied from the proximal end as a conventional catheter would do.

This need for precise application of forces has given rise to the use of magnetics for robotic actuation. Here, magnetic elements within the robot body can be manipulated via externally applied magnetic fields. This avoids complex internal mechanisms whilst retaining the ability to induce precise forces on the instrument. This forms a wireless actuation methodology where the induced torques and forces are proportional to both the volume of internal magnetic material and the magnitude of the applied magnetic field and gradients.

Magnetic instruments have been designed both from hard permanent magnet elements or via integrating magnetic micro-powders (such as NdFeB) into silicone elastomers [2], [14]. The latter retains a fully soft structure throughout the device. More recently, soft robot designs have utilised magnetic fluids. These can be free-flowing magnetic fluids capable of controlling both their movement and geometry or constrained magnetic fluids placed within soft bodies [15], [16]. Leon-Rodriguez et. al. presented an untethered everting design inspired by motion of Amoeba bacteria actuated by an internal magnetic fluid [17]. This robot is pulled by magnetic field gradients, moving without relative shear and therefore low friction all whilst retaining a fully soft body.

In our previous work, we introduced an 8 mm diameter vine structure exhibiting a magnetic skin upon the vine wall which directed the growth of the robot through various vessels [18]. To enable successful eversion, vines require a sufficiently flexible, and therefore thin, wall structure. Due to this constraint, and the integration of magnetic material into the walls, the magnetic volume of this device was limited meaning the induced force and torque on the system was low. This system therefore required low separation between the external permanent magnet (EPM) and the robot for successful navigation, and was limited in terms of further miniaturisation. Indeed, the low induced magnetic force and torques meant deformation whilst the vine robot was pressurised was minimal except in the case of immediate EPM proximity. A strategy of alternate growing and steering was thus utilised making complex navigations a challenge which required large magnetic fields. This effect would be exacerbated in the presence of internal tools such as a biopsy needle, further augmenting the effective stiffness of the body and making steered navigation near impossible. We have previously explored hard magnetic tips featuring permanent magnets for vine steering at the 25 mm diameter scale [19]. This provides a large magnetic volume but sacrifices the soft body of the vine robot, leaving a hard tip. This can introduce some degree of shear translation at the tip and can therefore potentially still lead to traumatic tissue interaction, particularly in small diameter lumen. Further, for the case of tissue biopsy, where applying large forces is needed, the conformity of entire soft bodies provides a point of stabilisation, which can be leveraged

to provide greater reaction forces [20]. Table 1 summarises key approaches to vine robot steering control as well as target application.

Table 5.1: Comparison of notable steering mechanisms and their applications.

Authors	**Steering Mechanism**	**Diameter**	**Body**	**Application**
Hawkes et al. [8]	Pneumatic Artificial Muscles	25 mm	Soft	First exploration of steerable *vine* robots
Berthret-Rayne et al. [7]	Internal hard tendon	2.9 mm	Hard, stiff internal tendon	Navigation of the mammary glands
Li et al. [13]	None (preshaped to anatomical structure)	3.5 – 5 mm	Soft	Endovascular surgery
Kim et al. [19]	Permanent magnet at the tip	25 mm	Hard tip but soft body	Robotic colonoscopy
Davy et al. [18]	Magnetic skin	8 mm	Soft	Navigation of upper bronchial tree
This Work	Internal magnetic fluid	4 – 7 mm	Soft	Navigation of deep bronchial tree and biopsy of soft tissue

A biopsy is one of the most common endoluminal procedures, involving the extraction of a small tissue sample for histological analysis to differentiate between healthy and cancerous tissues. It is also one of the most challenging to achieve with soft systems, while being among the most demanding in terms of force transmission. Recent research has introduced soft robotic platforms with origami-inspired architectures that allow needle deployment, demonstrating promising results [20]. However, these designs remain limited as they require the needle to be exposed during the robot's deployment and are also constrained in their potential miniaturisation. Current approaches are also constrained in terms of force transmission with a maximum of 1 N [20], [21] whereas the required force is closer to 2 N in the case of stiffer tissues [22].

In this study, we consider vine robots driven by a pressurised magnetic fluid. By utilising a magnetic fluid we form a vine robot with an entirely soft body but also high magnetic volume, enabling growth through hydraulic pressure and steering under external magnetic

fields. We show this design to be highly miniaturisable and explore designs in the 4 to 7 mm diameter range. We show how these bodies are capable of conforming to the anatomy and are not limited by friction when navigating a lumen due to the entirely soft body of the robot.This device is capable of high curvature steering in any plane based on the positioning of the EPM. We chose tissue biopsy in the bronchial tree as a clinical case study and, by integrating an endoscopic camera and biopsy needle into our vine robot, demonstrate camera-assisted navigation within a bronchial tree phantom and the puncturing of soft tissue with a needle, leading the way towards clinical application.

In summary, we make the following contributions:

- The introduction of a uniquely miniaturised vine robot capable of creating high body forces for steering via magnetic fields but crucially retaining robot body softness whilst producing forces at the tip greater than 1 N.
- An evaluation of this robot at various diameters and its ability to navigate tight lumen.
- A pre-clinical study of the application of this unique robot to tissue-biopsy procedures in the lungs through a clinically relevant phantom.

5.4 Fundamentals

5.4.1 Eversion

Vine robots take a simple form. The outer body is that of a thin-walled flexible tube, inverted into itself creating a double layer that is enclosed at one end (hereby referred to as the vine tip (See Figure 5.1B. Pressurisation of this internal cavity causes the internal material to be expelled at the tip, leading to elongation of the body in a process known as vine eversion or growth. Constraining the internal material (the vine tail) and management of its release, allows the eversion process to be regulated. As the vine body is growing from the tip rather than translating relative to the enviroment, external friction is negated, with the only friction in the system being within the vine body between

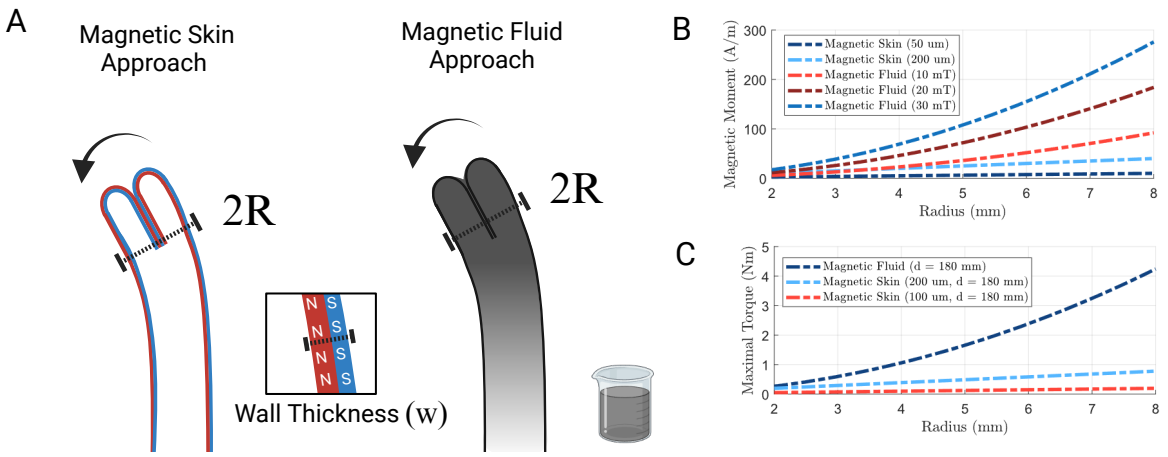

Figure 5.2: A) Diagram demonstrating the significant increase in magnetic volume achieved with the magnetic fluid approach of this work, rather than the magnetic skin approach of our previous work [18]. B) Graph comparing magnetic skin to magnetic fluid under various fields and wall thickness for a 50 mm length vine (See Appendix for details). C) Graph showing maximal induced torque under rigid body assumptions between the two approaches given an EPM of diameter 101 mm, length 101 mm (R_e = 1.44 T) was positioned 150 mm away.

everted and inverted material.

Due to this frictionless shear-free navigation, vine robots are of great interest for applications in endoluminal surgery [7], [13], [18]. Traditional instruments are often formed of hard bodies and locomote via pushing from their proximal end (Figure 5.1A). In contrast, vines are formed of entirely soft bodies and locomote via growth rather than translation. This has the potential to reduce potentially traumatic tissue interaction with vessels within the body and could enable navigation to areas of the anatomy that would traditionally be considered unreachable or too dangerous to access [18]. Further, the inherent channel within the vine tail, can be utilised for irrigation, or incorporating standard endoscopic tools such as a biopsy needle, allowing useful access deep within the human anatomy.

5.4.2 Magnetic Fluids

Vine robot designs have been proposed which utilise both pneumatic and hydraulic pressurisation for eversion. In this work, we propose a vine robot actuated via an internal magnetic liquid. Here, pressurisation leads to vine growth, steering of the robot across

bifurcations is achieved through magnetic attraction. Forces can be applied directly to the magnetic fluid via application of external magnetic fields. Magnetic fluids typically take the form of dispersed magnetic particles in a carrier liquid and can be categorised into ferrofluids and magnetorheological fluids [23]. The former is commonly formed from magnetic nano-particles in permanent suspension, often in a highly toxic petroleum based carrier liquid. Alternatively, magnetorheological fluids are based on much larger particles in the micron range. The carrier fluid is typically water or oil and are typically of a greater magnetic volume (20 - 40%) than ferrofluids (10 - 20%). However, due to their large particle size and concentration, the suspension is only temporary. Typically, these fluids utilise a thixotropic agent to stabilise the fluid and reduce sedimentation [24]. Magnetorheological fluids are named as they exhibit the magnetorheological effect. This effect is characterised by the dependence of the material's viscosity on the applied magnetic field. This is due to the alignment of particles once magnetised, forming chains within the material and under certain conditions, this fluid can even become a viscoelastic solid. For magnetic fluids, the ability of the suspended magnetic particles to freely rotate means that they will align with the direction of applied field near instantaneously (constrained only by viscosity). Consequently, for magnetic fluids, no material torque will be present and any actuation will be purely gradient-force based. In the case of manipulation with external permanent magnets, this force will be directed towards the poles of the EPM.

As mentioned previously, our earlier work considered vine robots with a magnetic skin [18]. This utilised hard magnetic NdFeB micro-particles which store a much higher remanent magnetisation under typical fields. However, the inherent requirement for vines to be formed of thin-wall materials limits the overall magnetic volume. In Figure 5.2, we compare the approach of magnetic fluid with that of magnetic skin for a 50 mm length vine. Full details of assumptions made are provided in the Appendix. It can be observed that the magnetic fluid approach produces a significantly higher magnetic moment across these small scales and results in much higher actuation torques whilst retaining the soft structure, motivating this new design of miniaturised magnetic vine robot.

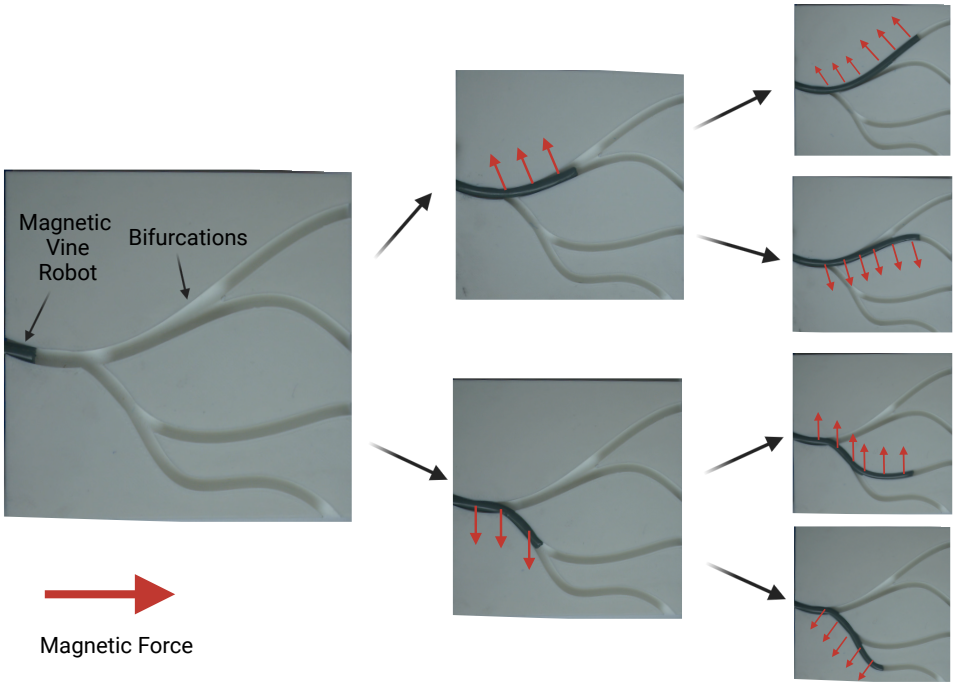

Figure 5.3: Figure showing navigation of tight bifurcations. Movement of the external EPM creates a net magnetic force on the entire robot body. As the vine robot everts, the direction of this growth can be controlled by manipulating the magnetic field with the EPM. Despite this force being experienced across the whole body, the constraint of the lumen permits only the tip to be manipulated.

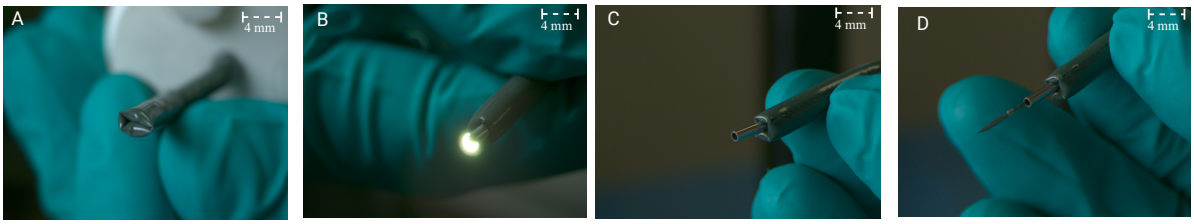

Figure 5.4: A) A vine robot of 4 mm diameter filled with magnetic fluid. B) An optical fibre inserted into the vine. C) Retracted biopsy needle. D) Extended biopsy needle.

5.4.3 Functionalisation

The use of tools such as biopsy needles in vine robots presents a significant challenge. Due to the everting structure, no part of the material body can be defined as the permanent tip and therefore no direct attachment point is available. This is further exacerbated by the fact that the internal material moves at twice the speed of the tip. This leads to the so-called *spitting* problem in which anything placed within the vine's inner channel is ejected as the vine everts. Furthermore, the pressurisation of the vine body contracts onto this inner channel, preventing free movement of tools. Therefore, any device needing to

maintain position at the tip of the robot during growth must somehow be synchronised with the eversion process. This can be achieved by a duty cycling of pressurisation, growth, depressurisation and then tool retraction [7]. Given the vine robots' ability to navigate constricted channels without friction, this contact can be exploited as a point (or area) of stabilisation for applying large forces (such as those required for tissue penetration) at the robot tip. This however does require the channel to be smaller than the vine robot's nominal diameter.

With the combination of fluidic actuation for growth and an internal magnetic fluid enabling steering, magnetic-fluid driven vine robots retain the simplicity of vine robot form, exhibit an entirely soft robot body, and give rise to the potential for a highly miniaturised design. Given our requirement for the use of tools with the vine robot, the relative high forces and torques of the magnetic fluid approach solves this, preserving the soft body but giving the operator a high degree of control, all whilst providing an intuitive control system via positioning of an external magnet. The magnetic fluid within the robot's structure creates forces under a gradient magnetic field that act on the entire body, not just the tip. "Body steering" methods are well-studied in pneumatic vine robots and have been demonstrated for navigating various complex environments [25]. In constrained environments such as bifurcations and narrow lumens, the robot's body is constrained with little freedom for movement allowing tip-focused navigation via manipulation of the magnetic field (see Figure 5.3).

In the following sections, we will develop a methodology for evaluating the potential of these robots for navigation within the anatomy via endoscopic camera for positioning of a biopsy needle for target applications in minimally invasive surgery (see Figures 5.1 and 5.4).

5.5 Materials and Methods

5.5.1 Vine Robot Body

The vine robot body must be formed of a thin-wall and sufficiently flexible tube in order for successful growth under eversion. Based on previous work, we selected a 38 μm thick thermoplastic-elastomer (TPE) film (Stretchlon 200, Airtech Advanced Materials, UK) as our vine material. For these thin geometries, this material (E = 10 MPa) is flexible but can be considered of low extensibility at our operating pressures. The low melting point of the material allows it to be easily sealed with heat. We utilise a laser-welding technique to form the vine into a layflat tube of length 290 mm [26]. This is achieved first by soft sealing two layers of the material at 100 °C on a heat press (Combo Heat Press, Creworks, USA) for two minutes to bring the two layers into close contact. The pressure of the heat press was manually tuned to allow the layers to be adhered but separable by hand. After this, the tube was formed using an optical laser cutter (Creality Falcon 2 Pro 22W, Creality, China) to simultaneously seal and cut (See Figure 5.5A). The width of the layflat tube corresponds to $\pi/2$ of the inflated body diameter. The parameters utilised for the laser cutter were determined empirically. A speed of 2,733 mm/min with a laser power of 50% was found to give a seal that was not prone to leakage. Once cut, the vine body was then inflated and checked for leaks. The completed vine is of length 145 mm. Once pressurised, due to the elasticity of the vine material, the diameter will increase slightly. However this is shown to be less than 1 mm under typical operating pressures (See Appendix).

5.5.2 Magnetic Fluid

Due to the toxicity and relatively low magnetic volume of commercial ferrofluids, we utilised an iron-water suspension for the magnetic growing fluid within the robot. The fluid was manufactured as outlined in McDonald et. al. [24]. This fluid was selected due to its simplicity and the intrinsic biocompability of its constituent parts. Firstly,

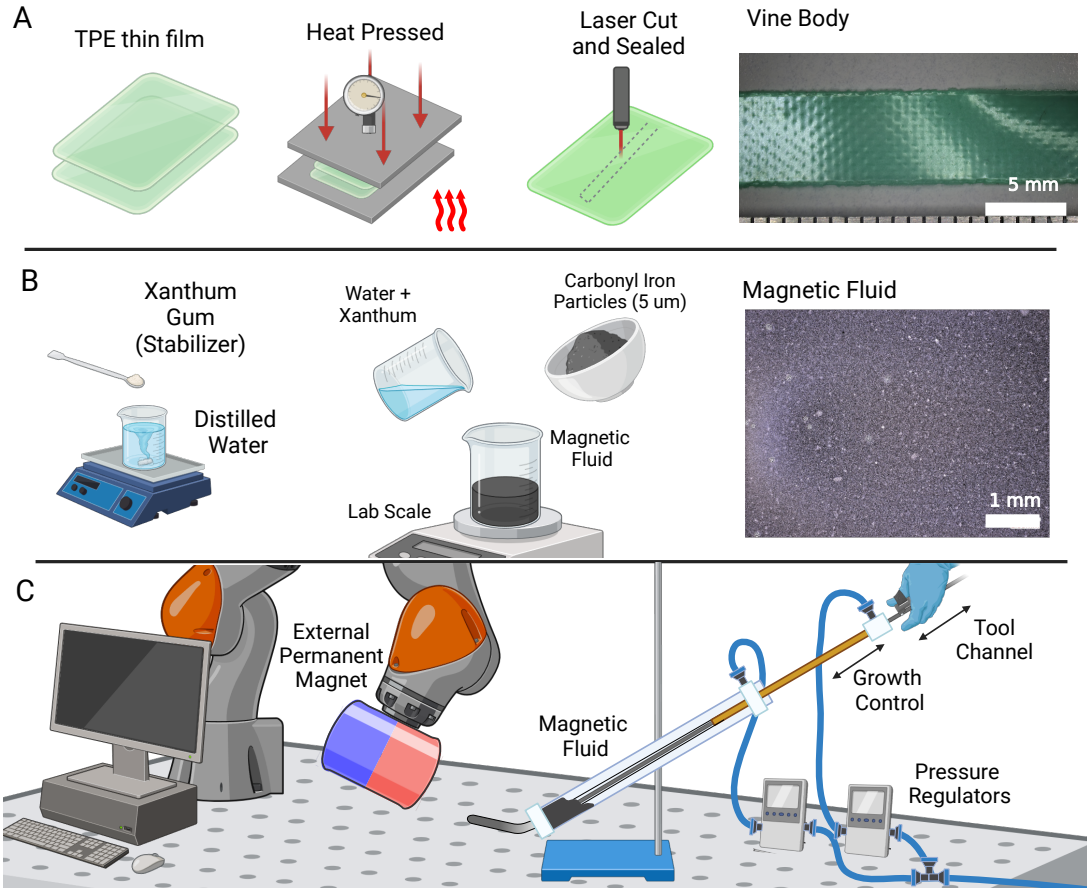

Figure 5.5: A) Fabrication of the vine body. Two layers of thermoplastic-elastomer are layered and are softly heat pressed to form a temporary bond. The laser cutter seals and cuts the vine body. B) Preparation of the magnetic fluid. Xanthum gum acts as a stabiliser to maintain a suspension of the iron particles. C) The vine robot is steered using an external permanent magnet (EPM) mounted to a robotic manipulator. The vine's growth is controlled via insertion of a TPU tube that also provides a tool channel.

0.2% by weight xanthum gum was mixed with water, then 23% by volume carbonyl iron particles (1-6 μm mean particle size, 98% purity, GF42083210, Goodfellow) were added. The mixture was then mixed at 1,600 RPM for two minutes. The xanthum gum acts as a stabiliser, prolonging the suspension of the particles (See Figure 5.5B). Through experimentation, it was found the fluid remained in an adequate suspension for up to 12 hours, after which point settling of the iron particles could be observed (See Appendix). Repeating the mixing stage however, again dispersed the particles. This will affect the lifetime in which the robot can be used before the magnetic fluid needs to be replaced. Carbonyl iron particles were selected due to their high purity and iron's intrinsic high magnetic susceptibility.

5.5.3 Hardware

For creating the external field for magnetic manipulation, a robotic manipulator (iiwa14 LBR, Kuka, Germany) was used with a large External Permanent Magnet (EPM) (101.6 mm diamater, 101.6 mm length, N52 NdFeB) as an end-effector (see Figure 5.5C). The pose of the EPM was controlled in end-effector space via an external gamepad enabling teleoperated control by the user. The vine body was attached to a clear tube where pressure could be applied and was inverted with the tail attached to a smaller internal tube (see Figure 5.5C). This internal tube manages the growth of the vine and also permits tool insertion into the vine body. Magnetic fluid was inserted into the outer tube filling the vine. Metallic components were deliberately avoided in the base mechanism to prevent influences on the magnetic field. Given the relatively weak field produced by the magnetic fluid reservoir itself, this has a negligible effect on the vine robot's performance. An electronic pressure regulator (ITV1010-211BL, SMC, USA) was used to pressurise the air above the magnetic fluid in order to control the vine pressure. A secondary regulator was also used to equalise the pressure in the internal tool channel. This equalising pressure reduces friction within the tool channel allowing the tool to be inserted and retracted from the vine.

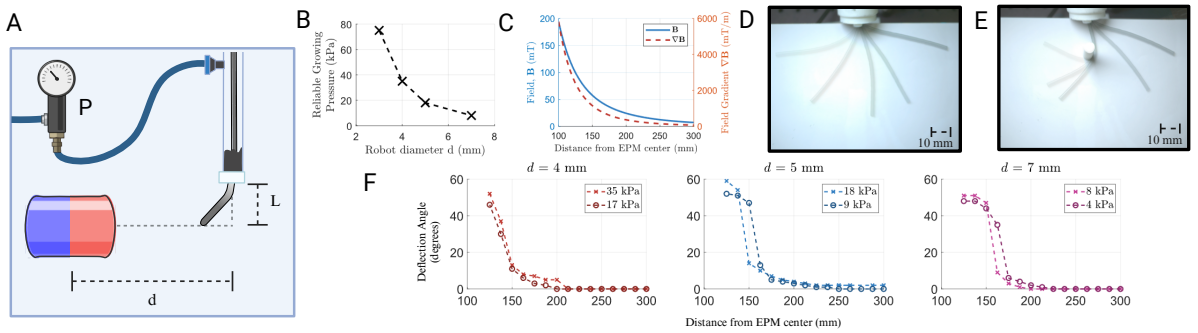

Figure 5.6: A) Experimental setup for analysis of deflection of the vine under varying external fields. The distance between EPM and vine base d is varied causing a deflection of the vine body. B) Vine diameter versus reliable growing pressure. The high pressure of the 3 mm vine made it prone to bursting. C) The magnetic fields and field gradients produced by the EPM ($|\mathbf{m}| = 970.1$ A/m) under dipole assumptions. D) Deflection of the vine on a planar surface with an external magnet. E) Deflection of the vine in the presence of an obstacle. F) Vine deflection versus distance from the EPM at the reliable growing pressure and half the reliable growing pressure.

5.6 Results

5.6.1 Growing and Steering

Four vine robots were produced with 3, 4, 5 and 7 mm diameters respectively. Each was inverted and the internal pressure increased until the vine began to evert. This was repeated three times until a reliable growing pressure for each diameter vine was established (see Figure 5.6B). As can be observed, smaller diameter vines require larger pressures to evert. This can be attributed to their smaller tip surface area and greater friction within the body. The high pressures required for the growth of the 3 mm vine (75 kPa) provoked bursting and therefore this diameter was not further analysed.

Each vine was analysed for ability to deflect with the external magnet. The vines were placed vertically and the EPM was introduced causing deflection (See Figure 5.6A). The vines were pressurised to their respective growing pressure and grown to a length $L = 50$ mm whilst the EPM distance d was varied. The EPM was vertically positioned so the tip of the vine aligned with the central axis of the EPM at rest. This process was repeated at half the growing pressure. For each measurement, we performed a total of three experimental repeats. It can be observed that pressure has little effect on deflection. Indeed,

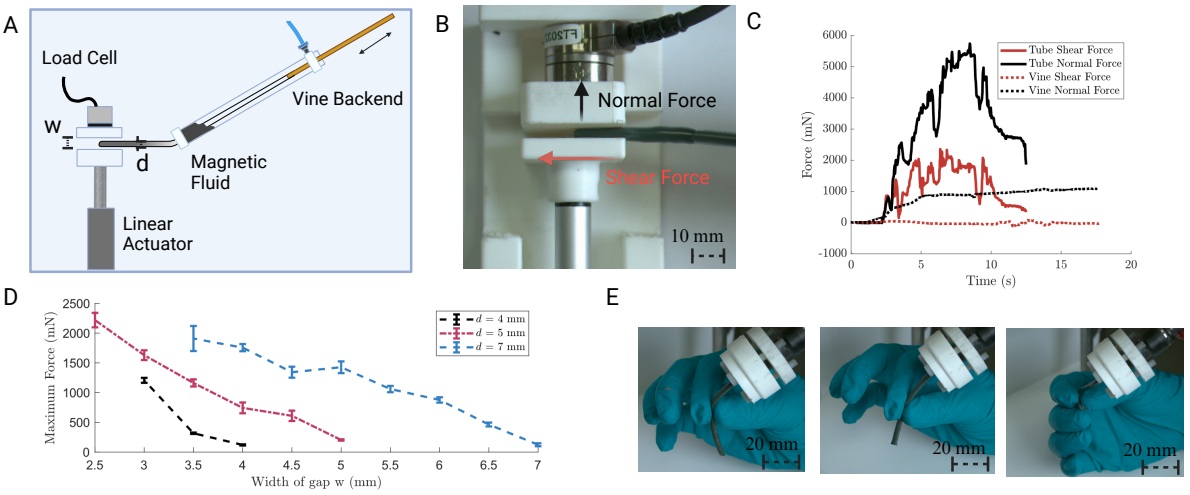

Figure 5.7: A) Schematic experimental setup for evaluation of forces during vine locomotion. B) Real experimental setup showing directions of normal and shear forces. C) Comparison of insertion of TPU tube with vine robot (both 5 mm diameter). The vine robot produces near zero shear forces and a reduction of normal force of 72.54%. D) Maximum force of insertion versus width of gap navigated for 4, 5 and 7 mm diameter. E) Conformity and reliance of the robot body to external forces.

deflection is minimal up to a critical distance at which the vine deflects sharply towards the EPM. This critical distance was approximately 160 mm for all vines corresponding to a magnetic field of magnitude of 56 mT and field gradient of 1,134 mT/m. The maximal achieved deflection for each of the vines against gravity was 52°, 59°and 51° respectively (See Figure 5.6F).

Figure 5.6D shows the deflection of a 4 mm vine with an external magnet. Here the vine lays flat on a surface. It can be observed that without gravity acting directly against the deflection, vine bending is much more controllable and a variety of deformations can be achieved demonstrating deflection up to 70°. Further, Figure 5.6E shows how the vine can still be deflected in the presence of an obstacle, the soft body allowing it to conform to the environment (see Supplementary Video 1).

5.6.2 Squeezing

A key characteristic of vine robots is their ability to squeeze through gaps smaller than their diameter. Our magnetic fluid driven vine with its entirely soft body retains this property. In the clinical case, it is important that the vine can navigate through vessels

without application of large forces on surrounding walls. To explore this, we grew vines through a variable width gap of length 25 mm. This gap width was varied via a linear actuator (See Figure 5.7A and B). We quantified the forces applied in the shear and normal directions utilising a six axis force sensor (Nano17, ATI Industrial Automation, USA) repeating three times. Figure 5.7D shows the maximum applied normal force for 4, 5 and 7 mm vines for varying gap widths at their respective established growing pressures. Where the vine was not able to squeeze through the gap, the data is not presented. Notably, the 5 mm vine is capable of squeezing through the smallest gap of 2.5 mm outperforming the 4 mm vine in this metric. This can be attributed to the fact that although friction will be greater in the larger diameter vine (due to the increase in tail material), the surface area of the tip is larger and therefore a larger growing force is produced.

In Figure 5.7C, we compare the vine's shear and normal forces to the insertion of a soft tube (O.D 4 mm I.D 3 mm, TPU) with a 4 mm magnetically driven vine through a 3 mm gap. Over three repeats, we consider the average peak force produced. As would be anticipated, the vine creates near zero shear forces (10.3 mN) under insertion, compared to the average peak of 1.04 N by the tube. The vine does produce some normal forces (2.87 N) however they are considerably less than the tube insertion (7.88 N).

5.6.3 Biopsy Forces

When the vine is in contact with its surroundings it can stabilise via anatomical contact and exploit this stability to apply large tip forces. We consider the application of tissue biopsy procedures. A biopsy tool formed of a hollow needle tip (20G, 0.91 mm diameter) was attached to a modified thin-wire endoscopic tool (FG-25d retrieval tool, Olympus, Japan) and inserted into the vine robot. We evaluated the vine's ability to apply a force at the tip, given its grown length. A load cell was positioned at the tip of the vine, and the tool was inserted into the vine robot. The maximum force was recorded just before the robot began to buckle at its base. A stabilisation point was added between the vine and the load cell (see Figure 5.8A and C). The vine had a diameter of 5 mm, while the

circular stabilisation point had a diameter of 4 mm. The robot's grown length was 75 mm and the internal vine pressure was 35 kPa. Two scenarios were examined: in the first, the vine was aligned parallel to the load cell (Figure 5.8A, Scenario S), and in the second, the vine was oriented perpendicular to the load cell (Figure 8C, Scenario C). The maximal force was recorded for varying distance d between the stabilisation point and the load cell over three repeats. Figures 5.8B and C plot the maximal force with respect to d. Finally, in each of the scenarios the vine was deflated to represent the case of no stabilisation on surrounding anatomy. It can be observed in this case of no stabilisation the force output was significantly less than with the vine acting to stabilise the tool. The maximal force output was 1.05 N and 1.26 N in each of the scenarios respectively. This is dependent on close proximity between the stabilisation point and applied force. This represents the need for stabilisation close to the target tissue in the case of high tissue stiffness.

In Figure 5.8E, we demonstrate the ability to steer the vine robot with the inserted needle via movement of the EPM. At 75 s the vine robot is positioned accordingly and the soft tissue phantom is penetrated (see Supplementary Video 2).

5.6.4 Navigation

Table 5.2: Table describing average times for the navigation experiment in Figure 5.9.

Navigation	**Path Length (mm)**	**Success Rate**	**Mean Time (s)**	**Standard Deviation (s)**
i	112	4/4	69	19
ii	99	4/4	109	14
iii	104	4/4	125	27
iv	61	4/4	110	30

To evaluate the ability to navigate through bifurcations, we utilised a 3D-printed phantom of a bronchial tree (LIDC-IDRI-0807) (www.cancerimagingarchive.net). The vine robot (5 mm diameter) was positioned at the base of the trachea and the system was placed within the workspace of the manipulator and EPM (see Figure 5.9). To track the position of the vine robot, a LED fibre was inserted into the tool channel and the duty cycling approach (as described in Section 5.4.3) was applied manually to maintain the fibre at

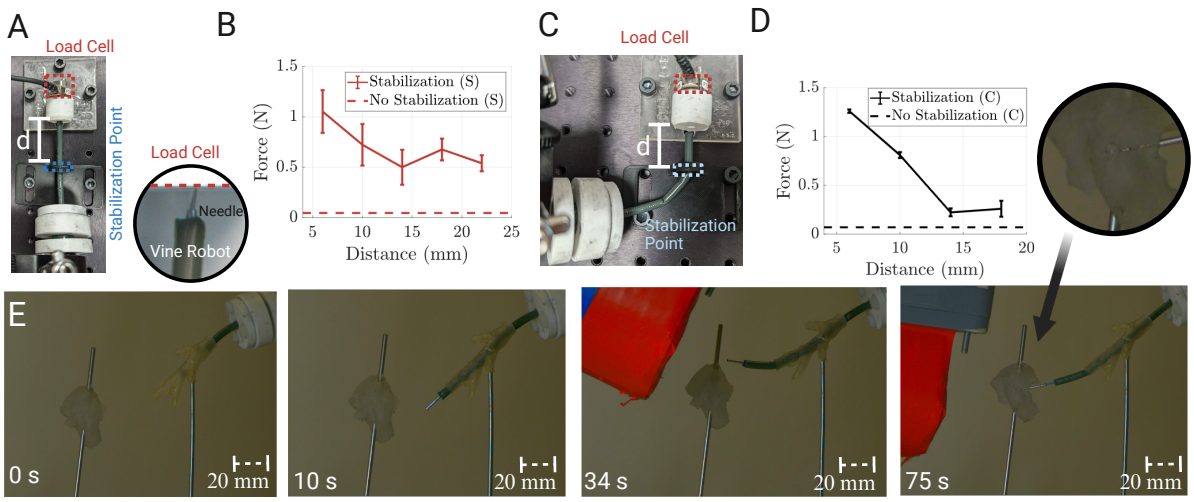

Figure 5.8: Experimental setup to quantify maximal force output of the biopsy needle with respect to stabilisation of the robot. A) Scenario S (Straight). The stabilisation point and load cell are parallel with the robot base. B) Maximal force output before buckling with varying distance d with and without stabilisation for Scenario S. C) Scenario C (Corner). The stabilisation point and load cell are orthogonal with the robot base. D) Maximal force output before buckling with varying distance d with and without stabilisation for Scenario C. E) Manipulation of the vine with the biopsy needle inserted through the tool channel via movement of the EPM. At 75 s the needle is extended to penetrate a piece of a soft tissue phantom.

the tip during growth. Four target areas of the bronchial tree were established and four repeats were performed. The robot manipulator was controlled via the joystick to position the EPM. The average time for the four navigations and path lengths is specified in Table 5.2. Due to the magnetorheological effect, some small stiffening of the vine was found to inhibit growth at close proximity to the EPM. Therefore, the EPM had to be intermittently retracted to a greater distance to allow growth (see Supplementary Video 3). A detailed exploration of this phenomenon is beyond the scope of this work but is addressed in the conclusion.

5.6.5 Clinical Case Study: Peripheral Lung Biopsy

Finally, we demonstrate the use of the magnetic fluid driven vine robot (5 mm diameter) in a bronchoscopy training simulator for the application of tissue biopsy (Ultrasonic Bronchoscopy Simulator, Adam Rouilly, UK). We attach a NanEYE 1mm x 1mm RGB CMOS camera (AMS-OSRAM, USA) to the end of the optical fibre and implement

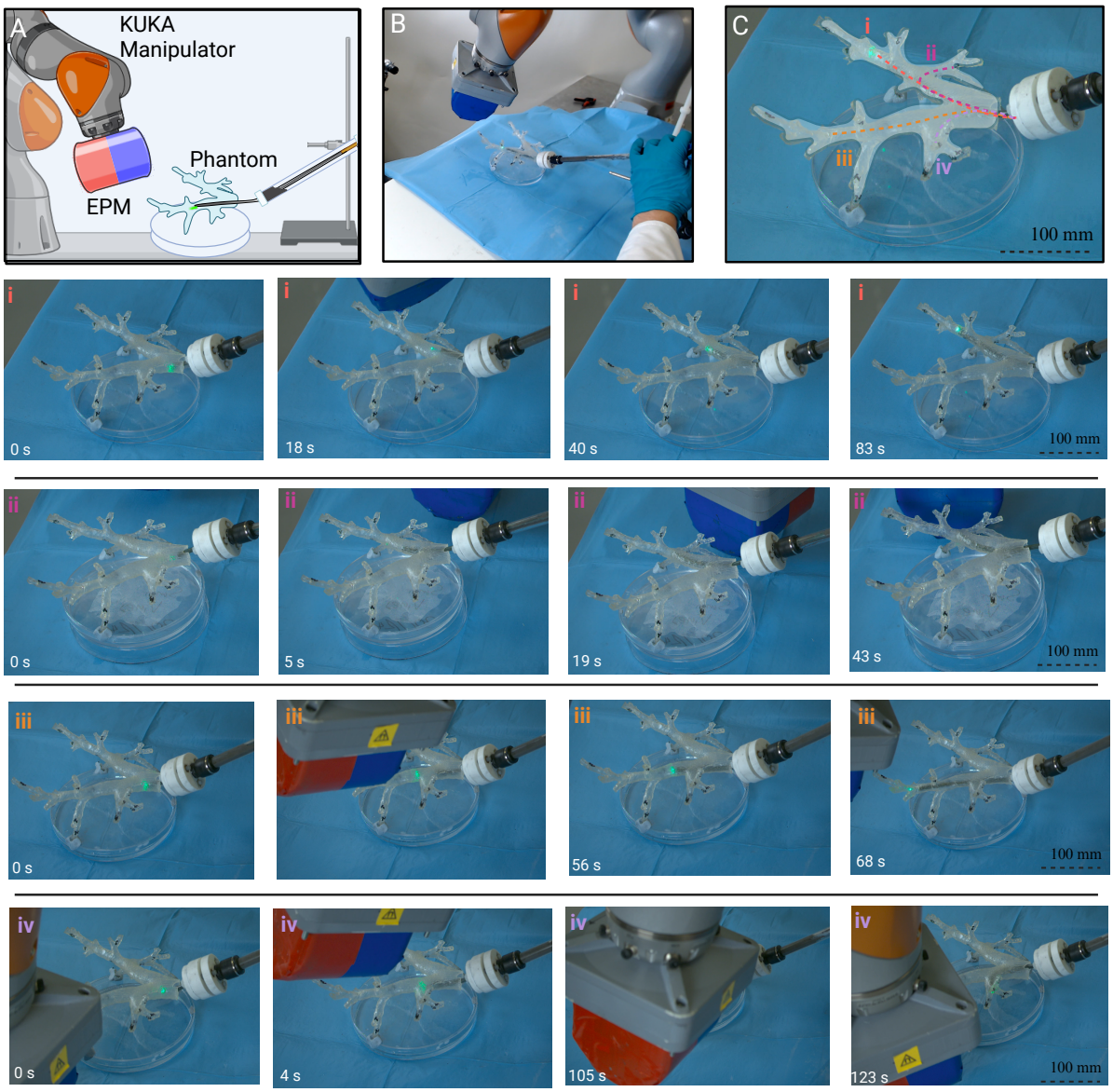

Figure 5.9: A) Diagram of experimental setup. The phantom is placed within the workspace of the manipulator and the vine robot introduced to the start point. The EPM is then manipulated using a gamepad to direct the vine robot through the phantom. B) Real-world experimental setup. C) Diagram showing four target paths on the phantom.

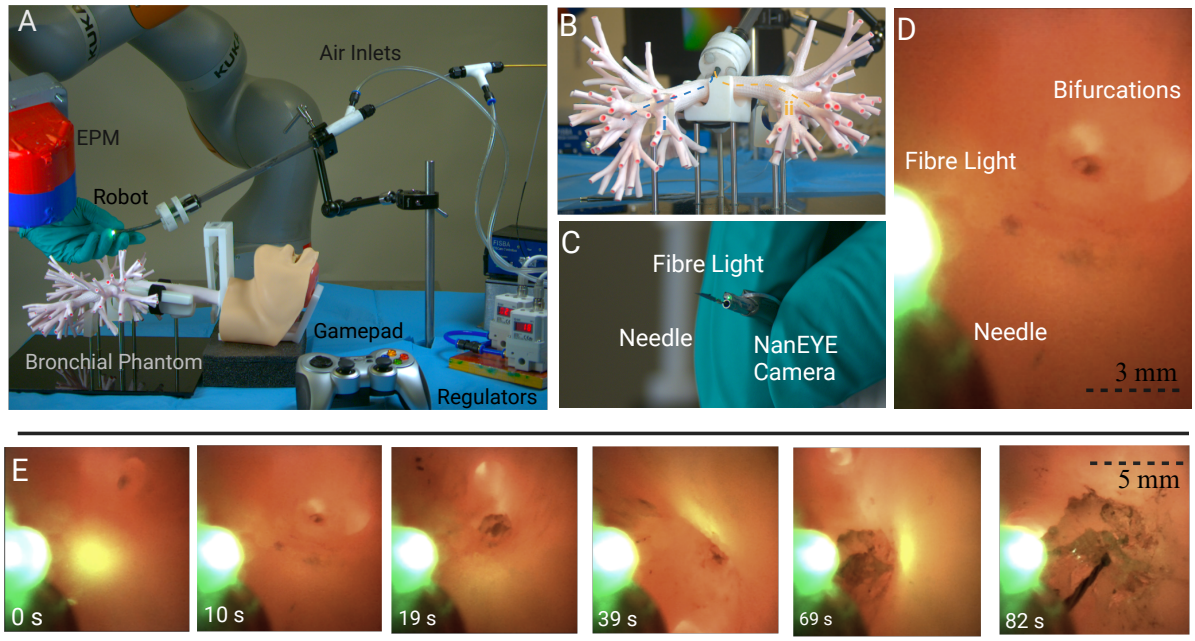

Figure 5.10: A) Real world experimental setup. B) Bronchial tree phantom. C) NanEYE camera mounted to fibre with tissue biopsy needle. D) Features as seen by the internal camera. E) View from endoscopic camera in navigation (i), reaching a target tissue and penetration with the biopsy needle.

camera assisted navigation (see Supplementary Video 4). The wire for the camera was kept external of the tool channel for simplicity of attachment, but in the future would be integrated into the vine tool channel. The same duty-cycle approach was applied for keeping the illumination fibre at the tip, with the secondary pressure source utilised for further reduction of friction within the body. Two target areas were established and the EPM manually positioned. The navigation was completed using the internal camera for approximate location and visual inspection of the phantom was used to correlate this with the real bifurcation. In a clinical setting, this step would be preformed with a pre-operative CT scan of the lungs. The navigations were repeated four times with 100% success rate averaging 92 and 140 seconds respectively and standard deviations of 15 and 33 seconds. Figure 5.10E shows the first navigation, from the endoscopic camera. After reaching the target anatomy, the needle is inserted into a piece of soft phantom tissue, replicating a biopsy procedure. The ability to penetrate the target tissue is assisted by the vine robot's stabilisation on the surrounding vessel.

5.7 Discussion and Conclusion

Whilst the pressurisation of everting structures allow them to locomote, the steering of miniaturised vine robots has proven challenging. A magnetic fluid used in lieu of air or water serves the simultaneous purposes of growing the vine under pressure whilst also enabling steering via deflection under magnetic fields. This novelty retains the entirely soft structure of the vine allowing squeezing through gaps and fully compliant behavior along the vine's length. The simplicity of the structure allows for the miniaturisation of the device enabling bending in any arbitrary plane, given the EPM can be appropriately positioned. Via teleoperated control, under feedback from a tip mounted camera, the robot can accurately position a biopsy needle. The work of Li et al. [27] observed that pressures up to 62 kPa did not visually damage any tissue in their bronchoscopy soft robot. Our demonstrated platform operates at pressures well below this value, with a maximum required growing pressure of 35 kPa. Further clinical studies of the safety of these pressures in the lungs will clearly be needed.

The functionalisation via a biopsy needle, shows a clinical use case for such robots, where the vine's ability to stabilise on surrounding lumens and apply large tip forces enables penetration of soft tissue. This, combined with the shear-free movement and soft body of the robot holds the potential for reduced traumatic tissue interaction compared to traditional tools. In the work of Van Lewen et. al, to achieve a 1 N penetration force, a pressure of 200 kPa was needed which could potentially be dangerously high. Our work, via stabilisation near the robot tip, is capable of a 1.26 N penetration force with a significantly (82%) lower pressure of 35 kPa [20]. The ability to create these large tip forces is dependent on vine stabilisation. Therefore, the vine robot diameter must be appropriate for the anatomy. Future work will consider how variable vine robot diameters can be digitally manufactured based on pre-operative imaging, including tapered designs and hyper-elastic ballooning vine robots capable of conforming to a wider range of lumen diameters [20].

In our previous work, we adopted an approach based on a magnetic skin for the vine

robot [18]. This approach was constrained to very low magnetic volume thus limiting any induced magnetic wrench which, coupled with requisite growing pressures, limits achievable deformation. In this work, the use of a magnetic liquid gives a relatively high magnetic volume (over 95% by total volume of the robot) and therefore allows vines to be steered and grown simultaneously. The drawback to this approach is the magnetorheological effect which stiffens the fluid under high magnetic fields enforcing a balance between wrench and stiffening. Whilst this characteristic could potentially be leveraged for a variable stiffness design, in the case of navigation (being discussed here) it is not helpful. A potential solution to this challenge would be the use of a magnetic fluid with low magnetorheological behaviour. Approaches to this include the use of smaller magnetic particles (nano-particles) whose chaining would likely be less significant on the bulk material properties. This would also come with the advantage of prolonged or permanent suspension of particles. With iron and water as the main ingredients, the iron suspension utilised is biocompatible, however, the effect of leakage of a large volume of iron into certain anatomies could potentially be dangerous. A current device used in clinical practice named EndoRail [28], utilises a similar iron-water suspension for assisting during colonoscopy procedures, further supporting the clinical viability of this technique. Future work should more closely consider the fluid of choice with respect to both magnetorheology and the risk of leakage pertaining to the specific procedure investigated.

The 5 mm robot demonstrated enables navigation up to the fourth generation of the bronchial tree [29] but further miniaturisation will be needed for deeper peripheral lung access. Our thermoplastic elastomer and laser sealing process enabled customisable vine diameters, essential for comparative studies, though the 3 mm design struggled with burst pressure limitations. Scaling down vine diameters increases the required growing pressure quadratically and therefore resistance to higher pressures is vital for miniaturisation. Alternative approaches for forming cylindrical TPE structures include the heat pressing method of Rogatinski et al. (capable of holding pressures up to 300 kPa) and extrusion of thermoplastic elastomeric cylinders which would completely eliminate seam sealing

[30]. Miniaturisation could also benefit from stronger polymers like LDPE or PTFE along with friction-reducing lubricants or hydrophilic coatings [12]. The magnetic fluid approach is inherently easier to implement at smaller diameters compared to other vine steering methods (as shown in Table 1) due to the lack of complex structures in the vine body. Further developments in vine wall material and construction techniques will allow the development of fully steerable vine robots at scales suitable for navigating tighter lumens.

The stiffening of the magnetorheological fluid was found in some cases to inhibit growth and therefore the EPM had to be withdrawn to allow growth. This stiffening could however be utilised for the application of large forces for stabilisation and tissue interaction. Magnetorheological fluids have been explored for stiffening within soft robotic systems however do rely on large magnetic fields [31] (436 mT for a 344% change in stiffness). Other approaches to stiffening could also be explored such as granular or layer jamming however they have proved challenging at very small scales [32]. Alternatively, low melting point alloys have been explored for vine stiffening and demonstrated at a 6.4 mm diameter scale [33] achieving a 2100 % stiffness change but requiring heating to 62 °C to achieve transition. This approach can of course result in the heating of surrounding tissue which has the potential to limit clinical viability.

When compared to pneumatically steered vine robots based on inbuilt pressurised pouches our design provides a simple structure much more compatible with miniaturisation requirements. Smaller vine robots have been presented based on steerable internal tendons however these sacrifice the vine's fully soft structure and the presence of complex internal mechanisms hinder further miniaturisation. With the correct materials and manufacturing, magnetic fluid-driven vines should be viable at a significantly smaller scale as long as the material is capable of eversion. Our work has focused on the control of the direction of growth of the vine robot, however, given the body-steering methodology, it may be possible with localised field gradients to control the whole body enabling more complex deformation and shape control. Future work could consider applying this to compensate for movement in the lungs during respiration [34].

Once a vine has navigated to the area of interest, its retraction must also be considered. The naive approach of simply retracting the tail leads to vine buckling for anything other than a straight vine. This is true of all soft vine robot methodologies independent of actuation approach [25]. In our case, we removed the vine from the anatomy simply by deflating it to reduce its diameter and pulling it from the proximal end in a similar manner to a standard endoscopic tool. However, an ideal system would invert the vine in the opposite manner to the eversion process, enabling shear-free movement for both insertion and retraction. Active retraction systems based on complex internal mechanisms that retract the vine material have been developed [35], however applying systems such as these to highly miniaturised vines remains an open challenge. Others have considered the use of stiff internal tools to aid retraction, however this sacrifices the soft body of the robot [7] [36]. The use of magnetics for stabilisation during retraction has also been explored, however this approach currently relies on high magnetic volumes and high fields [19]. Future work will consider retraction mechanisms suitable for magnetic fluid driven vines at this scale.

The minimal growing pressure for a vine robot depends on path-independent properties (e.g., material, thickness, viscosity, and diameter) and path-dependent properties (e.g., grown length and curvature) [11]. While this work uses a reliable experimentally determined growing pressure (Figure 5.6B), future studies will explore qualitative models, especially considering the influence of magnetic fields on fluid viscosity. Modeling the deflection of magnetic fluid-driven vine robots is challenging due to complex interactions between the flexible pressurised walls, magnetic properties, fluid behavior and the anatomy through which the robot travels. These effects are difficult to predict using current methods. The simple model presented in Figure 5.2, compares magnetic fluid with magnetic skin but neglects many complexities, such as demagnetisation effects and fluid suspension behavior, focusing instead on maximal torque. Future research should develop detailed models of these phenomena. Combining these models with internal sensing will enable a closed-loop control strategy, giving rise to more intuitive robotised systems.

The focus of this work has been on the exploration of a novel approach to vine steering, the

design of suitable magnetic fluids, relevant hardware and potential application in tissue biopsy procedures. The control approach has been manual with the manipulation of the EPM pose via a gamepad. Compared to other magnetic manipulation systems based on hard internal magnets, the use of magnetic fluids which instantly align with the magnetic field, provides a relatively intuitive system to control via a gamepad. Nevertheless, due to the low magnetisation of soft magnetic materials when compared to their magnetically hard counterparts, the required distance between EPM and internal robot continues to be smaller than a clinically ready system. Future work will consider either increasing the magnetic volume of the magnetic fluid or alternate magnetic manipulation systems capable of generating larger magnetic field gradients. The duty-cycle approach adopted for holding tools at the tip was also operated manually. This should be automated as seen in previous work in order to improve the usability of the system, lowering the task burden and allowing growth to also be controlled via the gamepad [7]. It would also be desirable to implement a closed loop control strategy within this framework. This could be approached via Fibre-Bragg shape sensors or by integrating magnetic field sensors into the robot [37], coupled with appropriate modeling of the vine and of interactions with magnetic fields and the surrounding physical environment [38].

Here we have demonstrated the possibility of utilising magnetic fluid for the steering actuation of miniaturised vine robots. We have demonstrated the functionality of these robots at diameter scales from 4 to 7 mm and explored their application in minimally invasive tissue biopsy procedures. Further miniaturisation is dependent on the ability to form thin-walled flexible tubes which can withstand higher pressures. This will provide new avenues for the application of magnetic fluid driven vines to ever smaller lumens where their distinct advantages of mechanical compliance and zero-shear navigation can be further leveraged.

5.8 Appendix

5.8.1 Calculation of Magnetic Moment and Torques

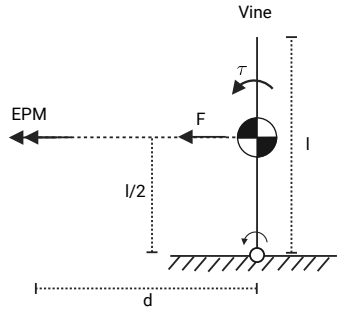

Figure 5.11: Diagram showing rigid body assumptions used in the mathematical analysis comparing magnetic skin and magnetic fluid approaches discussed in section

For the case of magnetically hard skin, the magnetic moment when magnetised orthogonally to the main axis is calculated as

$$|\mathbf{m}_s| = |\mathbf{m}_{\text{outer}} + \mathbf{m}_{\text{inner}}| = |\mathbf{m}_{\text{outer}} - \mathbf{0}|, \tag{5.1}$$

as given in our previous work [18] where $\mathbf{m}_{\text{outer}}$ is the moment of the outer everted layer and $\mathbf{m}_{\text{inner}} = \mathbf{0}$ is the moment of the inner tail, equal to zero in the case of orthogonal magnetisation. Given the hard magnetic material utilised and an actuating field significantly below that of the saturation magnetisation,

$$\mathbf{m}_s = \frac{\mathbf{B}_r V}{\mu_0} \tag{5.2}$$

where $\mathbf{B}_r$ is the remanent magnetic flux density vector. μ_0 is the magnetic permeability of free space and V is the volume of the everted magnetic skin equal to $2\pi rwl$, where r is the robot radius, w is the skin thickness and l is the length of the vine. For the NdFeB doped Ecoflex-30 silicone utilised in our previous work, $|\mathbf{B}_r|$ is equal to 0.1 T [39].

For the magnetic fluid approach, magnetic moment is a function of the applied field,

$$\mathbf{m}_f = \sigma\chi\mathbf{H}V \tag{5.3}$$

where σ is the volumetric proportion of magnetic fluid in this case equal to 0.23 as discussed in Section 5.5.2, χ is the volume magnetic susceptibility of iron equal to 4999 (dimensionless) and V is the volume of magnetic fluid in the vine equal to $\pi r^2 l$.

Maximal torques are calculated under rigid body assumptions with a pivot point at the vine base (see Figure 5.11). The vine is assumed to be positioned along the EPM major axis at a distance d and the fields and gradients are calculated under dipole assumption as given by the dipole model

$$\mathbf{B}(\mathbf{m}_e, \mathbf{r}) = \left(\frac{\mu_0}{4\pi \left\|\mathbf{r}\right\|^3}(3\hat{\mathbf{r}}\hat{\mathbf{r}}^T - \mathbb{I})\right)\mathbf{m}_e, \tag{5.4}$$

where r is the displacement between measurement and dipole position, $\mathbf{m}_e$ is the magnetic moment of the dipole, $\hat{\mathbf{r}} = \frac{r}{|r|}$, with $\mathbf{H} = \frac{1}{\mu_0}\mathbf{B}$ in free space.

Maximal torque can be calculated as the summation of the magnetic body torque (in the case of the hard magnetic skin) and the induced moment from the magnetic force acting on the pivot point equal to

$$\tau_{\max} = |\boldsymbol{\tau} + \mathbf{F}\frac{l}{2}| = |\mathbf{m} \times \mathbf{B}| + |(\nabla\mathbf{B})^T\mathbf{m}|\frac{l}{2} \tag{5.5}$$

5.8.2 Modeling of Diametric Extension under Pressure

The stress at the vine wall can be calculated under the hoop stress equation [40].

$$\sigma = \frac{Pd}{2t} = E\epsilon \tag{5.6}$$

where P is the pressure, d is the vine diameter, t is the material thickness, E is the elastic modulus, ϵ is the strain and σ is the stress. Plotting this for vine diameters of 4, 5 and

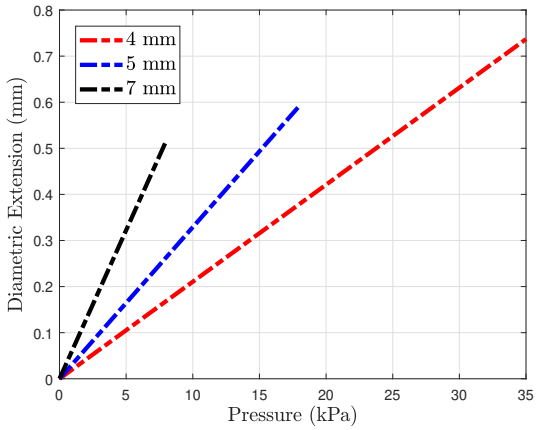

Figure 5.12: Diametric extension for various vine diameters up to reliable growing pressure as established in Section 5.6.1.

7 mm, we can calculate the diametric extension (See Figure 5.12). Pressures are plotted up to the reliable growing pressure established in Section 5.6.1 (Figure 5.6B).

It can be observed that the diametric extension is less than 1 mm for all reliable growing pressures.

5.8.3 Settling of Magnetic Fluid

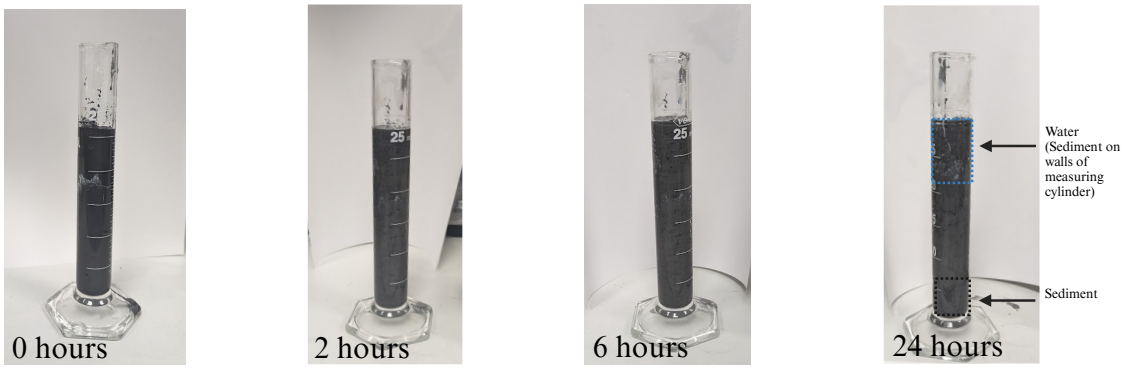

Figure 5.13: Settling of the iron particles in the magnetic fluid. The fluid remains usable for 0-12 hours before agitation is needed. The fluid is visibly settled into layers after 24 hours.

References

[1] S. M. Kavic and M. D. Basson, "Complications of endoscopy," *The American journal of surgery*, vol. 181, no. 4, pp. 319–332, 2001.

[2] G. Pittiglio, P. Lloyd, T. da Veiga, *et al.*, "Patient-specific magnetic catheters for atraumatic autonomous endoscopy," *Soft robotics*, vol. 9, no. 6, pp. 1120–1133, 2022.

[3] T. da Veiga, J. H. Chandler, P. Lloyd, *et al.*, "Challenges of continuum robots in clinical context: A review," *Progress in Biomedical Engineering*, vol. 2, no. 3, p. 032 003, 2020.

[4] H. B. Gilbert, D. C. Rucker, and R. J. Webster III, "Concentric tube robots: The state of the art and future directions," in *Robotics Research: The 16th International Symposium ISRR*, Springer, 2016, pp. 253–269.

[5] I. W. SCUDAMORE, B. C. DUNPHY, and I. D. COOKE, "Outpatient falloposcopy; intra-luminal imaging of the fallopian tube by trans-uterine fibre-optic endoscopy as an outpatient procedure," *BJOG: An International Journal of Obstetrics & Gynaecology*, vol. 99, no. 10, pp. 829–835, 1992.

[6] S. Masuda, "Apparatus for feeding a flexible tube through a conduit," *GB-1534441-A, UK patent*, vol. 1, no. 6, 1978.

[7] P. Berthet-Rayne, S. H. Sadati, G. Petrou, *et al.*, "Mammobot: A miniature steerable soft growing robot for early breast cancer detection," *IEEE Robotics and Automation Letters*, vol. 6, no. 3, pp. 5056–5063, 2021.

[8] E. W. Hawkes, L. H. Blumenschein, J. D. Greer, and A. M. Okamura, "A soft robot that navigates its environment through growth," *Science Robotics*, vol. 2, no. 8, eaan3028, 2017.

[9] D. Seo, N. G. Kim, and J.-H. Ryu, "Inflatable-structure-based working-channel securing mechanism for soft growing robots," *IEEE Robotics and Automation Letters*, 2024.

[10] T. Ashuri, A. Armani, R. Jalilzadeh Hamidi, T. Reasnor, S. Ahmadi, and K. Iqbal, "Biomedical soft robots: Current status and perspective," *Biomedical Engineering Letters*, vol. 10, pp. 369–385, 2020.

[11] C. Girerd, A. Alvarez, E. W. Hawkes, and T. K. Morimoto, "Material scrunching enables working channels in miniaturized vine-inspired robots," *IEEE Transactions on Robotics*, 2024.

[12] S. Goldstein, R. Jones, J. Sipe, J. Doppman, and J. Boretos, "A miniature toposcopic catheter suitable for small diameter tortuous blood vessels," *J Biomech Eng*, 1980.

[13] M. Li, R. Obregon, J. J. Heit, A. Norbash, E. W. Hawkes, and T. K. Morimoto, "Vine catheter for endovascular surgery," *IEEE Transactions on Medical Robotics and Bionics*, vol. 3, no. 2, pp. 384–391, 2021.

[14] Y. Kim and X. Zhao, "Magnetic soft materials and robots," *Chemical reviews*, vol. 122, no. 5, pp. 5317–5364, 2022.

[15] X. Fan, X. Dong, A. C. Karacakol, H. Xie, and M. Sitti, "Reconfigurable multifunctional ferrofluid droplet robots," *Proceedings of the National Academy of Sciences*, vol. 117, no. 45, pp. 27 916–27 926, 2020.

[16] R. Ahmed, M. Ilami, J. Bant, B. Beigzadeh, and H. Marvi, "A shapeshifting ferrofluidic robot," *Soft Robotics*, vol. 8, no. 6, pp. 687–698, 2021.

[17] H. Leon-Rodriguez, V. H. Le, S. Y. Ko, J.-O. Park, and S. Park, "Ferrofluid soft-robot bio-inspired by amoeba locomotion," in *2015 15th international conference on control, automation and systems (ICCAS)*, IEEE, 2015, pp. 1833–1838.

[18] J. Davy, N. Greenidge, S. Kim, *et al.*, "Vine robots with magnetic skin for surgical navigations," *IEEE Robotics and Automation Letters*, 2024.

[19] N. G. Kim, N. J. Greenidge, J. Davy, *et al.*, "External steering of vine robots via magnetic actuation," *Soft Robotics*, 2024.

[20] D. Van Lewen, T. Janke, H. Lee, R. Austin, E. Billatos, and S. Russo, "A millimeter-scale soft robot for tissue biopsy procedures," *Advanced Intelligent Systems*, vol. 5, no. 5, p. 2 200 326, 2023.

[21] J. Zhang, Q. Fang, P. Xiang, *et al.*, "Flexible biopsy robot with force sensing for deep lung examination," *Advanced Intelligent Systems*, vol. 6, no. 2, p. 2 300 107, 2024.

[22] A. K. Golahmadi, D. Z. Khan, G. P. Mylonas, and H. J. Marcus, "Tool-tissue forces in surgery: A systematic review," *Annals of Medicine and Surgery*, vol. 65, p. 102 268, 2021.

[23] P. Ryapolov, A. Vasilyeva, D. Kalyuzhnaya, A. Churaev, E. Sokolov, and E. Shel'deshova, "Magnetic fluids: The interaction between the microstructure, macroscopic properties, and dynamics under different combinations of external influences," *Nanomaterials*, vol. 14, no. 2, p. 222, 2024.

[24] K. J. McDonald, L. Kinnicutt, A. M. Moran, and T. Ranzani, "Modulation of magnetorheological fluid flow in soft robots using electropermanent magnets," *IEEE Robotics and Automation Letters*, vol. 7, no. 2, pp. 3914–3921, 2022.

[25] S. Al Harthy, H. Sadati, C. Girerd, *et al.*, "Tip-growing robots: Design, theory, application," *IEEE Transactions on Robotics*, 2024.

[26] P. E. Glick, I. Adibnazari, D. Drotman, D. Ruffatto III, and M. T. Tolley, "Branching vine robots for unmapped environments," *Frontiers in Robotics and AI*, vol. 9, p. 838 913, 2022.

[27] Y. Li, J. Peine, M. Mencattelli, J. Wang, J. Ha, and P. E. Dupont, "A soft robotic balloon endoscope for airway procedures," *Soft Robotics*, vol. 9, no. 5, pp. 1014–1029, 2022.

[28] A. Repici, M. Spadaccini, E. Vespa, *et al.*, "Endorail add-on device for solving colon loops: Proof of concept in a phantom colon.," *Endoscopy*, vol. 54, no. S 01, eP174, 2022.

[29] M. Chovancová and J. Elcner, "The pressure gradient in the human respiratory tract," in *EPJ Web of Conferences*, EDP Sciences, vol. 67, 2014, p. 02 047.

[30] J. Rogatinsky, D. Recco, J. Feichtmeier, *et al.*, "A multifunctional soft robot for cardiac interventions," *Science Advances*, vol. 9, no. 43, eadi5559, 2023.

[31] L. T. Gaeta, K. J. McDonald, L. Kinnicutt, *et al.*, "Magnetically induced stiffening for soft robotics," *Soft Matter*, vol. 19, no. 14, pp. 2623–2636, 2023.

[32] M. Manti, V. Cacucciolo, and M. Cianchetti, "Stiffening in soft robotics: A review of the state of the art," *IEEE Robotics & Automation Magazine*, vol. 23, no. 3, pp. 93–106, 2016.

[33] S. Al Harthy, S. H. Sadati, Z. Wu, C. A. Seneci, and C. Bergeles, "Variable stiffness soft eversion growing robot via temperature control of low-melting point alloy pres-

surised medium," in *2024 International Symposium on Medical Robotics (ISMR)*, IEEE, 2024, pp. 1–7.

[34] N. Murasovs, V. Francescon, P. Lloyd, *et al.*, "Breathing compensation in magnetic robotic bronchoscopy via shape forming," *IEEE Robotics and Automation Letters*, 2024.

[35] W. E. Heap, N. D. Naclerio, M. M. Coad, S.-G. Jeong, and E. W. Hawkes, "Soft retraction device and internal camera mount for everting vine robots," in *2021 IEEE/RSJ International Conference on Intelligent Robots and Systems (IROS)*, IEEE, 2021, pp. 4982–4988.

[36] X. Pi, I. A. Szczech, and L. Cao, "A retractable soft growing robot with a flexible backbone," in *2023 IEEE/RSJ International Conference on Intelligent Robots and Systems (IROS)*, IEEE, 2023, pp. 2477–2484.

[37] T. da Veiga, G. Pittiglio, M. Brockdorff, J. H. Chandler, and P. Valdastri, "Six-degree-of-freedom localization under multiple permanent magnets actuation," *IEEE Robotics and Automation Letters*, vol. 8, no. 6, pp. 3422–3429, 2023.

[38] J. Davy, P. Lloyd, J. H. Chandler, and P. Valdastri, "A framework for simulation of magnetic soft robots using the material point method," *IEEE Robotics and Automation Letters*, vol. 8, no. 6, pp. 3470–3477, 2023.

[39] T. Da Veiga, J. H. Chandler, G. Pittiglio, *et al.*, "Material characterization for magnetic soft robots," in *2021 IEEE 4th International Conference on Soft Robotics (RoboSoft)*, IEEE, 2021, pp. 335–342.

[40] G. Sinclair and J. Helms, "A review of simple formulae for elastic hoop stresses in cylindrical and spherical pressure vessels: What can be used when," *International Journal of Pressure Vessels and Piping*, vol. 128, pp. 1–7, 2015.

5.9 Chapter Evaluation

This chapter introduces the concept of magnetic fluid steered vine robots. Our contribution is the novel design of this soft robot and exploring its application in endoluminal

navigation. The clear contribution when compared to the magnetic skin approach is this approaches use of internal magnetic fluid to vastly improves navigation ability. This is due to the high magnetic volume enabling simultaneous steering and growing, vastly improving robot dexterity. The magnetic fluid approach essentially finds a middle ground between the magnetic tip approaches (with associated high magnetic volume) of Kim et al. and the magnetic skin approach of the previous chapter (with associated soft compliant structure), leading to a robot that can navigate through small complex anatomy, but be easily steered under magnetic fields [1].

As vine robots are miniaturised, the required growing pressure increases with the reciprocal square of the diameter, this leads to a potential safety implication in the case of leakage, with concern of potential vessel puncture or damage. However we have demonstrated for our 4 mm robot a growing pressure of just 35 kPa, well below the safe pressure of 62 kPa established in by Li et al. for bronchoscopy [2]. Our robot was successful in penetrating our soft tissue phantom with ease with the ability to generate over 1 N of force for the purpose of tissue penetration as specified in our design goals.

The major drawback of this design is the complexity between relationship of applied magnetic field and bending. The particle dispersion is inherently difficult to model and the suspension settles without agitation. Further challenges include potential biocompatibility issues in certain areas of the body and unwanted magnetorheological effects although these could be likely addressed by modifications to the fluid mixture.

The stabilisation properties of vines as well as their inherent tool channel provide a suitable platform for insertion of tools enabling stabilisation on surrounding anatomy. This enables our studied application of tissue biopsy via producing large tip forces despite an entirely soft structured robot.

This work advances the application of vine robots by demonstrated an entirely scalable steering method that crucially retains the soft body of the robot allowing conformity to the external enviroment. In theory this design has unbounded miniaturisation with the limiting factor being the ability to create sufficiently thin-wall tubes capable of eversion.

References

[1] N. G. Kim, N. J. Greenidge, J. Davy, *et al.*, "External steering of vine robots via magnetic actuation," *Soft Robotics*, 2024.

[2] M. Li, R. Obregon, J. J. Heit, A. Norbash, E. W. Hawkes, and T. K. Morimoto, "Vine catheter for endovascular surgery," *IEEE Transactions on Medical Robotics and Bionics*, vol. 3, no. 2, pp. 384–391, 2021.

Chapter 6

Conclusions

In this thesis, we have explored bio-inspired approaches to the creation of miniaturised magnetic robots. We aim to replicate some of the behaviours observed in nature such as the movement of tentacles of octopuses and squids, or the seemingly effortless movement of plant vines. We consider the application of these robots in the surgical setting for minimally invasive surgery; in particular the navigation of tortuous anatomy where conventual instruments struggle with frictional forces and potentially traumatic tissue interactions. We explore two such robots, the first is the shape-forming tentacle robot previously explored in our group [1], [2]. This robot, formed of a magnetic elastomer is produced from a computational design process based on a target patient-specific anatomy. This process leads to a unique magnetisation profile for the robot which gives rise to a shape-forming ability under pre-determined magnetic fields. In the work presented in this thesis, we tackle one of the challenges of the computational design process, in particular the challenges of simulating magnetic soft bodies. To do this we present a novel simulation framework based on the Material Point Method (MPM) where we integrate models of magnetic elastomers to create a mesh-less representation of arbitrary magnetic soft materials and magnetic profiles. Computational design processes, even when well equipped with models capable of representing real geometry and complex magnetic profiles, still struggle with reality-gap issues. Furthermore, the design of patient-specific catheters have drawbacks including custom manufacturing and complex magnetic con-

trol. To counter these challenges we proposed the design of miniaturised magnetic vine robots. These entirely soft robots move under the principle of eversion, growing at their tip and therefore mitigating friction with the external environment. This enables their navigation through tight tortuous vessels without the need for complexities such as magnetic profiles and patient-specific designs. Through the embedding of magnetic material within the structure of the robot we can steer through bifurcations via application of external fields. To achieve this we proposed two such methods for integrating magnetic agents. The first is that of a magnetic skin of the vine robot which embeds magnetic micro particles into the vine robot wall. This approach enables steering but only once the internal pressure of the vine had been decreased. This lead to a navigation strategy based on duty cycling of internal pressure, however this limited the ease of navigation due to the inability to grow and steer the vine robot simultaneously. This brought us to our second approach, that of an internal magnetic fluid which enabled high magnetic volume and therefore concurrent steering and growing. This enabled navigation of complex vessels all whilst retaining the soft structure of the robot. We utilise this soft complaint structure to stabilise on the surround vessel wall, enabling high tip forces to be applied from a internal biopsy tool.

There are areas of the anatomy such as the peripheral bronchial tree or the Cerebral-Spinal Fluid (CSF) spaces in the brain where conventional surgical tools would be associated with too high a risk of tissue trauma. Soft tools (where the stiffness is of the order of the tissue itself) come with an inherent safety factor, however their lack of body stiffness means insertion is difficult and buckling is common. Everting vine-like robotic tools can compensate for this issue via their lack of translating motion. Miniaturisation of everting tubes has been proven to scales of 1 mm diameter [3]. In our work, we have reached scales of 4 mm, however further miniaturisation should be possible. In this thesis, manufacturing has not been the overall focus of the work and a deeper study of materials and fabrication techniques would enable the replication of 1 mm diameter or potentially even smaller designs. The magnetic fluid approach should scale well here, given the reduced required buckling forces at smaller diameters and simple applicability

of an internal magnetic fluid.

Although the magnetic skin and fluid approaches are appealing due to the entirely soft structure, the permanent magnetic tip approach is likely acceptable for a lot of applications. As long as the soft body of the vine is preserved, and locomotion is via the internal growing pressure, then the potential for traumatic tissue interaction would likely remain low. However, the maintaining of a permanent tip on an everting system is non-trivial [4], [5]. More recent work has considered tip material scrunching as an alternative to fully everting vine robots enabling permanent tips and relatively low growing pressures [6]. Others have considered attachment of tips to traditional everting vine robots [7]–[9]. However these come at the cost of additional mechanical complexity due to the relative velocity of the everting vine material being twice that of movement of the tip. Either some internal mechanism such as a friction-based or magnetic attachment system allows for passive synchronisation of the tip or alternatively external synchronisation via translation insertion stages can be utilised [7], [10]. The use of magnetics for actuation is advantageous because of the ability to precisely and wirelessly apply force and torques to the internal magnetic elements of the robot. However, this comes at the cost of external hardware which size increases with the required magnetic field which can become high when the internal magnetic volume of the device is low, this is particularity apparent in highly miniaturised devices with little space for magnetic material. When designing any surgical device, there is question around biocompatibility of the materials used. This is particularly apparent in the use of magnetic materials which have the potential for toxicity, particularly if implanted within the body. Translational work would require analysis of these biocompatibility concerns, particularly when considering magnetic fluid based devices.

The question of retracting the vine promotes several points of view. In the ideal case, it would be appealing for vine robots to retract in the inverse manner to their growing, therefore maintaining shear-free movement. This has been studied via addition of adjacent "retraction channels" for soft vine robots and has been demonstrated down to a 3 mm diameter scale [11], [12]. Alternatively, it may just be acceptable for a lot of clinical

applications to simply retract the vine robot by depressurisation and pulling from the distal end. This is clearly simpler and scalable and is advantaged by the entirely soft vine robots studied in this thesis due to their diameter decreasing significantly when not pressurised.

Our developed simulation framework in Chapter 2 has proved itself useful beyond the work of our group, backed up by several recent publications and dissertations utilising it [13]–[15]. The framework was deliberately made to generalise across robotic approaches from micro-robots to centimetre-scale magnetic continuum robots. The advantage of MPM methodology is its overall simple implementation when compared to FEM approaches along with the associated advantages of a mesh-free implementation. Future work should consider how this MPM framework could be expanded to also consider vine robots. This would involve integrated pneumatic material models as well as considering efficient implementation of sliding contacts between materials. Simulation models of magnetic vine robots would potentially allow them to be integrated into computational design frameworks for design of both structure and magnetic profile. This could lead to a hybrid-like design combining the benefits of the tentacle robots with the everting properties of vines.

Fundamentally, this work proposes a radical approach for surgical instruments far from current clinical practice. Magnetically-driven devices such as Niobe and Levita, have received associated clinical approval [16]–[18]. Technologies based on eversion have also reached advanced pre-clinical trials however haven't seen widespread adoption [3], [19], [20]. With the appealing advantages of the techniques given in this thesis, future work should concern itself with specific clinical problems motivated by close collaboration with clinicians, towards the overall betterment of public healthcare services.

6.1 Future Work

References

[1] P. Lloyd, G. Pittiglio, J. H. Chandler, and P. Valdastri, "Optimal design of soft continuum magnetic robots under follow-the-leader shape forming actuation," in *2020 International Symposium on Medical Robotics (ISMR)*, IEEE, 2020, pp. 111–117.

[2] G. Pittiglio, P. Lloyd, T. da Veiga, *et al.*, "Patient-specific magnetic catheters for atraumatic autonomous endoscopy," *Soft Robotics*, 2022.

[3] S. Goldstein, R. Jones, J. Sipe, J. Doppman, and J. Boretos, "A miniature toposcopic catheter suitable for small diameter tortuous blood vessels," *J Biomech Eng*, 1980.

[4] M. M. Coad, L. H. Blumenschein, S. Cutler, *et al.*, "Vine robots," *IEEE Robotics & Automation Magazine*, vol. 27, no. 3, pp. 120–132, 2019.

[5] C. Suulker, S. Skach, D. Kaleel, *et al.*, "Soft cap for vine robots," in *2023 IEEE/RSJ International Conference on Intelligent Robots and Systems (IROS)*, IEEE, 2023, pp. 6462–6468.

[6] C. Girerd, A. Alvarez, E. W. Hawkes, and T. K. Morimoto, "Material scrunching enables working channels in miniaturized vine-inspired robots," *IEEE Transactions on Robotics*, 2024.

[7] A. Yanez Trujillo, J. Davy, J. H. Chandler, J. Avery, and P. Valdastri, "Miniaturized magnetic tip design for endoluminal vine robot navigation," *Advanced Robotics Research*, e202500188, 2026.

[8] N. G. Kim, S. Park, D. Seo, *et al.*, "A soft growing robotic endoscope for painless and strain-free insertion," *Soft Robotics*, 2025.

[9] N. G. Kim, N. J. Greenidge, J. Davy, *et al.*, "External steering of vine robots via magnetic actuation," *Soft Robotics*, 2024.

[10] P. Berthet-Rayne, S. H. Sadati, G. Petrou, *et al.*, "Mammobot: A miniature steerable soft growing robot for early breast cancer detection," *IEEE Robotics and Automation Letters*, vol. 6, no. 3, pp. 5056–5063, 2021.

[11] N. G. Kim, D. Seo, S. Park, and J.-H. Ryu, "Self-retractable soft growing robots for reliable and fast retraction while preserving their inherent advantages," *IEEE Robotics and Automation Letters*, 2023.

[12] S. Kim and T. K. Morimoto, "Kinked air channel enables retraction of small-scale soft everting robots," in *2025 IEEE 8th International Conference on Soft Robotics (RoboSoft)*, IEEE, 2025, pp. 1–8.

[13] L. Wang, "Co-design of magnetic soft robots with large deformation and contacts via material point method and topology optimization," *Computer Methods in Applied Mechanics and Engineering*, vol. 445, p. 118 205, 2025.

[14] S. Wang, Z. Dai, Q. Lu, and C.-Y. Su, "The simulation and path tracking control study of magnetic miniature soft robots," *Journal of Field Robotics*, vol. 42, no. 3, pp. 903–915, 2025.

[15] F. Norouziani, "Design of small scale magnetic soft robots using cma-es and material point method," Ph.D. dissertation, 2025.

[16] J. Fulla, A. Small, E. Kaplan-Marans, and M. Palese, "Magnetic-assisted robotic and laparoscopic renal surgery: Initial clinical experience with the levita magnetic surgical system," *Journal of Endourology*, vol. 34, no. 12, pp. 1242–1246, 2020.

[17] I. N. Haskins, A. T. Strong, M. T. Allemang, K. P. Bencsath, J. H. Rodriguez, and M. D. Kroh, "Magnetic surgery: First us experience with a novel device," *Surgical endoscopy*, vol. 32, no. 2, pp. 895–899, 2018.

[18] M. P. Armacost, J. Adair, T. Munger, *et al.*, "Accurate and reproducible target navigation with the stereotaxis niobe® magnetic navigation system," *Journal of Cardiovascular Electrophysiology*, vol. 18, S26–S31, 2007.

[19] D. A. Haggerty, J. R. Cazzoli, M. A. Wayne, *et al.*, "A soft robotic device for rapid and self-guided intubation," *Science Translational Medicine*, vol. 17, no. 815, eads7681, 2025.

[20] Z. Wu, H. Sadati, P. Vartholomeos, *et al.*, "Vine-inspired robots for navigation in the spinal subarachnoid space: A pilot human tissue study," in *Vine-inspired Robots for Navigation in the Spinal Subarachnoid Space: A Pilot Human Tissue Study*, 2025.

Appendix A

Appendix

A.1 Workshop Paper: Computational Design of Magnetic Soft Shape-Forming Catheters using the Material Point Method

A.1.1 Abstract

Magnetic Soft Catheters (MSCs) are capable of miniaturisation due to the use of an external magnetic field for actuation. Through careful design of the magnetic elements within the MSC and the external magnetic field, the shape along the full length of the catheter can be precisely controlled. However, modelling of the magnetic-soft material is challenging due to the complex relationship between magnetic and elastic stresses within the material. Approaches based on traditional Finite Element Methods (FEM) lead to high computation time and rely on proprietary implementations. In this work, we showcase the use of our recently presented open-source simulation framework based on the Material Point Method (MPM) for the computational design of magnetic soft catheters to realise arbitrary shapes in 3D, and to facilitate follow-the-leader shape-forming insertion.

A.1.2 Introduction

Magnetic Soft Catheters (MSCs) have been proposed as a solution for minimally invasive medical procedures [1]. The ability to achieve miniaturisation and precise shape control of these catheters using an external magnetic field has opened up new possibilities for targeted interventions [2]. Through careful design of magnetic elements integrated within the catheter, the full-length shape can be controlled to navigate through intricate anatomical pathways with enhanced accuracy and dexterity. This, along with the soft structure of the catheter, reduces the anatomical forces on the surrounding tissues with the potential to reduce patient trauma [3].

However, the successful implementation of MSCs hinges upon the ability to accurately model the complex interaction between magnetic and elastic stresses within the catheter's soft material. Traditional approaches, such as Finite Element Methods (FEM), have been employed to simulate and analyse these interactions [4]. Yet these methods often suffer from high time complexity and rely on proprietary software/toolkits limiting accessibility and hindering broader research efforts.

In our recent work, we presented a simulation framework for modelling of magnetic soft materials based on the Material Point Method (MPM) [5]. Unlike previously presented FEM approaches, our framework inherently models self-collision between areas of the model and can capture the effect of forces in non-homogeneous magnetic fields. We demonstrated this framework on various test cases but also on robot designs presented in the literature with good agreement with the authors' real-world results.

Previous work on this, based on FEM analysis was found to have high time complexities limiting the ability to apply iterative optimisation processes to these models [6]. Instead a data-driven approach was applied where a data-set of MSC deformations under various applied fields was initially created and a neural network trained to approximate the inverse function. Although functional, this system was limited to a 2D case and three magnetic elements. Data-driven approaches often fail to generalise far from their provided data-set. For this approach to move to 3D catheters under a wider range of deformations, the

required data collection and training process would become computationally intractable. In contrast, FEM based approaches have been directly optimised on using evolutionary algorithms [7], however the combination of large computation time and high number of iterations for convergence can lead to large run-times.

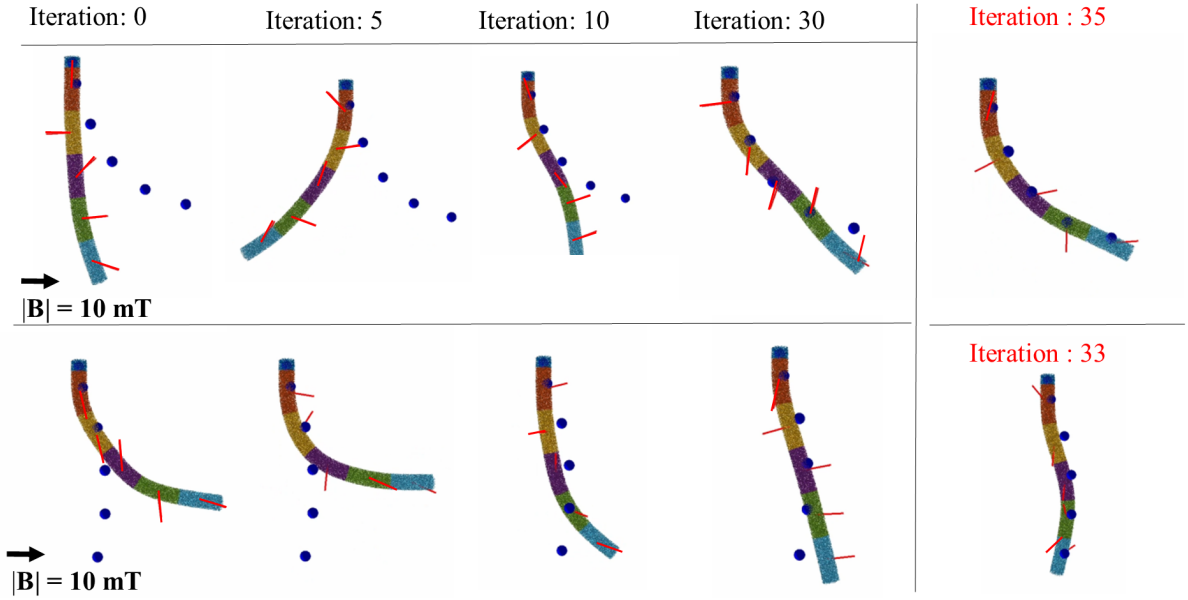

Figure A.1: Convergence of static deformations of MSCs. Target shapes shown as blue dots and magnetisation vectors by red arrows. The actuating field is fixed and the magnetisation vectors are optimised to minimse the gap between deformation and target shape.

Another approach has been to utilise more simplified modelling such as rigid links [3]. However, this fails to capture the full geometric structure of the MSC and introduce additional dependent variables such as number of links, link length etc.. Further, the twisting instability of MSCs around their major-axis has been noted as an important factor in their design [3]. Simplified models fail to capture this.

In this work, we consider the application of the *magneticMPM* framework for computational design of shape-forming catheters. In particular, we showcase the ability to model the 3D deformation of catheters in dynamic simulation. Our computational design approach is computationally tractable with each iteration lasting between 20 and 25 seconds. The use of a surrogate based optimisation approach allows convergence of our process within 100 iterations.

A.1.3 Simulation of catheters with magneticMPM

Previously, we presented an open-source simulation framework for representing magnetic soft robots based on MPM. The magneticMPM framework is available at `https://github.com/joshDavy1/magneticMPM`. The simulation framework is capable of representing magnetic soft robot designs of various scales and geometry. In particular, we replicated the designs of [8] and [9] in simulation. MPM utilises a dual particle-grid representation of the material. The lack of a deforming underlying mesh (Such as in FEM), allows large deformations to be represented without the risk of mesh collapse. The MSCs we consider are fully soft and are formed of silicone polymers mixed with NdFeB magnetic powder. Once cast and cured, these catheters are then subjected to an impulse magnetic field that sets the direction of remnant magnetisation. The direction of this magnetisation as a function of the robot's length is referred to as it's magnetic profile. This magnetic profile can be carefully designed in order to give desired deformations under an applied magnetic field.

To simulate the MSC in magneticMPM, we adopt the Neo-Hookean hyper-elastic model to represent the soft material in Piola-Kirchoff form

$$\mathbf{P}^t_{p,elastic} = GJ^{-2/3}(\mathbf{F}^t_p - \frac{I_1}{3}\mathbf{F}^{-T}) + KJ(J-1)\mathbf{F}^{-T}. \tag{A.1}$$

where $\mathbf{P}p^t_{p,elastic}$ is the elastic contribution of the first Piola-Kirchoff stress tensor, G is the shear modulus of the material and K is the bulk modulus. $J = \text{determinant}(\mathbf{F}^t_p)$ and $I_1 = \text{trace}(\mathbf{F}^{t^T}_p \mathbf{F}^t_p)$. Assuming near incompressiblity of the utilised silicone polymers we chose the bulk modulus to be a sufficiently high value. In this case we set $K = 20G$.

For the magnetic properties, we use the stress-relationship derived in Zhao et. al. [10]

$$\mathbf{P}^t_{p,magnetic} = -\frac{1}{\mu_0}\mathbf{B} \otimes \mathbf{B}_{r_p}, \tag{A.2}$$

where $\otimes$ is the dyadic product and $\mathbf{B}_{r_p}$ is the remnant magnetic flux density associated

with the particle. B is the applied field.

A.1.4 Computational Design

By iterative optimisation, the magnetic profile of the simulated MCR can be adjusted until the desired deformation is achieved. To achieve this, we can formulate the optimisation as a minimisation process using the cost function

$$f(\boldsymbol{\theta}) = \sum_{i}^{N} ||\mathbf{p}_i - \hat{\mathbf{p}}_i||^2. \tag{A.3}$$

where $\boldsymbol{\theta}$ is the magnetic profile, $\mathbf{p}_i$ is the desired position at distance i along the robot $i \in \{0, N\}$. $\hat{\mathbf{p}}_i$ is the equivalent resultant position in simulation. This cost is then minimised in order to give the final magnetic profile.

The optimisation process can be treated as an expensive black-box optimisation problem. With the computational time of each iteration being in the range of 20 - 25 seconds. We apply the Bayesian optimisation algorithm to this problem in order to converge in a tractable time. This, algorithm relies on a underlying surrogate function that is sampled in order to choose the next magnetic profile. Each iteration is utilised to improve this surrogate function. More details can be found in [11].

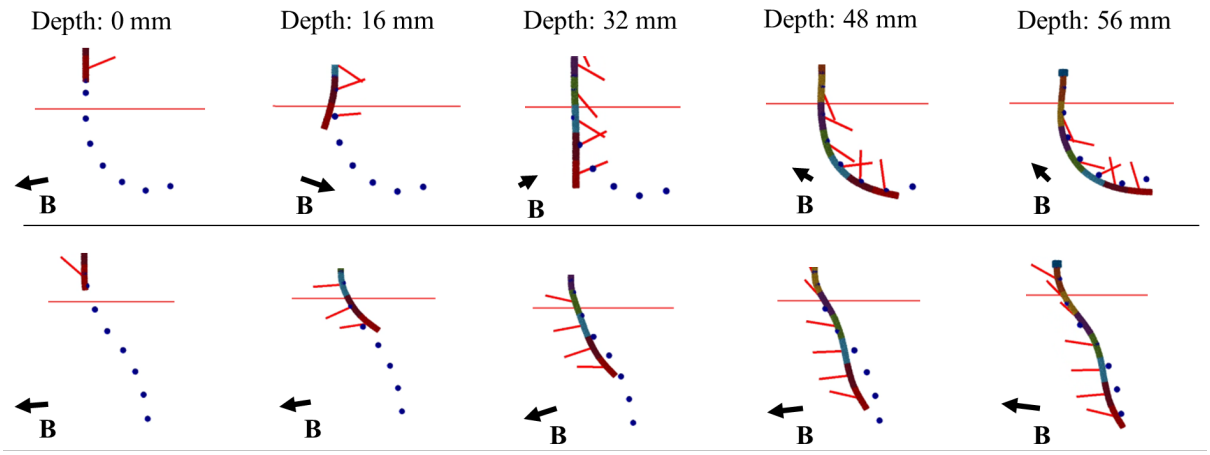

Figure A.2: Converged solutions of two MSCs under follow-the-leader actuation.

A.1.5 Results

To evaluate our methodology, we assume the material properties of previously presented MSCs shown in [12]. Each MSC is formed of N magnetic segments each with their own direction of magnetisation. An external homogenous magnetic field is applied leading the MSC to deform.

A.1.5.1 Static deformation

We first consider the static deformations of the MSC under a fixed applied field with $N = 5$. The catheter length is 40 mm with diameter 4 mm. The optimisation process was repeated until an average RMS error of below 2 mm between target and desired shape was achieved. Figure A.1 shows two examples of the iterative process on two arbitrary target shapes. Convergence was achieved in 35 and 33 iterations respectively. From random initialisation, it can be observed that the solution is found in a small number of iterations.

A.1.5.2 Deformation under continuous insertion

When considering a MSC inserting into a lumen, a follow-the-leader trajectory must be followed. Here, a target path is defined which the catheter must follow whilst inserted into the space. The catheter length is 56 mm and diameter 3 mm. With the need to change the sectional deformation as the catheter is inserted, the applied field is also included in the optimisation vector. The field norm was limited to a maximum $B = 10$ mT. Figure A.2 shows two examples of converged solutions for arbitrary shapes. Both converged in under a 100 iterations with an exit error of 3 mm.

A.1.6 Conclusion

In this work, we consider the computational design of magnetic soft shape-forming catheters. Utilising our open-source framework, we have successfully shown the tractability of 3D simulations of MSCs and integrated that into an optimisation problem in order

to solve for shape-forming tasks. Similar work [4], based on evolutionary algorithms require hundreds of iterations before convergence. The underlying surrogate function in Bayesian optimisation allows efficient sampling with the simulation keeping the runtime within tractability.

Compared to the data driven approach in [4], our proposed model-based optimisation generalises well to various deformations and robot geometries. This avoids any need for large dataset collection and training process. However, to be an accurate representation of real world MSCs, the underlying simulation material parameters must closely match. In this work, we relied on existing material parameter data from previous work [13], however these optimal parameters will depend on the strain ranges experienced.

The use of a surrogate based optimisation with a realistic simulation model could be considered a hybrid between data-driven and model-based approaches. The surrogate model is incrementally improved with each sample of the real world simulation and is used to suggest new sample points for the relatively expensive simulation model.

Although our previous work showcased the strong agreement between our magneticMPM framework and real world results [5], the results shown in this work must be validated against real world fabricated MSCs. We will consider how this methodology can be further applied to optimise additional factors, such as catheter geometry, energy minimisation and to achieve dynamic time-variant behaviours.

References

[1] C. Zhou, Y. Yang, J. Wang, *et al.*, "Ferromagnetic soft catheter robots for minimally invasive bioprinting," *Nature communications*, vol. 12, no. 1, p. 5072, 2021.

[2] G. Pittiglio, J. H. Chandler, T. da Veiga, *et al.*, "Personalized magnetic tentacles for targeted photothermal cancer therapy in peripheral lungs," *Communications Engineering*, vol. 2, no. 1, p. 50, 2023.

[3] P. Lloyd, O. Onaizah, G. Pittiglio, D. K. Vithanage, J. H. Chandler, and P. Valdastri, "Magnetic soft continuum robots with braided reinforcement," *IEEE Robotics and Automation Letters*, vol. 7, no. 4, pp. 9770–9777, 2022.

[4] P. Lloyd, G. Pittiglio, J. H. Chandler, and P. Valdastri, "Optimal design of soft continuum magnetic robots under follow-the-leader shape forming actuation," in *2020 International Symposium on Medical Robotics (ISMR)*, IEEE, 2020, pp. 111–117.

[5] J. Davy, P. Lloyd, J. H. Chandler, and P. Valdastri, "A framework for simulation of magnetic soft robots using the material point method," *IEEE Robotics and Automation Letters*, vol. 8, no. 6, pp. 3470–3477, 2023.

[6] P. Lloyd, A. K. Hoshiar, T. da Veiga, *et al.*, "A learnt approach for the design of magnetically actuated shape forming soft tentacle robots," *IEEE Robotics and Automation Letters*, vol. 5, no. 3, pp. 3937–3944, 2020.

[7] L. Wang, D. Zheng, P. Harker, A. B. Patel, C. F. Guo, and X. Zhao, "Evolutionary design of magnetic soft continuum robots," *Proceedings of the National Academy of Sciences*, vol. 118, no. 21, e2021922118, 2021. DOI: 10.1073/pnas.2021922118. eprint: https://www.pnas.org/doi/pdf/10.1073/pnas.2021922118. [Online]. Available: https://www.pnas.org/doi/abs/10.1073/pnas.2021922118.

[8] T. Xu, J. Zhang, M. Salehizadeh, O. Onaizah, and E. Diller, "Millimeter-scale flexible robots with programmable three-dimensional magnetization and motions," *Science Robotics*, vol. 4, no. 29, eaav4494, 2019.

[9] W. Hu, G. Z. Lum, M. Mastrangeli, and M. Sitti, "Small-scale soft-bodied robot with multimodal locomotion," *Nature*, vol. 554, no. 7690, pp. 81–85, 2018.

[10] R. Zhao, Y. Kim, S. A. Chester, P. Sharma, and X. Zhao, "Mechanics of hard-magnetic soft materials," *Journal of the Mechanics and Physics of Solids*, vol. 124, pp. 244–263, 2019.

[11] P. I. Frazier, "A tutorial on bayesian optimization," *arXiv preprint arXiv:1807.02811*, 2018.

[12] G. Pittiglio, P. Lloyd, T. da Veiga, *et al.*, "Patient-specific magnetic catheters for atraumatic autonomous endoscopy," *Soft Robotics*, 2022.

[13] T. Da Veiga, J. H. Chandler, G. Pittiglio, *et al.*, "Material characterization for magnetic soft robots," in *2021 IEEE 4th International Conference on Soft Robotics (RoboSoft)*, IEEE, 2021, pp. 335–342.